DOCTORAL THESIS

Study of a gliding arc discharge for sustainable nitrogen fixation into NO_X

by

Filippo Manaigo

Chimie des Interactions Plasma-Surface (ChIPS),
Faculté des Sciences,
Université de Mons

Plasma Lab for Application in Sustainability and Medicine ANTwerp (PLASMANT),
Faculteit wetenschappen,
Universiteit Antwerpen

Promoters and Committee Members

Promoter:
Prof. Rony Snyders
(Research Group ChIPS, University of Mons, Belgium)

Promoter:
Prof. Annemie Bogaerts
(Research Group PLASMANT, University of Antwerp, Belgium)

Committee members:

Prof. Jérôme Cornil
(CMN, University of Mons, Belgium)

Dr. Olivier Guaitella
(LPP, Ecole Polytechnique, France)

Prof. Stéphanos Konstantinidis
(ChIPS, University of Mons, Belgium)

Prof. Rino Morent
(RUPT, Ghent University, Belgium)

Prof. Erik Neyts
(PLASMANT, University of Antwerp, Belgium)

Dr. Georgi Trenchev
(PLASMANT, University of Antwerp, Belgium)

Abstract

With the growth of the world population, the agricultural sector is required to meet an increasing demand for nutrients. In order to achieve this, since decades the sector has relied on industrially produced fertilizers to increase its production yield. Among them, nitrogen-based fertilizers are the most common choice, although their production requires inert N_2 to be converted into more reactive molecules, such as nitric oxides NO_x or ammonia NH_3, in a process called "nitrogen fixation". Today, this is mainly performed in industry through the well-known Haber-Bosch process. Despite being the dominant choice for industrial nitrogen fixation for over a century because of an almost perfect optimization, the Haber-Bosch process is not ideal since it requires large-scale facilities to be economical and is associated with a high energy cost and high CO_2 emissions, thus, resulting in an environmental impact that is pushing for the study of different, greener, alternatives.

Among several options, plasma-based nitrogen fixation to NO_x is considered a promising alternative to Haber-Bosch, thanks to (i) the possibility of implementing the technology at lower scales, (ii) its compatibility with intermittent, renewable energy sources, and (iii) the absence of direct CO_2 emissions. In this context, a type of plasma reactor that proved to be particularly suitable for nitrogen fixation is the gliding arc plasma, as it operates at atmospheric pressure and favors energy transfer toward vibrational excitation states, which is known to be beneficial for the NO_x synthesis, although in practice, due to the high temperature in this "warm plasma" (order of 3000 K), vibrational-translation relaxation is quite efficient, reducing the populations of the vibrational excited levels, so they are in equilibrium with the gas temperature.

This thesis aims to study plasma-based nitrogen fixation focusing on a gliding arc plasma operating with N_2 and O_2 at atmospheric pressure. This is done both (i) on a fundamental level with the study of the physicochemical properties of the discharge aided by Fourier transform infrared spectroscopy and laser-induced fluorescence, (ii) on a more technological level by investigating the electrical stability of the process, and (iii) from a techno-economic perspective, benchmarking the plasma-based nitrogen fixation process.

More precisely, a new approach dealing with laser-based excitation of separate rotational lines has been successfully developed. Such an approach can be implemented on atmospheric discharges that produce rather high NO_x densities where the high concentration of relevant absorbers, such as NO, imposes essential restrictions for the use of "classical" laser-induced fluorescence methods. The method is then implemented and used to provide a discussion on the two-dimensional distributions of both the gas temperature and the NO ground state density. Based on temperature map analysis, a clear correlation between the gas temperature and NO concentration is found and the effects of both the gas temperature and the plasma power on the concentrations

of NO and NO_2 produced are discussed revealing how the conversion into NO_2 is already significant in the plasma afterglow region and the input gas flow rate is a crucial parameter affecting the temperature gradients in the afterglow region.

From a technological point of view, the conventional approach of introducing external resistors to stabilize the arc is challenged by studying both the performance and the stability of the plasma replacing the external resistor with an inductor. From this work, we conclude that similar stabilization results can be obtained while significantly lowering the overall energy cost, which decreased from up to a maximum of 7.9 MJ/mol N to 3 MJ/mol N.

Finally, this thesis studies whether a hypothetical small-scale fertilizer production facility based on a rotating gliding arc plasma for nitrogen fixation can be a local competitive alternative for the Haber-Bosch process. This is done by proposing a comparative model to understand how capital expenditures, gas price, CO_2 allowances, levelized cost of energy, and transport costs affect the fertilizer production costs. The model highlights how, with the current best available technology, plasma-based nitrogen fixation, while being an interesting alternative for the synthesis of NO_x, still requires a more efficient use of H_2 for a direct production of NH_3.

Résumé

Avec la croissance de la population mondiale, le secteur agricole doit répondre à une demande croissante de nutriments. Pour ce motif, le secteur s'appuie depuis des décennies sur des engrais produits industriellement afin d'augmenter le rendement de sa production. Parmi eux, les engrais à base d'azote constituent le choix principal, bien que leur production nécessite la conversion de N_2 inerte en molécules plus réactives, telles que les oxydes nitriques NO_x ou l'ammoniac NH_3, dans le cadre d'un processus appelé "fixation de l'azote". Aujourd'hui, ce processus est principalement réalisé dans l'industrie par le célèbre procédé Haber-Bosch. Bien qu'il soit le choix dominant pour la fixation industrielle de l'azote depuis plus d'un siècle en raison d'une optimisation presque parfaite, le procédé Haber-Bosch n'est pas idéal parce qu'il nécessite des installations à grande échelle pour être rentable et qu'il est associé à un coût énergétique élevé et à des fortes émissions de CO_2, ce qui a un impact sur l'environnement qui pousse à l'étude de différentes alternatives plus vertes.

Parmi plusieurs options, la fixation de l'azote au NO_x par plasma est considérée comme une alternative prometteuse à Haber-Bosch, grâce à (i) la possibilité de mettre en œuvre la technologie à plus petite échelle, (ii) sa compatibilité avec les sources d'énergie renouvelables intermittentes, et (iii) l'absence d'émissions directes de CO_2. Dans ce contexte, un type de réacteur à plasma qui s'est révélé particulièrement approprié pour la fixation de l'azote est le plasma à arc glissant, parce qu'il fonctionne à la pression atmosphérique et favorise le transfert d'énergie vers des états d'excitation vibrationnelle, ce qui est connu pour être bénéfique pour la synthèse de NO_x, bien qu'en pratique, en raison de la température élevée dans ce "plasma chaud" (de l'ordre de 3000 K), la relaxation de la translation vibrationnelle est assez efficace, réduisant les populations des niveaux d'excitation vibrationnelle, de sorte qu'ils sont en équilibre avec la température du gaz.

Cette thèse vise à étudier la fixation de l'azote par plasma en se concentrant sur un plasma à arc glissant fonctionnant avec N_2 et O_2 à pression atmosphérique. Ceci est fait à la fois (i) à un niveau fondamental avec l'étude des propriétés physico-chimiques de la décharge en se servant de la spectroscopie infrarouge à transformée de Fourier et de la fluorescence induite par laser, (ii) à un niveau plus technologique en étudiant la stabilité électrique du processus, et (iii) d'un point de vue technico-économique, en comparant le processus de fixation de l'azote basé sur le plasma.

Plus précisément, une nouvelle approche basée sur l'excitation par laser de lignes de rotation distinctes a été développée avec succès. Cette approche peut être mise en œuvre sur des décharges atmosphériques qui produisent des densités de NO_x assez élevées où la forte concentration d'absorbeurs pertinents, tels que le NO, impose des restrictions essentielles à l'utilisation des méthodes "classiques" de fluorescence induite par laser. La méthode est ensuite mise en pratique et utilisée pour fournir une discussion sur les distributions bidimensionnelles de la température du gaz et de la densité de l'état fondamental du NO. Les effets de la température du gaz et de la

puissance du plasma sur les concentrations de NO et de NO_2 produites sont discutés et révèlent que la conversion en NO_2 est déjà significative dans la région de rémanence du plasma et que le débit du gaz d'entrée est un paramètre crucial qui affecte les gradients de température dans la région de "afterglow".

D'un point de vue technologique, l'approche conventionnelle consistant à introduire des résistances externes pour stabiliser l'arc est remise en question par l'étude des performances et de la stabilité du plasma en remplaçant la résistance externe par un inducteur. Ce travail nous permet de conclure que des résultats de stabilisation similaires peuvent être obtenus tout en réduisant de manière significative le coût énergétique global, qui est passé d'un maximum de 7,9 MJ/mol N à 3 MJ/mol N.

Enfin, cette thèse étudie si une hypothétique installation de production d'engrais à petite échelle basée sur un plasma à arc glissant rotatif pour la fixation de l'azote peut être une alternative locale compétitive pour le procédé Haber-Bosch. Pour ce faire, elle propose un modèle comparatif permettant de comprendre comment les dépenses d'investissement, le prix du gaz, les quotas de CO_2, le coût de l'énergie nivelé et les coûts de transport affectent les coûts de production de l'engrais. Le modèle met en évidence le fait qu'avec la meilleure technologie disponible, la fixation de l'azote par plasma, tout en étant une alternative intéressante pour la synthèse de NO_x, nécessite toujours une utilisation plus efficace de H_2 pour une production directe de NH_3.

Samenvatting

Met de groei van de wereldbevolking moet de landbouwsector voldoen aan een toenemende vraag naar voedingsstoffen. Om dit te bereiken vertrouwt de sector al tientallen jaren op industrieel geproduceerde meststoffen om de productieopbrengst te verhogen. Meststoffen op basis van stikstof zijn de meest gangbare keuze, hoewel voor de productie ervan inerte N_2 moet worden omgezet in meer reactieve moleculen, zoals stikstofoxiden NO_x of ammoniak NH_3, in een proces dat "stikstoffixatie" wordt genoemd. Tegenwoordig gebeurt dit in de industrie voornamelijk via het bekende Haber-Bosch-proces. Hoewel het Haber-Bosch-proces al meer dan een eeuw de dominante keuze is voor industriële stikstoffixatie omdat het bijna perfect geoptimaliseerd is, is het niet ideaal omdat het grootschalige installaties vereist om rendabel te zijn en geassocieerd wordt met hoge energiekosten en hoge CO_2-uitstoot, wat resulteert in een milieu-impact. Dit zet aan tot onderzoek naar andere, groenere alternatieven.

Van verschillende opties wordt stikstoffixatie met behulp van plasma's tot NO_x beschouwd als een veelbelovend alternatief voor Haber-Bosch, dankzij (i) de mogelijkheid om de technologie op kleinere schaal toe te passen, (ii) de compatibiliteit met fluctuerende, hernieuwbare energiebronnen en (iii) de afwezigheid van directe CO_2-emissies. In deze context is de zgn. glijdende boog (Eng: "gliding arc") plasmareactor bijzonder geschikt voor stikstoffixatie, omdat deze bij atmosferische druk werkt en de energieoverdracht naar vibrerende excitatietoestanden bevordert, waarvan bekend is dat het gunstig is voor de NO_x-synthese, hoewel in de praktijk, vanwege de hoge temperatuur in dit "warme plasma" (orde van 3000 K), de relaxatie van de vibratiemodes naar translatie vrij efficiënt is, waardoor de populaties van de vibrationeel aangeslagen niveaus afnemen, zodat ze in evenwicht zijn met de gastemperatuur.

In dit proefschrift wordt onderzoek gedaan naar plasma-gebaseerde stikstoffixatie, waarbij de nadruk ligt op een glijboogplasma dat werkt met N_2 en O_2 bij atmosferische druk. Dit gebeurt zowel (i) op een fundamenteel niveau met de studie van de fysisch-chemische eigenschappen van de ontlading met behulp van Fourier transformatie infraroodspectroscopie en laser-geïnduceerde fluorescentie, (ii) op een meer technologisch niveau door de elektrische stabiliteit van het proces te onderzoeken, en (iii) vanuit een technisch-economisch perspectief door benchmarking van het plasma-gebaseerde stikstoffixatieproces.

Er is met succes een nieuwe aanpak ontwikkeld voor de excitatie van afzonderlijke rotatielijnen door middel van lasers. Een dergelijke benadering kan worden toegepast op atmosferische

ontladingen die vrij hoge NO_x-dichtheden produceren waarbij de hoge concentratie van relevante absorbers, zoals NO, essentiële beperkingen oplegt voor het gebruik van "klassieke" lasergeïnduceerde fluorescentiemethoden. De methode wordt vervolgens geïmplementeerd en gebruikt om de twee-dimensionale verdelingen van zowel de gastemperatuur als de NO grondtoestandsdichtheid te bespreken. Op basis van 2D temperatuur-analyse wordt een duidelijke correlatie gevonden tussen de gastemperatuur en de NO-concentratie, en de effecten van zowel de gastemperatuur als het plasmavermogen op de concentraties van geproduceerd NO en NO_2 worden besproken, waarbij duidelijk wordt hoe de omzetting in NO_2 al aanzienlijk is in de zgn. nagloei van het plasma (Eng: “afterglow”) en hoe de gasstroomsnelheid een cruciale parameter is die de temperatuursgradiënten in de nagloei beïnvloedt.

Vanuit technologisch oogpunt wordt de conventionele benadering van het introduceren van externe weerstanden om de boog te stabiliseren kritisch geëvalueerd, door zowel de prestaties als de stabiliteit van het plasma te bestuderen waarbij de externe weerstand wordt vervangen door een inductor. Uit dit werk concluderen we dat vergelijkbare stabilisatieresultaten kunnen worden verkregen, terwijl de algehele energiekosten aanzienlijk worden verlaagd, nl. van maximaal 7,9 MJ/mol N naar 3 MJ/mol N.

Tot slot wordt in dit proefschrift onderzocht of een hypothetische kleinschalige kunstmestproductie installatie op basis van een roterend glijboogplasma voor stikstoffixatie een lokaal concurrerend alternatief kan zijn voor het Haber-Bosch-proces. Dit wordt gedaan door een vergelijkend model voor te stellen om te begrijpen hoe kapitaaluitgaven, gasprijs, CO_2-rechten, genivelleerde energiekosten en transportkosten de productiekosten van kunstmest beïnvloeden. Het model toont hoe, met de huidige best beschikbare technologie, stikstoffixatie op basis van plasma weliswaar een interessant alternatief is voor de synthese van NO_x, maar nog steeds een efficiënter gebruik van H_2 vereist voor een directe productie van NH_3.

Acknowledgements

Four years may seem a long period when you are in your 20s, but, as it happens for all the enjoyable things in life, my Ph.D. years felt as fast as a blink of an eye. Since the very beginning, I've been welcomed in a warm, friendly, and fertile environment that made me quickly grow both professionally and personally. I've felt at home and, for this reason, I would like to express my deepest gratitude to the many people who made this journey as special as it turned out to be.

First of all, I want to thank Rony and Annemie. This thesis would not have been possible without your help and mentoring. Whenever I was in need I always found kindness, support, and brilliant advice from you. I honestly feel extremely lucky to have had the pleasure to work with you, and I hope you can say "he was my student" as proudly as I can say that you two were my promoters!

This journey wouldn't have been as fulfilling and fun without the friends and colleagues I've met along the way. I must, of course, mention my "international" friends and colleagues Abhyuday, Omid, Kseniia, Anastasiya, Mariam, and, more generally, all the Ph.D. students and postdocs I've had the pleasure to meet in these four years. Your help has been invaluable and wide, ranging from jokes to scientific expertise. It is inevitable: our paths may diverge and separate us by hundreds or thousands of kilometers, but I will never forget you and what we went through together. A special thank goes to the "équipe d'intégration accélérée": Nathan, Philippe, Loïc, Pierre, and Robin! You've welcomed me as one of you from the very first moment. What started as simply enjoying some time together after work quickly became a deeper bond, traveling together, discussing our problems, and cheering about each other successes. I honestly cannot put into words how grateful I am for all these experiences and. If now I feel so attached to Mons, it is mostly because of you! And of course, I have to thank Marco, Claudio, Giacomo, and Samuele: the Italian community of UMons, mostly located at CMN. You all contributed greatly to make me feel at home! A special thanks goes to a really dear friend of mine, Leonardo, for his long distance support through all my misadventures in these years.

Infine, un ringraziamento di cuore va ai miei genitori Antonia e Vanni, a mio fratello Daniele e alla sua famiglia. Mi avete sempre supportato, in tutti i modi possibili, e ve ne sono più che grato. Il percorso che ho superato, dopo anni e anni di fatica, non sarebbe stato possibile senza di voi!

I'm sorry if I forgot to thank any of the people I should have mentioned. But, if you cared enough to read through these lines, then, you deserve to be thanked as well!

Grazie a tutti!

Filippo

List of Publications

Peer-reviewed Journals:

[1] O. S. Bahnamiri, F. Manaigo, A. Chatterjee, R. Snyders, F. A. D'Isa and N. Britun, "Investigation of nitrogen fixation in low-pressure microwave plasma via rotational-vibrational NO and N_2 kinetics", *J. Appl. Phys.* 133, 113303 (2023).

[2] F. Manaigo, O. S. Bahnamiri, A. Chatterjee, A. Panepinto, A. Krumpmann, M. Michiels, A. Bogaerts and R. Snyders, "Electrical stability and performance of a Nitrogen-Oxygen atmospheric pressure gliding arc plasma", submitted (2023)

[3] F. Manaigo, K. Rouwenhorst, A. Bogaerts and R. Snyders, "Feasibility study of a small-scale fertilizer production facility based on plasma nitrogen fixation", *Energy Convers. Manag.* 302 (2024) 118124

[4] F. Manaigo, A. Chatterjee, A. Bogaerts and R. Snyders, "A new insight on NO synthesis in a gliding arc plasma via gas temperature and density mapping by laser-induced fluorescence.", submitted (2024)

International conferences and workshops:

[1] F. Manaigo, O. S. Bahnamiri, A. Chatterjee, A. Bogaerts and R. Snyders, "Nitrogen fixation in a N_2-O_2 Gliding Arc plasma, an optical emission and IR absorption spectroscopy study", *Solvay Workshop on Plasma Technology and Other Green Methods for Nitrogen Fixation*, Bruxelles, Belgium, November 15-17, 2021.

[2] F. Manaigo, O. S. Bahnamiri, A. Chatterjee, A. Bogaerts and R. Snyders, "NO_x synthesis and discharge stability in a Gliding Arc Plasmatron", *The 5th International Symposium on Plasmas for Catalysis and Energy Materials (ISPCEM)*, Liverpool, UK, July 3-7, 2022.

[3] O. S. Bahnamiri, F. Manaigo, A. Chatterjee, R. Snyders and N. Britun, "Insight into nitrogen fixation kinetics in a pulsed microwave discharge", *The 5th International Symposium on Plasmas for Catalysis and Energy Materials (ISPCEM)*, Liverpool, UK, July 3-7, 2022.

[4] F. Manaigo, O. S. Bahnamiri, A. Chatterjee, A. Bogaerts and R. Snyders, "NO_x synthesis and discharge stability in a Gliding Arc Plasmatron", *The 18th International Conference on Plasma Surface Engineering (PSE)*, Trade Fair Erfurt, Germany, September 12-15, 2022.

[5] O. S. Bahnamiri, F. Manaigo, A. Chatterjee, R. Snyders and N. Britun, "Insight into nitrogen fixation kinetics in a pulsed microwave discharge", *The 18th International Conference on Plasma Surface Engineering (PSE)*, Trade Fair Erfurt, Germany, September 12-15, 2022.

[6] F. Manaigo, A. Bogaerts and R. Snyders, "Feasibility study of a plasma based local fertilizer production", *Non-Thermal Plasmas for Sustainable Chemistry, Wilhelm and Else Heraeus-Stiftung*, Physikzentrum Bad Honnef, Germany, April 23-27, 2023.

[7] F. Manaigo, A. Chatterjee, A. Bogaerts and R. Snyders, "Characterization of an atmospheric N_2-O_2 Gliding Arc Discharge by LIF", *25th International Symposium on Plasma Chemistry (ISPC25)*, Miyako Messe Kyoto, Japan, May 21-26, 2023.

Contents

List of Figures

List of Tables

List of Acronyms and Symbols

$A(\nu)$	Absorbance
$A_L(\nu)$	Line absorption
A_{ij}	Probability of spontaneous emission
AC	Alternate current
CapEx	Capital Expenditures
CCD	Charge-couple device
d	Depreciation period
DBD	Dielectric barrier discharge
DC	Direct current
E_{las}	Laser beam energy
e	Electron charge
F	Input gas flow rate
FTIR	Fourier transform infrared
GA	Gliding arc
GAP	Gliding arc plasmatron
H-B	Haber–Bosch
I_{ji}	Emission intensity
I_{las}	Laser intensity
I_{LIF}	LIF signal intensity
ICCD	Intensified charge coupled device
J	Rotational quantum number
k_B	Boltzmann constant
L	Inductance in series with the GAP
LIF	Laser-induced fluorescence
MW	Microwave
n_e	Electron density
n_i	Ion density
n_n	Neutral particle density
NF	Nitrogen fixation
OES	Optical emission spectroscopy
OpEx	Opertional Expenditures
P_a	Annual production
P_P	Plasma power

P_T	Total power
R	Resistance in series with the GAP
RGA	Rotating gliding arc
$T(\nu)$	Transmittance
T_e	Electron temperature
T_{rot}	Rotational temperature
T_{vib}	Vibrational temperature
V_B	Breakdown voltage
ϵ_0	Vacuum permittivity
λ_D	Debye length
ν	Vibrational quantum number
τ	Decay time

Foreword

Nitrogen (N) is an essential component for any living organism as it is necessary for the formation of amino acids, nucleic acids, and other constituents. In nature, nitrogen is abundant and it is mostly found in its molecular form as N_2, making up for 78% of the atmosphere. However, due to the high energy needed to break its strong triple bond (9.756 eV bond dissociation energy [1]), the nitrogen atoms in the N_2 molecule cannot be directly accessible to most of the living organisms and must be converted into more reactive N-containing compounds in a process known as "nitrogen fixation" (NF). In nature, NF is usually performed by a few species of bacteria or by lightning, an example of a hot plasma discharge.

In this context, as both the world population and the per capita food consumption increase, the nutrient demand on the agricultural sector follows accordingly. Thus, the amount of fixated nitrogen naturally produced is not enough. Therefore, in 2000, almost half of the world population was fed thanks to industrial N fertilizers [2]. While the use of organic fertilizers did not record a significant increase in the last 50 years, the industrially produced inorganic fertilizer sector constantly grew with an average compound annual growth rate of 6.3 % from 1961 to 1988 and of 1.6 % from 1994 [3]. Inorganic fertilizers are classified according to the percentage in weight of the main nutrient, usually nitrogen (N), phosphorus (P), or potassium (K). Nitrogen fertilizers are the most commonly used accounting for 59 % of the global fertilizer production, especially in the EU where 73 % of the inorganic fertilizers produced are nitrogen-based [4]. Commercially available fertilizers are characterized by the weight percentage of their main nutrient(s) and common nitrogen-based fertilizers usually consist of ammonium nitrate (NH_4NO_3 - 35 %N), urea (CH_4N_2O - 47 %N) or urea ammonium nitrate (UAN - 28-32 %N) which is a solution of the two in water. In the EU, the average consumption per hectare of cropland strongly varies from approximately 60 kg/ha of N in the southern member states (Portugal, Italy, Greece, and Spain) up to 200 kg/ha of N in the Benelux region [5].

Today, the demand for industrially fixated nitrogen is met via the Haber-Bosch (H-B) process, which allows for the catalytic synthesis of NH_3 from N_2 and H_2, at high temperatures (650 K - 750 K) and high pressures of around 100 bars [6]. The process greatly benefits from an economy of scale and, thus, is mainly performed in large centralized H-B facilities [7]. Given the large scale in which it is globally used and despite its good energy efficiency, the H-B process currently consumes approximately 1% of the world energy production and, combined with the H_2 production by steam methane reforming (SMR), emits around 300 million tons of carbon dioxide (CO_2) each year [8], which corresponds to approximately 1% of the CO_2 emissions in 2019 [9]. These figures

highlight the necessity of developing alternative NF processes that would allow for lower energy consumption and a reduced environmental impact.

In this context, plasma-based NF approaches are gaining a lot of interest as a complementary method for the production of reactive nitrogen-based molecules, with an energy-cost-effective production of nitrogen compounds, especially nitrogen oxides (NO_x) [10]. On paper, plasma-based technology offers several potential advantages, namely,

- a lower theoretical energy consumption, predicted to be 0.2 MJ/mol of fixated nitrogen (MJ/mol N) [6]. This limit is lower than both the current best available technology reported for the H-B process (0.49 MJ/mol N) and its theoretical limit (0.35 MJ/mol N).
- no direct CO_2 emission is associated with plasma-based NF. Additionally, the relative ease of switching on and off a plasma reactor allows for the implementation of the technology with intermittent renewable energy sources, further improving the environmental impact of the technology.
- given the milder pressure and temperature requirements compared to the H-B process, the process can be implemented at a much smaller and local scale compared to H-B-based fertilizer production plants [11], thus reducing transportation costs.

Despite the potential advantages of plasma-based NF, in the last few decades, the technology has not seen a wide industrial implementation yet as it still suffers from low yields and a too high energy cost, far from the theoretical limit for the technology. There is, therefore, a strong incentive to improve the knowledge of this technology, both on a fundamental level and on an economic feasibility one.

In this context, this thesis focuses on improving the understanding of the plasma-based NF, focusing on nitrogen oxidation, in gliding arc plasmatrons (GAPs), which are particularly promising for gas conversion as they operate at atmospheric pressure, making them easy to be implemented on an industrial scale.

Thesis outline

Chapter 1, entitled "**The role of nitrogen fixation**", aims to provide a brief introduction on the history and role of NF in the current food production landscape.

Chapter 2, "**Plasma-based nitrogen fixation**" provides a general introduction to plasma discharges, the role of vibrational excitation in the context of non-thermal plasma NF, and an overview of the main types of discharge used in literature. Finally, the state-of-the-art for plasma-based NF and the research strategy in the framework of the "NITROPLASM" project, which this thesis is part of, are discussed.

In Chapter 3, entitled "**Setup and Methodology**", a detailed description of the experimental setup is provided. The design of the GAP reactor used as well as the optical diagnostic tools and their basic principles are discussed.

The high concentration of relevant absorbers, such as NO, may impose essential restrictions for the use of "classical" laser-induced fluorescence methods (dealing with excitation in the band-head vicinity), as the laser beam would be strongly absorbed along its propagation in the discharge. In Chapter 3, "**Laser-induced fluorescence-based characterization of the afterglow**", a new approach dealing with laser-based excitation of separate rotational lines is proposed and used to provide simultaneous and reliable measurements of both the NO density and the gas temperature in the GAP afterglow. Such a method is further utilized to investigate how both the gas temperature and the plasma power can affect the concentrations of NO and NO_2 produced.

The conventional approach to stabilize a GAP is to use external resistors. Although this indeed allows for an enhancement of the plasma stability, very little is reported about how it impacts the process efficiency, both in terms of NO_x yield and energy cost. Chapter 5, entitled "**Electrical stability and performances**", focuses on addressing this question by studying the effect of external resistors on both the performance and the stability of the plasma. As an alternative approach, it is demonstrated that the replacement of the resistor by an inductor is promising since it allows to stabilize the plasma without affecting either the energy cost of the process nor the NO_x yield.

Plasma-based NF is often presented as a technology that could be implemented at a small local scale. Chapter 6, entitled "**Feasibility study of a small-scale fertilizer production facility**", aims to verify this assumption by studying the economic feasibility of a small-scale nitrogen fertilizer facility that uses plasma-based technology and comparing it with the H-B process. Capital expenditures, gas price, CO_2 allowances, levelized cost of energy, and transport costs are considered in this comparative model which is used to understand the impact of such parameters on the fertilizer production costs.

Chapter 7, "**General conclusions and perspectives**" provides the overall conclusions of the thesis, highlighting the main achievements and expanding on the future perspectives of plasma-based NF.

Chapter 1

The role of nitrogen fixation

This chapter provides a general discussion on industrial nitrogen fixation. A strong focus is dedicated to the discussion of the Haber-Bosch process, which is the dominant method for the production of fixated nitrogen.

1.1 Nitrogen Fixation

Nitrogen (N) is a crucial element, which is essential for the formation of amino acids, nucleic acids, and other constituents required by any living organisms. As an example, daily, an average person consumes almost 11 g of nitrogen [12]. Nitrogen is abundant in nature in its molecular form N_2, which is inert due to the high energy associated with its strong triple bond (9.756 eV bond dissociation energy [1]). For this reason, most living organisms cannot directly access the nitrogen in the N_2 molecule and therefore rely on more reactive N-containing compounds, such as nitric oxide (NO), nitrogen dioxide (NO_2), ammonia (NH_3), etc. The process of synthesizing N-containing compounds is known as "nitrogen fixation" (NF).

NF can occur naturally thanks to lightning strikes or to a few species of bacteria that can be found either in the soil (e.g. Azotobacter and Clostridium), or in the nodules of the roots of leguminous plant species, where they form a symbiotic relationship (e.g. Rhizobium and Bradyrhizobium) [13]. Nitrogen compounds can be recycled from organic matter (such as manure, plant residues, etc...) through mineralization. A part of the nitrates (NO_x) is anaerobically reconverted to N_2 by a diverse group of bacteria. This process is known as denitrification and can take place mostly in the soil or in anoxic water [14]. An excess of nitrates in the soil can pollute nearby water reserves and have undesirable consequences, such as eutrophication, i.e. the excessive enrichment of a body of water that typically results in algal blooms that can lead to fish die-offs. This "cycle" is briefly illustrated in figure 1.1.

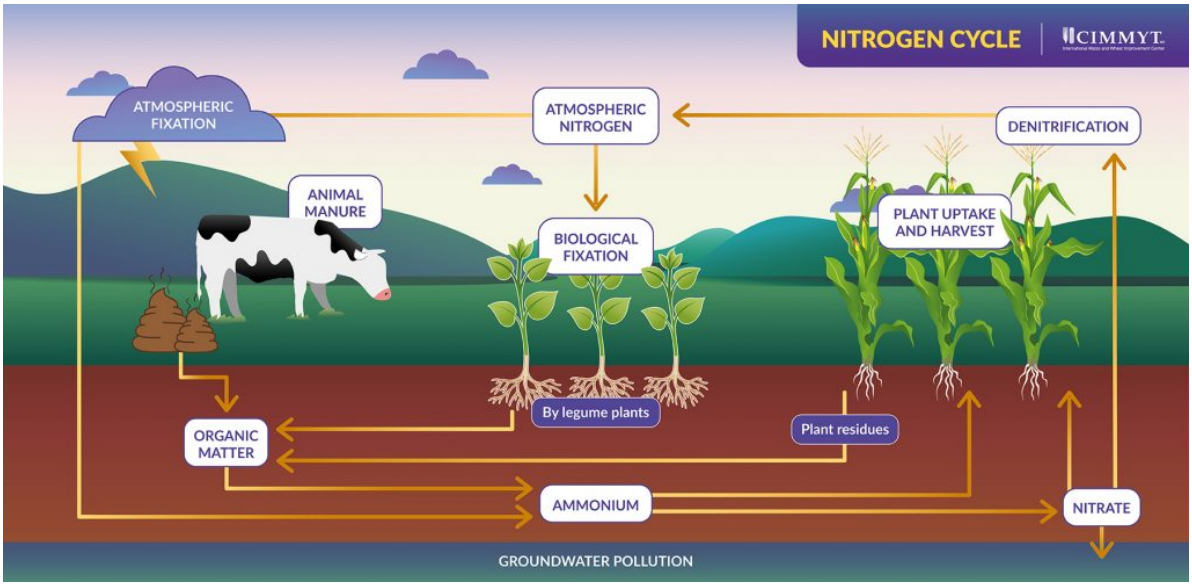

Figure 1.1: Simplified diagram illustrating the nitrogen cycle. Reprinted from [15].

However, the naturally occurring NF, alone, cannot sustain the current demand for nutrients, which has increased with the world population and the per capita food consumption. As a result, agriculture grew more and more dependent on nitrogen recycling through manure and on the use of industrially produced fertilizers to prevent soil denitrification and crop failures. In the EU, as

an example, the average consumption per hectare of cropland strongly varies from approximately 60 kg/ha of N in the southern member states (Portugal, Italy, Greece, and Spain) up to 200 kg/ha of N in the Benelux region [5]. Globally, the world demand for nitrogen is of the order of 100 million tons of main nutrient (N). Table 1.1 shows the global demand for fertilizers, per nutrient type, reported in [16].

Table 1.1: Global demand for fertilizers in thousand tonnes of main nutrient. Data from a 2019 report from the Food and Agriculture Organization of the United Nations (FAO) [16].

Year	2016	2017	2018	2019	2020	2021	2022
Nitrogen, N	105 148	105 050	105 893	107 424	108 744	110 193	111 591
Phosphorus, as P_2O_5	44 481	45 152	45 902	46 587	47 402	48 264	49 096
Potassium, as K_2O	35 434	36 249	37 171	37 971	38 711	39 473	40 232
Total (N + P_2O_5 + K_2O)	185 063	186 551	188 966	191 981	194 857	197 930	200 919

1.2 Industrial nitrogen fixation

Having discovered the role of nitrogen in agriculture in the late first half of the 19^{th} century, the European demand for sources of nitrogen quickly grew. This demand was met, in the second half of the 19^{th} century, by two imports from South America: guano and Chile saltpeter.

Guano, i.e. the excrement of seabirds, required three main conditions for the formation of large high-quality deposits: an arid climate to avoid the dispersion of soluble nutrients, large colonies of nesting seabirds, and the abundance of fish [17]. This made South America (especially Peru) the ideal location for the formation of large-scale deposits. Guano was the main source of fixed nitrogen in Europe until the 1870s when the peak of its production was reached. In that decade, Britain alone imported approximately 280 000 tons per year. The scarcity in the supply pushed the Peruvian government to place restrictions on guano exports in the following years, effectively limiting its production for domestic use only [18]. Further South, in Chile, huge deposits of sodium nitrate ($NaNO_3$ - also known as "Chile saltpeter") were discovered. Large-scale extraction quickly began as the high-quality guano deposits became unavailable. Concerns over the long-term availability of the deposits were raised as a too conservative estimation had predicted that deposits would reach depletion in the 1930s [17]. As a result, more and more scientists were pushed to study new ways of producing N-based fertilizers. The evolution of the annual production of fixated nitrogen from natural sources and from the industrial processes discussed in the following sections is shown in figure 1.2.

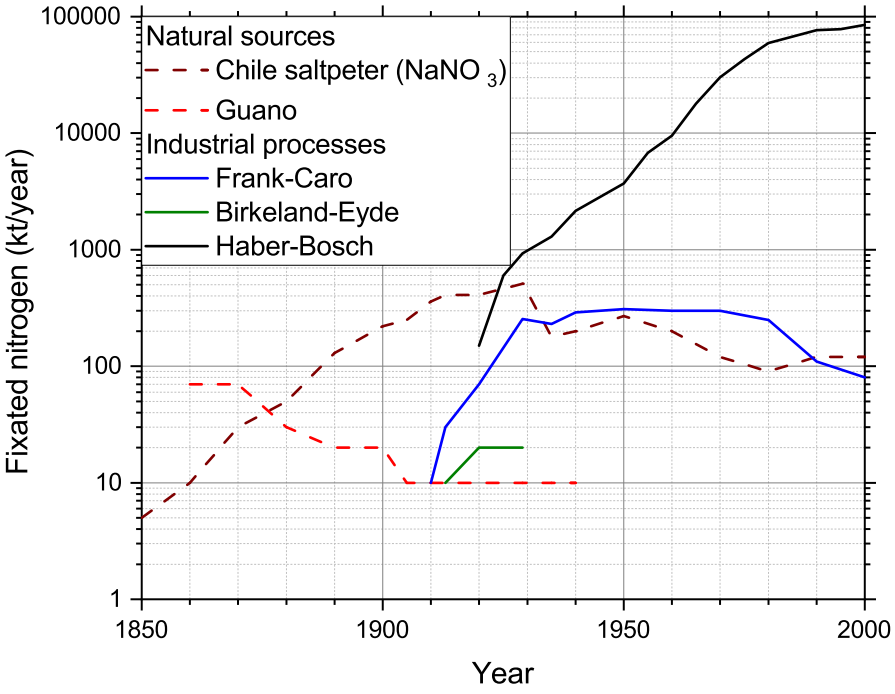

Figure 1.2: Time evolution of the annual production of fixated nitrogen (expressed in kt of the main nutrient, N) divided per method. Data from [17], readapted from[19].

1.2.1 The Cyanamide process

The Cyanamide process, also known as the Frank-Caro process, was discovered in the 1890s. Calcium carbonate ($CaCO_3$) and carbon coke reacted in an electric furnace to form calcium carbide (CaC_2) with the following reactions

$$CaCO_3 \rightarrow CaO + CO_2, \tag{1.1}$$

$$CaO + 3C \rightarrow CaC_2 + CO. \tag{1.2}$$

The calcium carbide could then be heated at around 1400–1900 K in order to react with N_2 and form calcium cyanamide ($CaCN_2$) [20]. In terms of energy cost the lowest reported energy consumption was approximately 1.9 MJ/mol [6].

The earliest large-scale cyanamide facility based on the Frank-Caro process was built in 1905 in Piano d'Orta, Abruzzo, Italy, and had an annual capacity of 500 t-$CaCN_2$. Figure 1.3 shows an image of the cyanamide facility built, a couple of years later, on the Canadian side of Niagara

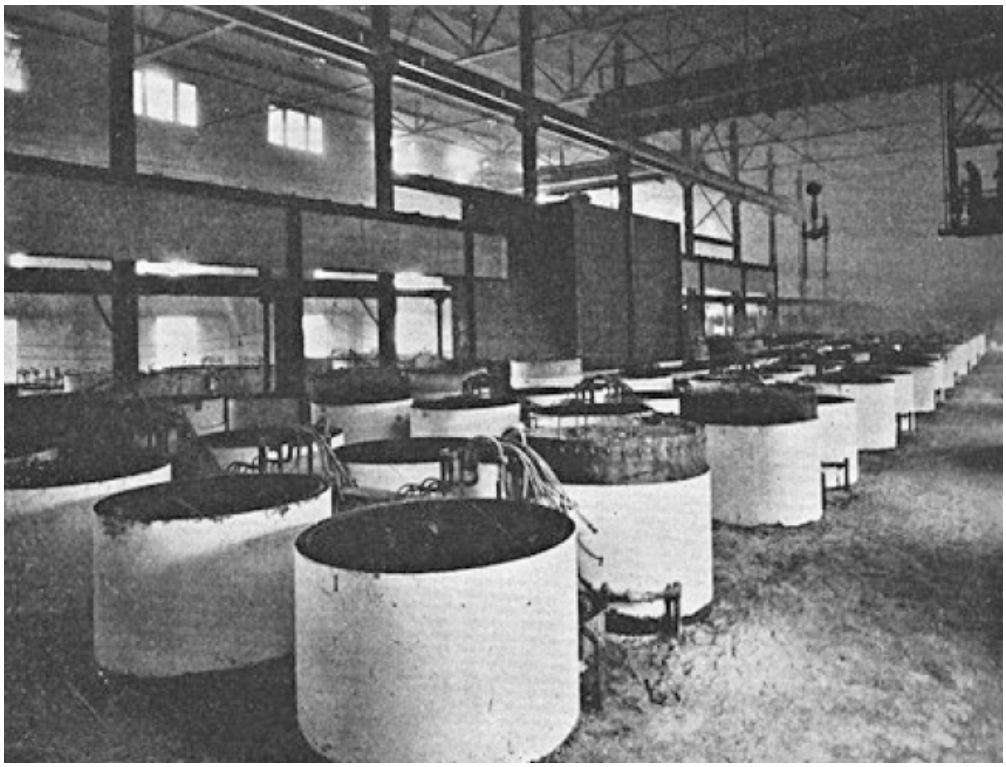

Figure 1.3: Cyanamid furnaces, Niagara Falls. Reprinted from [18, 20]

Falls. The initial annual capacity of this facility was 5000 t-$CaCN_2$, which was later expanded to 25 000 t-$CaCN_2$ [18, 20].

1.2.2 The Birkeland-Eyde process

In 1903, Birkeland and Eyde developed a process based on a thermal plasma to fixate nitrogen into nitrogen oxides (NO_x). Air was injected in an electric arc formed between two electrodes inside a circular 2 m wide furnace. The arc was supplied with alternating current in a magnetic field, forcing the arc to elongate semi-circularly, covering a wider area. The resulting gas mixture was then rapidly quenched to prevent the decomposition of the oxide. The cooled NOx then was passed through an oxidation chamber and finally captured in water to form diluted HNO_3. The acid was then reacted with limestone to form calcium nitrate, which could be used as a fertilizer.

The first large-scale applications of the Birkeland-Eyde process were developed in the South of Norway. As an example, the factory in Rjukan which was equipped with 120 furnaces and was powered by a nearby hydroelectric power plant is shown in figure 1.4. This process obtained energy efficiencies of about 2.4-3.1 MJ/mol of fixated nitrogen producing a gas mixture with up to 1-2% of NO [19–21].

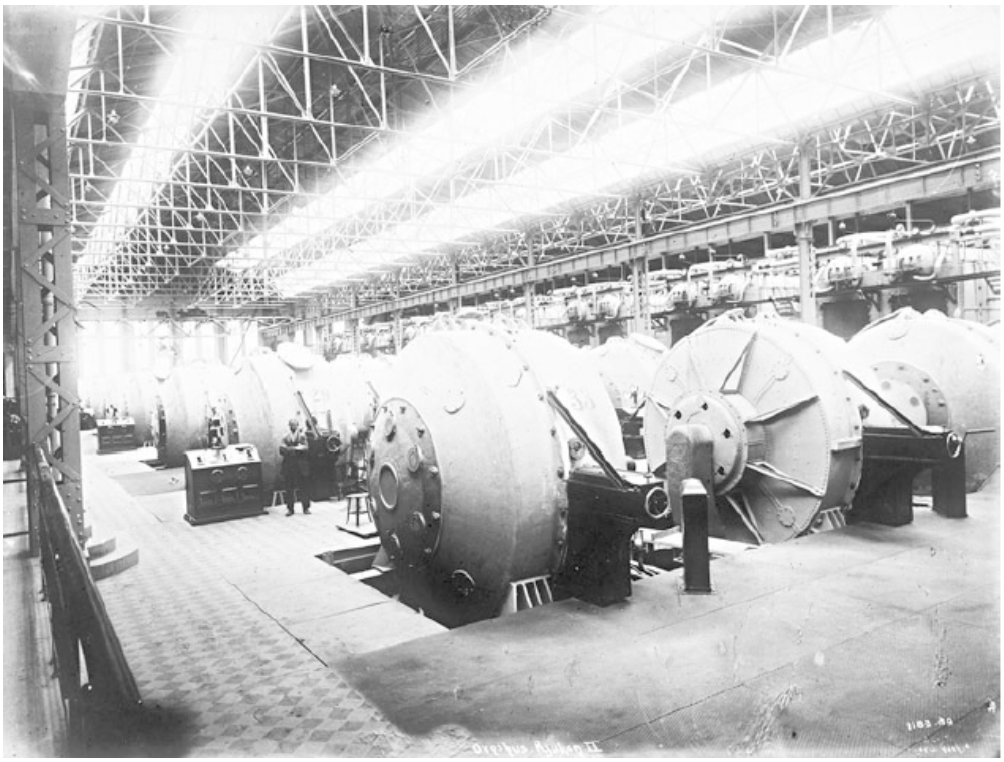

Figure 1.4: Birkeland-Eyde furnaces, Rjukan, 1912. Reprinted from [18, 20]

1.2.3 Haber-Bosch process

A new industrial process for industrial NF would be developed, in 1909, by the German physical chemist Fritz Haber, who discovered a method for the synthesis of NH_3 from N_2 and H_2 at high pressure and temperature with an osmium catalyst.

$$N_2 + 3H_2 \leftrightarrow NH_3, \qquad \Delta H = -46.14\,\text{kJ/mol} \tag{1.3}$$

The H_2 was produced through coal gasification. A few years later, in 1913, thanks to the combined effort with the industrial chemist Carl Bosch at BASF (Badische Anilin und Soda Fabrik), the process was upscaled for the industrial manufacture of nitrogen fertilizer, and has, since then been known with the name of Haber-Bosch (H-B) process. However, due to the proximity with the First World War, the first industrial applications of the H-B process consisted in the manufacture of nitrates necessary for the production of explosives, such as TNT or picric acid, for the Kaiser's armed forces [20]. The discovery and development of the H-B process earned a Nobel prize in 1918 to Fritz Haber, but not without controversies due to his major role in the German chemical warfare program: to Fritz Haber is attributed the idea of weaponizing chlorine gas, first used in the second battle of Ypres, Belgium (mid-April 1915) [20]. Thank to its efficiency, the H-B process quickly consolidated as the dominant and cheapest process, replacing its competitors.

Figure 1.5 shows the comparison between the recorded world population and its prediction

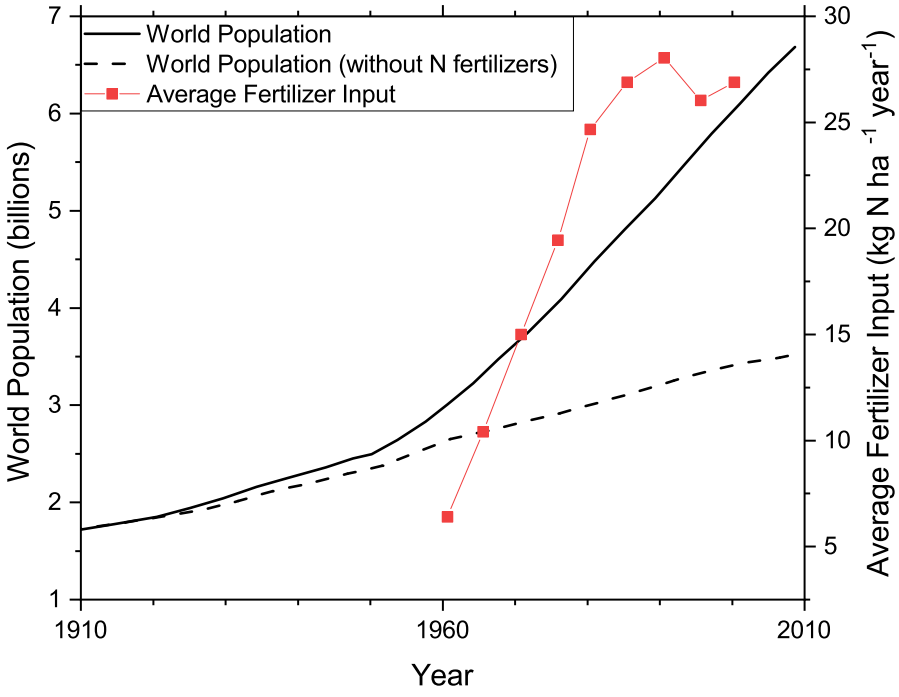

Figure 1.5: Recorded world population per year (black solid), its prediction without the N fertilizers produced via the H-B process (black dashed), and the average yearly fertilizer input per acre (red). Adapted from [2].

without industrial N-based fertilizers. It is currently estimated that about half of the world population is fed thanks to the H-B process. Over the last century, the H-B process was greatly optimized, seeing a reduction of its energy cost from more than 1 MJ/mol of fixated nitrogen (MJ/mol N) which was necessary in the 1950s to the current best result of 0.49 MJ/mol N [6, 22]. Nowadays the H-B is still the dominant process for NF. In its most commonly implemented design, which is schematized in figure 1.6, the H-B process can be divided into two main steps: the synthesis of H_2 and the synthesis of NH_3.

The main component of the NH_3 production stage is the H-B reactor which, with the current designs, uses iron catalysts and requires temperatures of 650 K-750 K and high pressures of about 100 bar to maximize its efficiency [6, 22]. The produced NH_3 is then separated by condensation and the unreacted N_2 and H_2 are recycled and reinjected in the reactor.

In the H_2 production stage, H_2 is produced from natural gas through Steam Methane Reforming (SMR),

$$CH_4 + H_2O \leftrightarrow CO + 3H_2, \qquad \Delta H = 206\ \text{kJ/mol} \tag{1.4}$$

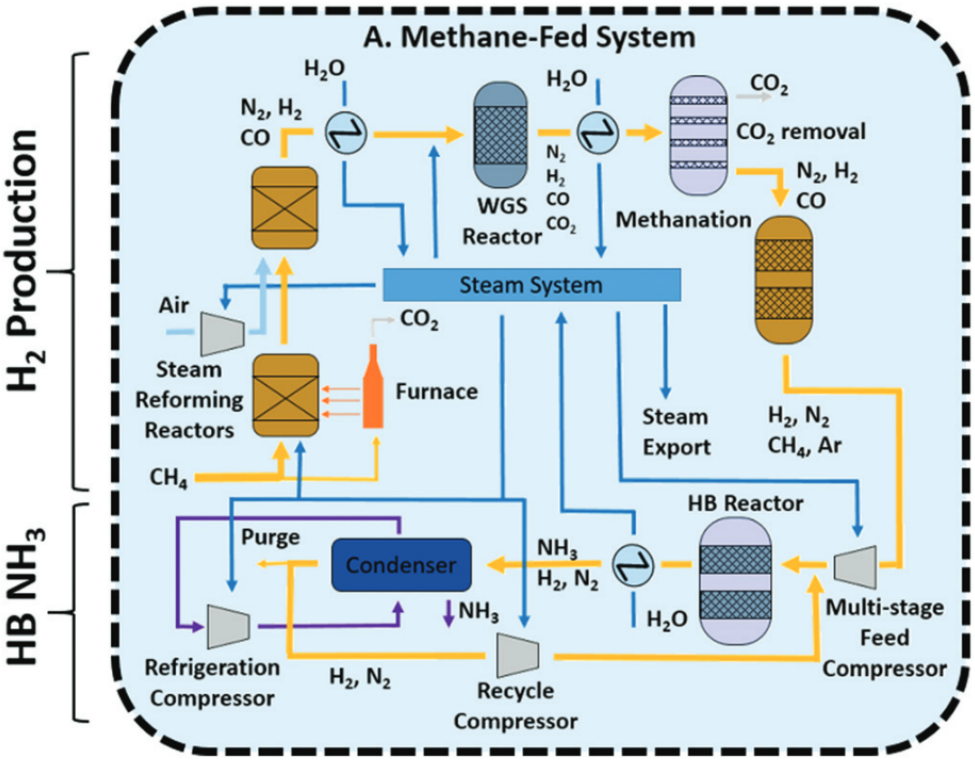

Figure 1.6: Schematics of a typical H-B process combined with SMR. Reprinted from [22].

for which the optimal operating conditions consist of pressures between 20 and 30 bars and temperatures between 1000K and 1200K. The process usually happens in two stages. The energy required for the reaction can be provided by methane combustion in an external furnace. Compressed air is then fed to provide the N_2 necessary for the NH_3 production stage. An additional H_2 molecule is released through the water gas shift (WGS) reaction (equation (1.5)), which is exothermic, thus requiring heat to be removed to minimize the CO concentration at equilibrium [22].

$$CO + H_2O \leftrightarrow CO_2 + H_2, \qquad \Delta H = -41 \text{ kJ/mol} \tag{1.5}$$

The CO_2 is then removed and the remaining CO is reconverted to CH_4 through methanation to avoid polluting the catalyst in the NH_3 production stage [22]. The compressors, required throughout the H-B process can be powered by steam turbines utilizing the waste heat from the SMR reactors [22]. Considering the pressure and temperature requirement, both the H-B and SMR greatly benefit from an economy of scale and, thus, are performed at large-centralized facilities. The effect of a large production capacity on the overall energy cost of the H-B process is shown in figure 1.7.

The typical ammonia plant, performing both the SMR and the H-B processes, produces between 200 kt and 1200 kt of NH_3 per year [31], which is enough to supply an order of magnitude of 100 000 km^2 of arable land in the EU.

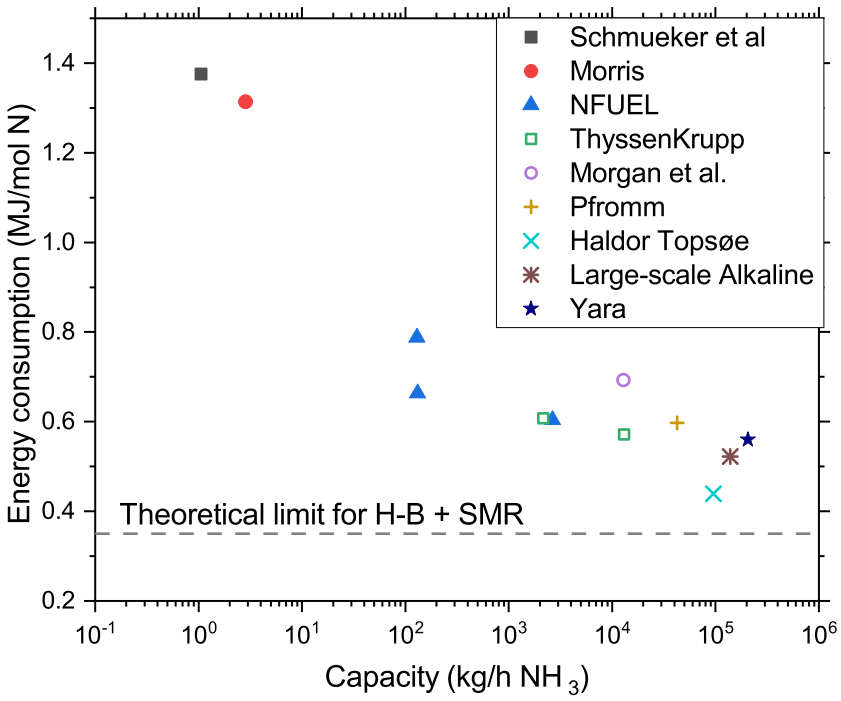

Figure 1.7: Energy consumption of the H-B process as a function of the production capacity. Adapted and modified from [23]. Original data references [24–30].

1.2.4 Fertilizer production chain

In a nitrogen-based fertilizer production facility, all the production steps are covered, starting from SMR and H-B. Figure 1.8 shows, as an example, a picture of a nitrogen fertilizer production facility in Sluiskil (NE) owned by Yara. The facilities dedicated to each of the production steps, as well as its port for international shipping are highlighted.

Part of the NH_3 produced via the H-B process undergoes oxidation through the Ostwald process where it is first converted into NO in the presence of a rhodium–platinum gauze [19].

$$4NH_3 + 5O_2 \rightarrow 4NO + 6H_2O, \qquad \Delta H = -905\ \mathrm{kJ/mol} \tag{1.6}$$

Ammonia oxidation is usually performed at approximately 1000 K and in a pressure range between 4–10 atm [19] but could be performed at atmospheric pressure [32]. The NO then passes through a cooling chamber where it reaches a temperature of 330 K and is oxidized into NO_2

$$2NO + O_2 \rightarrow 2NO_2, \qquad \Delta H = -114\ \mathrm{kJ/mol} \tag{1.7}$$

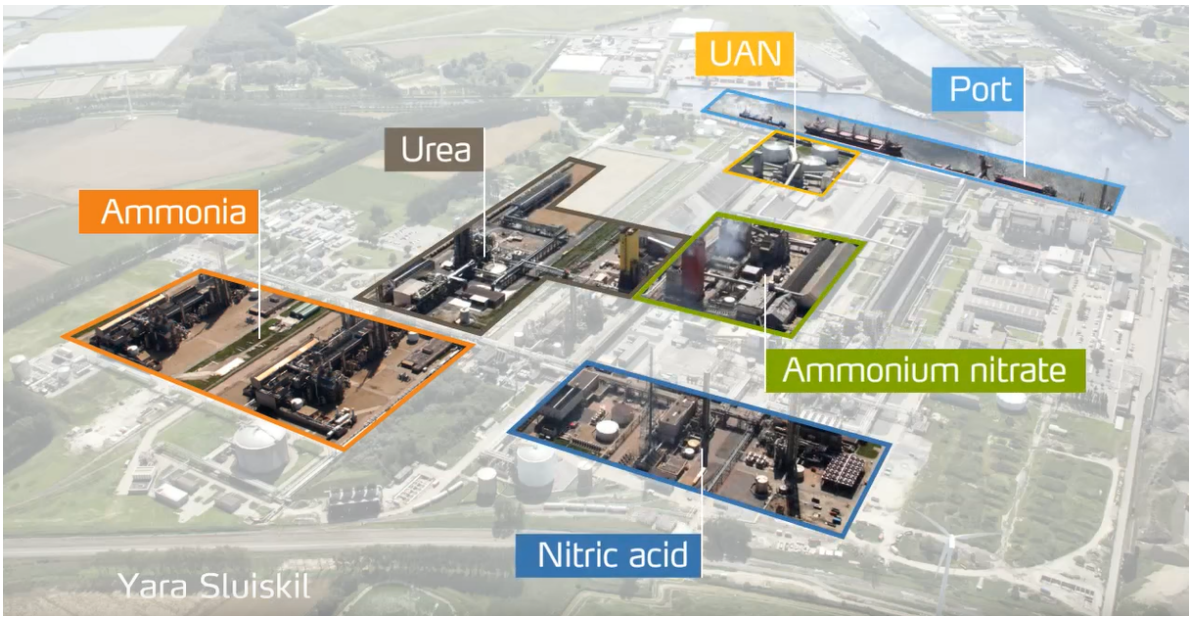

Figure 1.8: Picture of the nitrogen fertilizer production facility in Sluiskil (NE), reprinted from Yara

which is finally absorbed into water to form nitric acid (HNO_3) in an absorption column. The earliest HNO_3 absorption plants consisted of a series of, approximately 20 m high water sprayers towers filled with broken quartz.

$$3NO_2 + H_2O \rightarrow 2HNO_3 + NO, \qquad \Delta H = -117\,\text{kJ/mol} \tag{1.8}$$

The NO is then recycled and re-injected into the oxidation phase. The NO_2 absorption in water is usually performed in a pressure range between 3 and 6 bar (but higher pressures of 8-9 bar can also be applied)[32].

Finally, preheated HNO_3 is combined with compressed NH_3 to obtain NH_4NO_3 by pressure neutralization. The typical working conditions are approximately 4.5 bar and 450 K [32].

$$HNO_3 + NH_3 \rightarrow NH_4NO_3, \qquad \Delta H = -146\,\text{kJ/mol} \tag{1.9}$$

The NH_4NO_3 is then sold to retail sellers as a fertilizer in the form of pellets.

As an alternative, NH_3 can be pumped with compressed CO_2 in order to form ammonium carbamate ($[NH_2CO_2][NH_4]$) which then can condense into urea ($(NH_2)_2CO$).

1.3 Current challenges

Despite dating back to 1910, the H-B process remains to this day the most efficient industrial process to produce fixated nitrogen but is recognized to be environmentally impacting. The H-B and SMR processes combined are responsible for most of the nitrogen-based fertilizer production energy cost and CO_2 emissions. While the lowest reported energy cost for the H-B process is 0.49 MJ/mol N [6, 31], the average performances of the technology correspond to an energy cost of 0.65 MJ/mol N and a CO_2 emission of 2.16 t per t of NH_3 [33]. In 2019, 185 Mt of NH_3 have been produced and the nitrogen-based fertilizer industry was recorded to be globally responsible for approximately 1% of the world energy consumption and 1% of the world total CO_2 emissions [31]. As the energy cost for the HB process is strongly affected by its production scale, the process is currently performed in large-scale facilities in order to optimize its efficiency [7, 23]. This affects the logistics of the fertilizer industry which, considering the amount of arable land that the typical fertilizer production facility can sustain (Approximately 100 000 km^2. See section 1.2.3), can likely be required to cover distances of the order of 100-1000 km. For these reasons, it is therefore necessary to develop alternative NF processes that would allow for lower energy consumption and a reduced environmental impact.

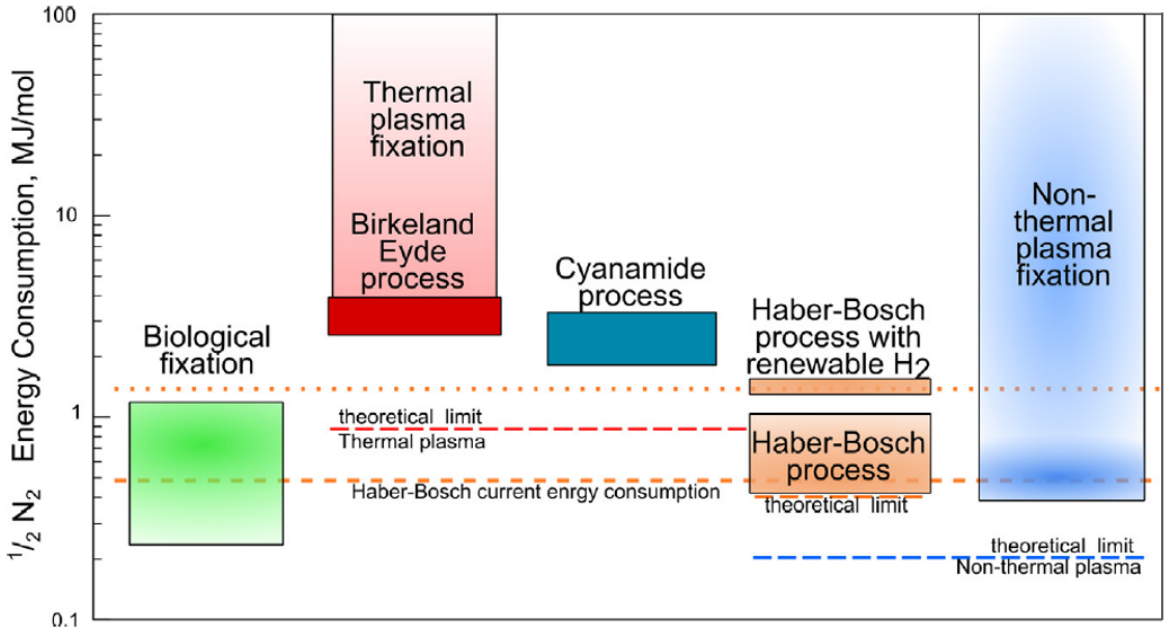

Figure 1.9: Comparison of the energy cost for NF for different processes. Adapted from [6]

In the quest for finding an alternative, plasma-based NF is gaining a lot of interest as, in theory, it would allow to overcome these issues. From an energy consumption perspective, it has been reported that the theoretical limit for the energy consumption for N_2 oxidative fixation with non-thermal plasmas is approximately 0.2 MJ/mol, which is significantly lower than the current energy consumption reached with the H-B process [6]. This is shown in figure 1.9, where the energy consumption of the main competitors for NF is visually summarized. Additionally, a

plasma-based NF process would allow for the production of fixated nitrogen with no direct CO_2 emissions. Moreover, the relative ease of switching on and off plasma reactors and the milder pressure and temperature requirements of the process would allow for a smaller, localized, implementation which would be compatible with the use of intermittent renewable energy sources.

Chapter 2

Plasma-based nitrogen fixation

This chapter introduces the fundamental concepts for a variety of topics necessary to understand the following discussion on plasma-based NF. An introduction to plasma, from its definition to some of its characteristics, is provided and the basics of the chemistry behind the plasma-based NF process, as well as a description of the principal plasma reactors, are discussed. Finally, an in-depth discussion on the state-of-the-art is provided, and from that, the motivation, the objective, and the strategy of the thesis are defined.

2.1 Plasma Basics

Plasma is a common state of matter that is often described as an ionized gas containing neutral particles, electrons, ions, and free radicals. It is the most abundant state of matter found in the universe as, for example, stars themselves are plasmas. A classic textbook definition is that plasma is a *quasi-neutral* gas of charged particles characterized by a *collective behavior* [34–36]. The concept of quasi-neutrality implies that, despite containing charged particles, the number densities of electrons and ions in a plasma are locally balanced. The collective behavior, on the other hand, arises due to the long range of the $1/r$ Coulomb potential and causes each charged particle in a plasma to interact with a large number of other charged particles. Quasi-neutrality can be considered a consequence of the collective behavior in a plasma as microscopic fluctuations are shielded in a large enough plasma region. The typical characteristic length required for the charged particles to shield one another is known as the Debye length λ_D, which is defined as [34]:

$$\lambda_D = \left(\frac{\epsilon_0 k_B T_e}{e^2 n_e} \right)^{1/2}, \tag{2.1}$$

where ϵ_0 is the vacuum permittivity, k_B is the Boltzmann constant, T_e is the electron temperature, e is the electron charge and n_e is the electron density. An ideal plasma has many charged particles in a sphere with radius λ_D, i.e.

$$n_e \frac{4\pi}{3} \lambda_D^3 \gg 1. \tag{2.2}$$

T_e, used in equation (2.1) is an important parameter of the plasma that can be measured from the electron energy distribution function (EEDF) describing the probability function for a free electron to have a specific energy. The EEDF is normalized and in molecular gases at atmospheric pressure is often described by the Maxwellian function [35], a few examples are shown in figure 2.1.

Plasma exists in many different ranges of pressures, n_e, and T_e (some examples are shown in figure 2.2) and can be characterized by several parameters. An important distinction commonly referred to in literature, is between cold or **non-thermal plasmas**, where T_e is much higher than the temperature of the heavier neutral or ionized species (T_n and T_i respectively), and hot or **thermal plasmas** where T_e, T_n and T_i are in equilibrium. Cold and hot plasmas are characterized by different ionization degrees α, which describes how many particles of the plasma are ionized and is defined as:

$$\alpha = \frac{n_i}{n_i + n_n}, \tag{2.3}$$

where n_i is the ion density and n_n is the neutral density. Following this definition, $\alpha \approx 1$ corresponds to fully ionized plasmas (which in general are hot plasmas) and $\alpha \ll 1$ to weakly ionized plasmas (cold plasmas). Hot plasmas are usually seen in stars, tokamaks, or, more generally,

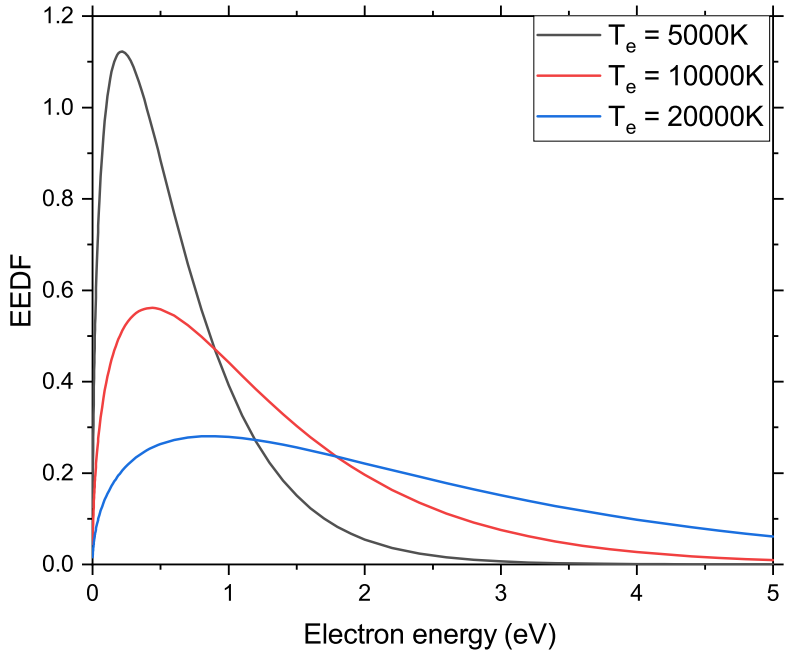

Figure 2.1: Example of the EEDF described by three different T_e.

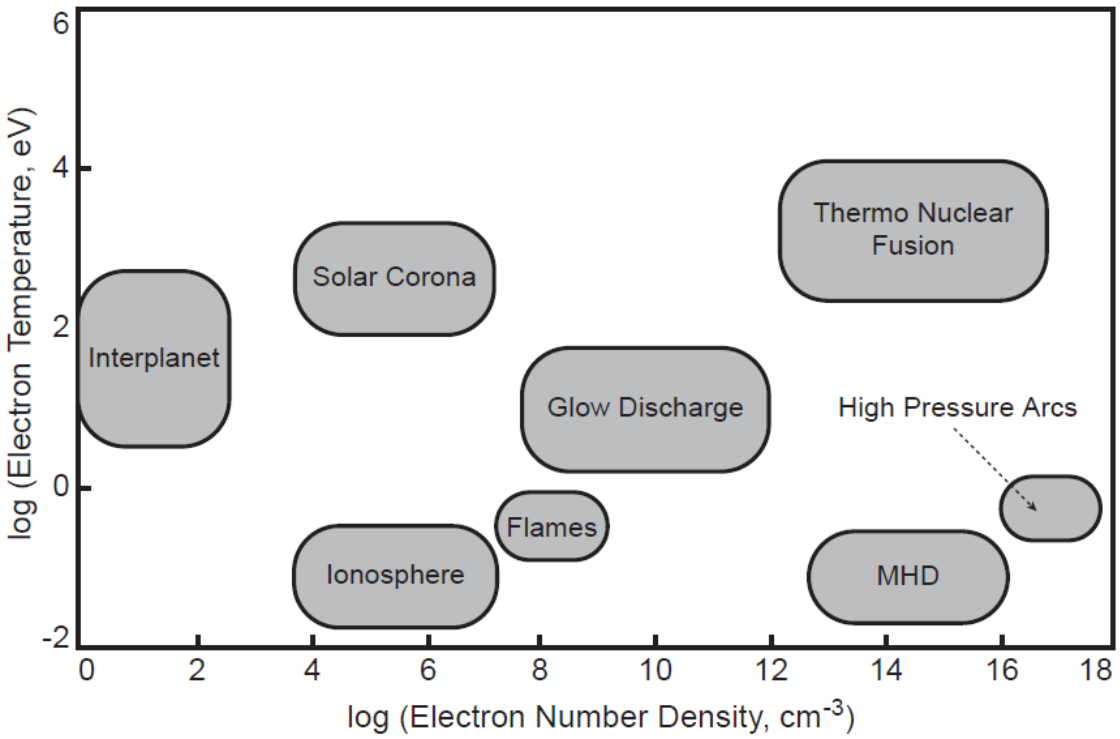

Figure 2.2: Plasma classification based on electron temperature and density. Reprinted from [35].

when nuclear fusion is involved, while cold plasmas are generally used for lower-temperature applications such as gas conversion, film deposition, or surface sterilization.

2.2 Molecular theory

Understanding the structure of a diatomic molecule as N_2, O_2, or NO is crucial for the interpretation of the measurements. Additionally, as it will be further discussed in later sections, in the context of plasma NF the energy transfer between different excitation modes is an important phenomenon to control in order to optimize the conversion efficiency [21]. In general, the type of excitation of a species depends on its degrees of freedom. For diatomic molecules, three main excitation modes can be distinguished: electronic, vibrational, and rotational [37, 38]. These excitations exist in discrete energy levels, following the rules of quantum mechanics.

2.2.1 Electronic states

A collision between a high energy free electron and a neutral molecule, or atom, can cause an energy transfer to an electron bound to the molecule. The mechanism is represented as $e + X \rightarrow e + X^*$, where the species X receives energy from an electron and reaches the higher electronically excited state X^*. The energy of the electronically excited particles is generally high, ranging from approximately 5 to 10 eV, and, thus, generally involves the electrons corresponding to the tail of the EEDF. This energy transfer causes a change in the quantum numbers of the electrons of a molecule. Therefore, the naming of the electronic states for diatomic molecules follows a labeling that depends on the quantum numbers characterizing the state and can be generalized as [37, 39]:

$$^{2S+1}\Lambda^{+,-}_{g,u}, \tag{2.4}$$

where S is the spin quantum number of the molecule (and $2S + 1$ its multiplicity), Λ the projection of the molecule angular momentum on the inter-nuclear axis ($\Sigma = 0$, $\Pi = 1$, $\Delta = 2$, ...) and, finally $+, -$ and g, u describe the symmetry of the electronic wave function [39]. This labeling is usually accompanied by a Latin letter defining the energy of the electronic level: the electronic ground state is labeled by the letter X and electronically excited states are ordered by increasing energy and named with a letter A, B, C, ...

2.2.2 Vibrational states

The energy can also be transferred to an excitation of the vibrational state of a molecule. Considering a diatomic molecule, the vibrational excitation describes the oscillation in the internuclear distance between the two atoms of a molecule. The oscillation is possible in discrete modes and it can be described by the vibrational quantum number ν.

The energy difference between different vibrational levels is milder and is usually in the order of magnitude of 0.1 eV. D_0 is the dissociation energy, which describes the vibrational energy

threshold for the molecule to dissociate. The importance of the vibrational excitation is crucial as, in the context of this thesis and as it will be discussed in section 2.3, a high vibrational excitation can greatly enhance the formation of NO.

By considering an ensemble of molecules in a plasma, each will be characterized by its vibrational excitation level. If the distribution of molecules in different vibrational states can be assumed to follow a Maxwell-Boltzmann distribution, a vibrational temperature (T_{vib}) can be defined.

$$n_\nu \propto \exp\left(-\frac{E_\nu}{k_b T_{vib}}\right), \tag{2.5}$$

where E_ν is the energy associated to the vibrational level ν.

2.2.3 Rotational states

An additional degree of freedom of a diatomic molecule is the rotation around its center of mass. As discussed for the vibrational excitation, the rotational excitation is only possible in discrete modes which are described by the rotational quantum number J. The energy difference between two rotational levels is smaller than between two vibrational levels and a rotational temperature can also be defined as:

$$n_J \propto \exp\left(-\frac{E_J}{k_b T_{rot}}\right), \tag{2.6}$$

where E_J is the energy associated with the rotational level J. It should be noted that the rotational energy distribution may differ between electronically excited molecules and ground-state molecules. The lifetime of a molecule in electronic ground state is in most cases long enough for the rotational distribution to thermalize, through collisions between heavy particles, and reach the Boltzmann equilibrium. On the other hand, the lifetime of an electronically excited molecule is often shorter and this assumption should be verified before assuming a Maxwell-Boltzmann distribution, especially for low-pressure plasmas [40].

Figure 2.3 shows a scheme of the potential energy of a diatomic molecule, summarizing the main excitational states, as a function of the internuclear distance.

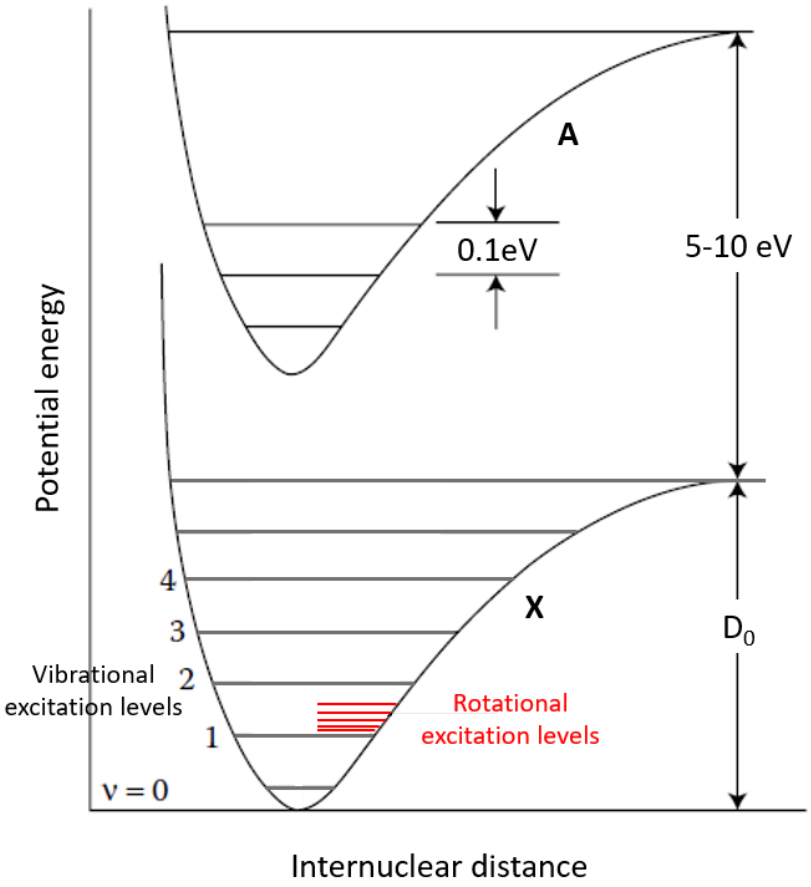

Figure 2.3: Typical potential energy of a diatomic molecule as a function of the internuclear distance. Adapted from [37].

2.2.4 Energy transfer mechanisms

Energy is mainly transferred between the species population and the plasma through collisions. The collisions are defined as "elastic" if the total kinetic energy remains unchanged. More interesting are "inelastic" collisions, where part of the kinetic energy is transferred to the molecules changing their excitation level [35]. As already highlighted, electron impact collisions contribute significantly to the energy transfer towards each excitation mode (electronic, vibrational, or rotational) of a molecule according to the energy of the electron involved in the collision. However, besides direct electron impact excitation, as a result of collisions between heavy species, the molecules in a plasma are affected by energy transfer mechanisms which are crucial for the plasma chemistry.

Particularly relevant for this thesis is the formation of molecules with a high vibrational excitation level which, at elevated pressures, are populated by collisional energy exchange between molecules, called VV relaxation, rather than by direct electron impact. The most conventional resonant energy transfer due to VV relaxation usually implies a transfer of vibrational energy between two molecules of the same species [35], as for example,

$$N_2(\nu = 1) + N_2(\nu = 2) \rightarrow N_2(\nu = 2) + N_2(\nu = 1). \tag{2.7}$$

Similarly, the VT relaxation describes the transfer of energy between vibrational excitation modes and the translational energy of the molecule, whose distribution is effectively described by the gas temperature T_{gas}, and the RT relaxation describes the transfer of energy between rotational excitation modes and the translational energy of the molecule.

For these processes, a characteristic time can be defined to describe the time required to reach equilibrium between these excitation modes. If, for example, the characteristic time for VT relaxation is high, the molecules on average, maintain their vibrational excitations for longer, which, as discussed in section 2.3 is beneficial for N_2 dissociation.

2.3 Zeldovich mechanism

Due to the strong triple bond present in the N_2 molecule (9.756 eV bond dissociation energy [1]), NF into NO is a highly endothermic process and is characterized by an enthalpy of $\Delta H = 90\,\mathrm{kJ/mol}$ [10]. In a N_2-O_2 plasma, the first step towards the formation of NO is the dissociation, through electron collision, of O_2 which can happen in more stages, depending on the energy of the impacting electron.

$$e^- + O_2(\nu = 0) \rightarrow e^- + O_2(\nu > 0) \rightarrow e^- + O + O \tag{2.8}$$

The main net contributor to the NO_x formation is the Zeldovich mechanism, which consists of breaking the triple bond of N_2, either in the ground state or vibrationally excited, with an O atom.

$$N_2(g, \nu) + O \leftrightarrow NO + N \tag{2.9}$$

While the reaction from $N_2(\nu)$ is more efficient, because part of the energy barrier is already provided by the excitation energy, it should be noted that the Zeldovich reaction can occur from both N_2(g) and $N_2(\nu)$. In the first case, it is defined as the thermal Zeldovich mechanism, while in the second case, it is called the "vibrationally-enhanced Zeldovich mechanism" [41]. The N atom is further involved in a reaction with O_2 in either ground state or vibrationally excited.

$$O_2(g, \nu) + N \leftrightarrow NO + O \tag{2.10}$$

NO_2 is then mainly formed in either the discharge region as the NO reacts with the O atoms

$$NO + O \leftrightarrow NO_2, \tag{2.11}$$

or, as the gas cools down, in the post-discharge region through NO oxidation

$$2NO + O_2 \leftrightarrow 2NO_2, \qquad \Delta H = -114\ \text{kJ/mol}. \tag{2.12}$$

2.4 Non-thermal plasma processes

In the context of gas conversion, the free electrons in the plasma are used to selectively excite and activate the gas molecules, allowing them to quickly react and undergo thermodynamically unfavorable or energy-intensive chemical reactions. Gas conversion usually involves non-thermal plasmas in which, expanding the definition provided at the end of section 2.1, the temperature of the free electrons (T_e) is much higher than the characteristic temperatures of the molecules $T_e > T_{vib} > T_{rot}$. Thermal plasmas can also be used for gas conversion but are typically less energy-efficient [21, 35].

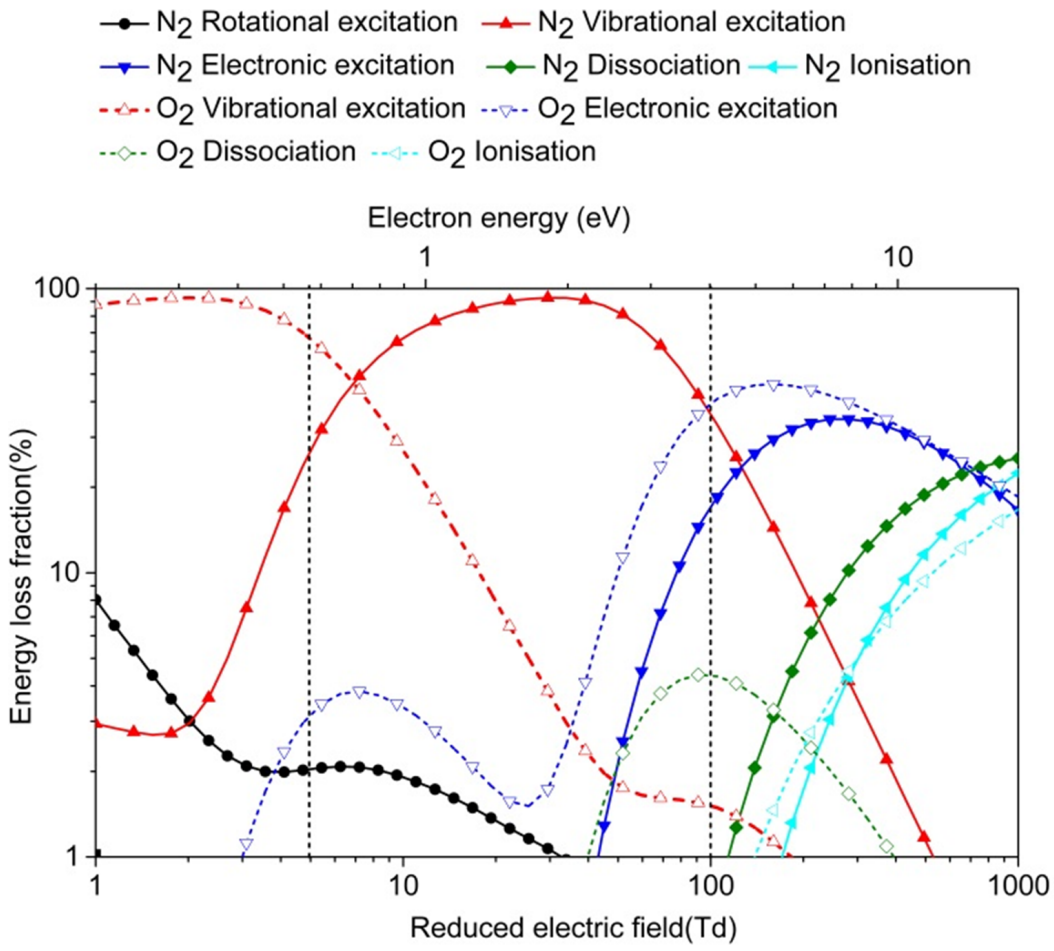

Figure 2.4: Fraction of energy transferred from free electrons to different channels of excitation, dissociation, and ionization of N_2 and O_2 as a function of E/N and of the electron energy, from [42].

Recent articles based on modeling have highlighted the reduced electric field (E/N) as an important parameter to understand how the energy of the free electrons is transferred to the neutral species in the plasma [21, 42]. Figure 2.4 shows how free electrons transfer their energies as a function of E/N in a N_2-O_2 plasma specifically. These results highlight that, in order to enhance the N_2 conversion through the vibrationally-enhanced Zeldovic mechanism, plasmas characterized by an E/N between 5 and 100 Td should be preferred, such as gliding arc plasmatrons (GAP) and microwave (MW) discharges. Higher E/N would be characterized by an energy transfer towards less efficient channels for NF, such as electron excitation or electron impact molecular dissociation.

It should be noted, however, that an optimal E/N is not a sufficient condition to guarantee for the Zeldovic mechanism to be favored. Despite being among the most promising plasma types, GAPs and MWs operating at atmospheric pressure are characterized by a high T_{gas}, approaching a more thermal regime, and VT relaxations can quickly depopulate the vibrational levels.

2.5 Types of plasma

As it is important to discuss the way the energy is channeled, since it strongly affects the process efficiency, it is also crucial to distinguish between the different types of plasma to understand which best suits the desired process.

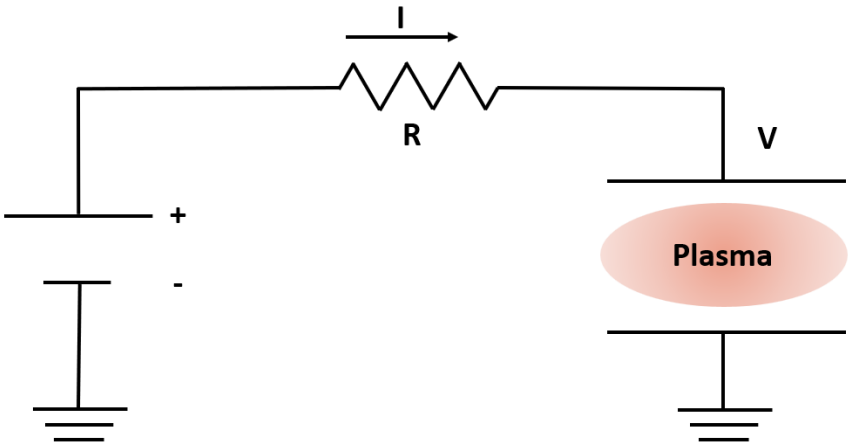

Figure 2.5: Simplified schematics of a DC discharge setup.

Figure 2.5 shows a simplified scheme of a DC discharge. A DC power supply is connected to an electrode through a resistance R. Depending on the voltage and current provided to the setup different regimes can be observed which are schematized in figure 2.6:

- The **dark discharge regime**. At the initial state, when no voltage difference is applied between the two electrodes, the gas cannot be considered ionized as the only few free charges present in the gas are caused by the background radiation. As the voltage is increased, more of these ionized free charges are collected by the electrodes (A-B in figure 2.6), until a saturation regime is reached where all the charged particles are collected (B-C). The voltage

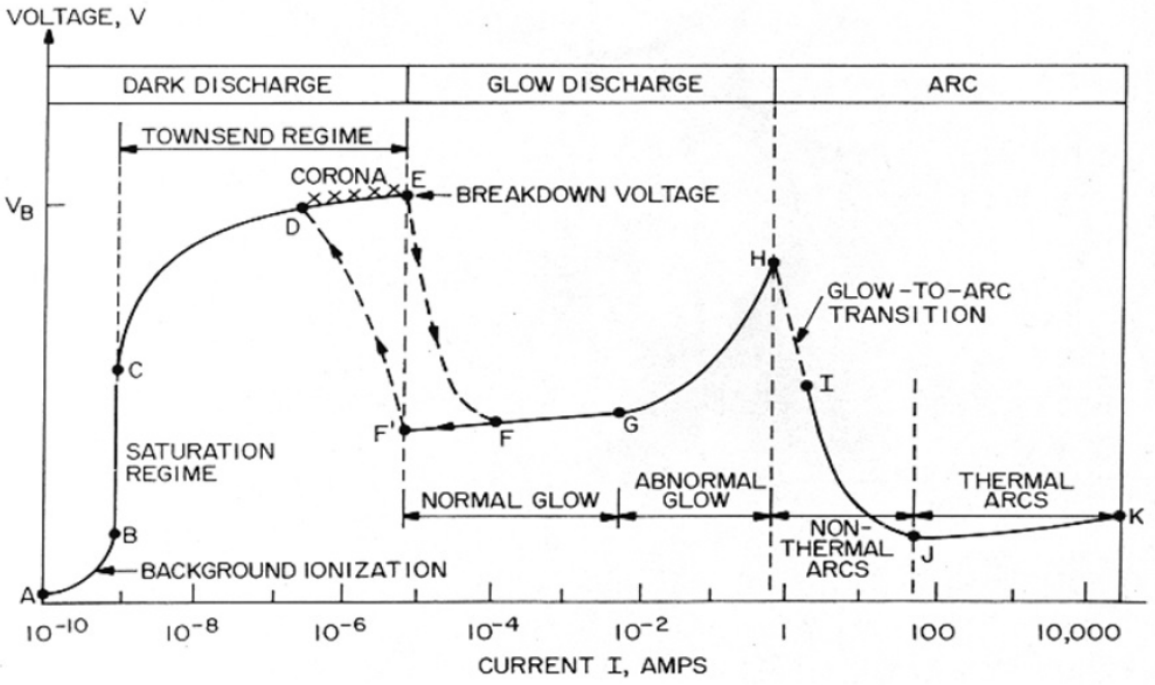

Figure 2.6: General current-voltage characteristics of DC discharges. The values for the current vary according to different parameters such as the pressure, the gas composition of the plasma, or the electrode geometry. Reprinted from [43].

difference eventually becomes sufficient for a free electron to gain enough energy to ionize a neutral particle in the gas upon collision, causing a secondary electron to detach and a positive ion to form. Both of the electrons can then drift towards the anode, eventually colliding and ionizing more molecules (C-D). This avalanche ionization process is known as the **Townsend regime** and the ratio between the secondary electron flux and the flux of free charges collected at the anode can be described by the Townsend coefficient γ. As the voltage applied increases, the positive ions collide with the cathode with growing energy, freeing additional electrons. Eventually, the amount of electrons emitted due to collisions with the cathode becomes dominant compared to the primary electrons detached due to the background ionization. This phenomenon is defined as the **gas breakdown**. The breakdown can be local if the electric field is not uniform and it is known as a **corona discharge** (D-E) which is typical if spikes or inhomogeneities are present on the cathode. Or it can be global causing the gas to become conductive and lower its electrical resistance, causing a drop in the voltage (E-F).

- The **glow discharge**. As the gas breakdown is obtained, the discharge becomes visible (thus, its name) due to photon emissions from the excited molecules in the plasma. The main characteristic of the **normal glow** (F-G) is that the current density remains constant. As the total current increases, more surface of the cathode is covered by the discharge with little effect on the voltage between the electrodes. When no more free surface is left on the cathode further current growth requires a higher current density causing the voltage to

steeply increase in what is defined as the **abnormal glow** discharge (G-H).

- The **arc discharge**. As the current density increases the energy of the ions colliding with the cathode grows accordingly. The cathode is consequently heated increasing the number of electrons released due to thermionic and field emissions. The contribution of these two effects can quickly become dominant over the electron emission due to the ions colliding with the cathode. Thus, due to the high amount of electron emission, the discharge current can be sustained without a further avalanche ionization in the plasma. This results in the discharge stabilizing at a lower voltage (H-I). Two regions can be identified according to the voltage behavior as a function of the discharge intensity.
  - For **non-thermal arcs**, the main electron emission process is the thermionic emission, which is favored as the cathode temperature increases due to higher currents [37]. This results in a net decrease of the voltage as more current is applied. As a physical system naturally evolves toward configuration with lower potential energy, a non-thermal arc is unstable as the current tends to increase indefinitely if not limited. For this reason, as shown in the scheme in figure 2.5, it is necessary to introduce a passive component, as a resistance, to limit the arc current.
  - For **thermal arcs** field emission generally becomes the dominant electron emission process due to the progressive erosion of the cathode and the consequent formation of spikes where the emission of electrons is concentrated [37]. This region is characterized by a weak increase in the voltage as a function of the arc current. If the material of the cathode can withstand high temperatures, thermal arcs can also be sustained by thermionic emission [37].

Typically, the arc regime can directly follow the gas dielectric breakdown if the voltage provided is still sufficient to cause the transition from glow to arc.

More generally, the voltage at which the gas dielectric breakdown occurs is defined as the breakdown voltage (V_B) which is described by the Paschen law [44]

$$V_b = \frac{Cpd}{\log\left(\frac{Apd}{\log(1+\gamma^{-1})}\right)}, \tag{2.13}$$

where C and A are two constants that depend on the gas composition, and γ, previously defined as a Townsend coefficient, depends on the electrode material. It should be noted that the V_B is a function of the product of both the gas pressure and the distance between the electrodes (pd). The Paschen curve for various gases is shown in figure 2.7. As an example, considering air at atmospheric pressure (760 Torr) and an electrode distance of 1 mm, V_B is approximately 3 kV. It should be noted that the Paschen curve has a minimum. For relatively low pd, the possibility of having an electron collision ionization is low, thus, as pd decreases, a higher voltage is needed to generate enough secondary electrons to self-sustain the discharge. On the other hand, for relatively

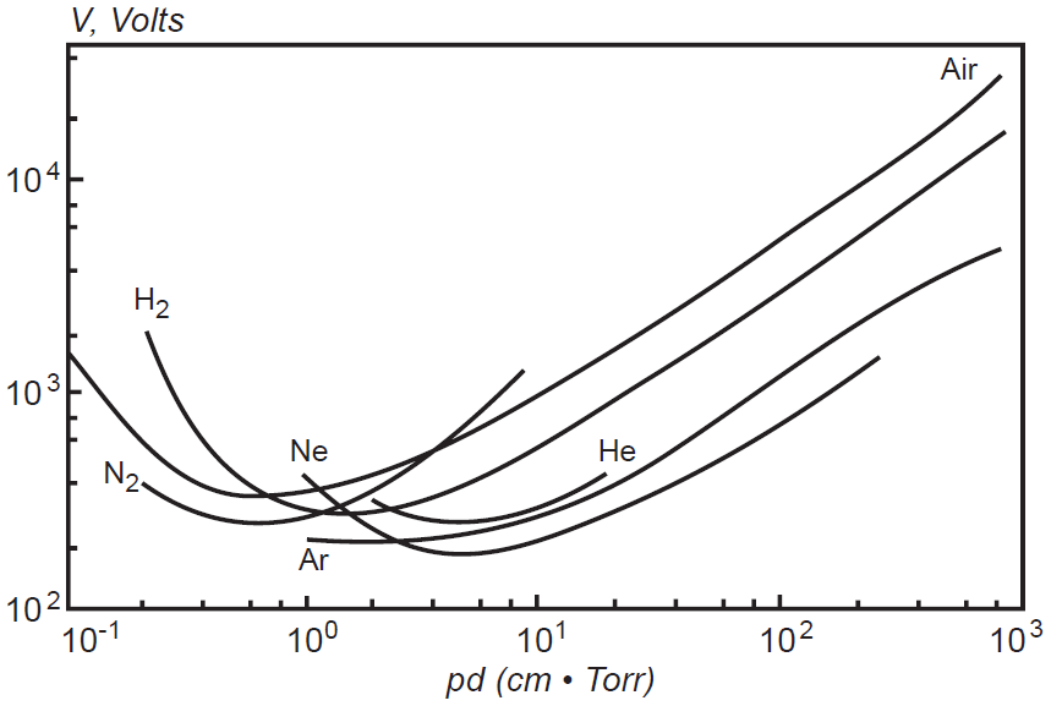

Figure 2.7: Breakdown voltage (V_B) for various gases as a function of the product between the gas pressure and the distance between the electrodes (pd). Reprinted from [35].

large pd, ion-molecule collisions increase in frequency, causing the ions to lose energy. A higher V_B is thus needed for the ions to hit the electrode with enough energy to cause the emission of secondary electrons, causing V_B to increase almost linearly to pd [44].

2.5.1 Gliding arc plasmatron

A classic gliding arc (GA) discharge consists of two diverging electrodes among which a gas flow is injected as shown in figure 2.8(a). A high voltage difference is applied between the two electrodes until the breakdown voltage is reached, initiating an arc at the shortest distance between the electrodes where the electric field is the strongest. The arc is then dragged by the gas along the direction of the flux. Moving upstream, the elongation of the arc increases together with the voltage difference required to sustain the arc. Once the power supply is not able to sustain it, the arc extinguishes and the process restarts with a new arc forming at the shortest distance between the electrodes. Depending on the operating conditions, such as the total flux, the input gas composition, and the power provided, the plasma generated by a GA can have the properties of either a thermal or a non-thermal arc. It is also possible for the arc to transition from a thermal regime where the arc discharge is formed and the current is at its highest to a non-thermal regime as the arc elongates [37, 45].

More recently, the design of GA discharges evolved towards a three-dimensional implementation called gliding arc plasmatron (GAP) as proposed by Nunnally et al. [46]. In the GAP the cathode and the anode are hollow cylinders with one and two apertures respectively as shown

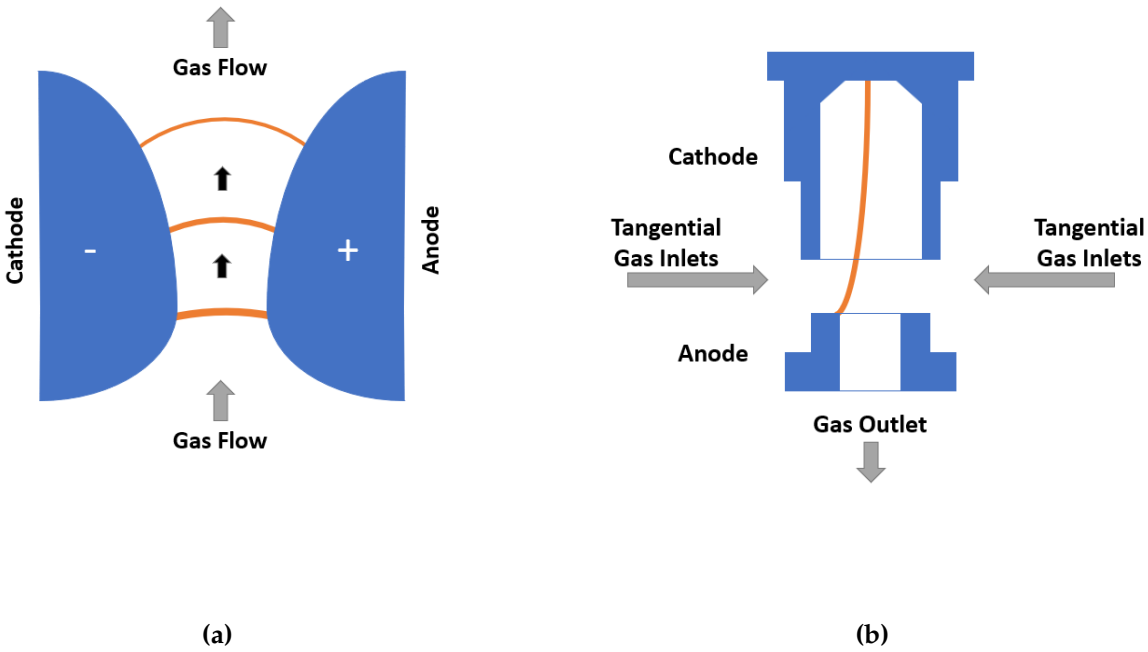

Figure 2.8: Basic schematics of a classical gliding arc (a) and a gliding arc plasmatron (b)

in figure 2.8(b). The gas is injected tangentially between the electrodes through a swirl generator, which can be schematized as in figure 2.9, initiating a vortex-shaped flow along the walls. A photo of the system showing the anode is illustrated in figure 2.10.

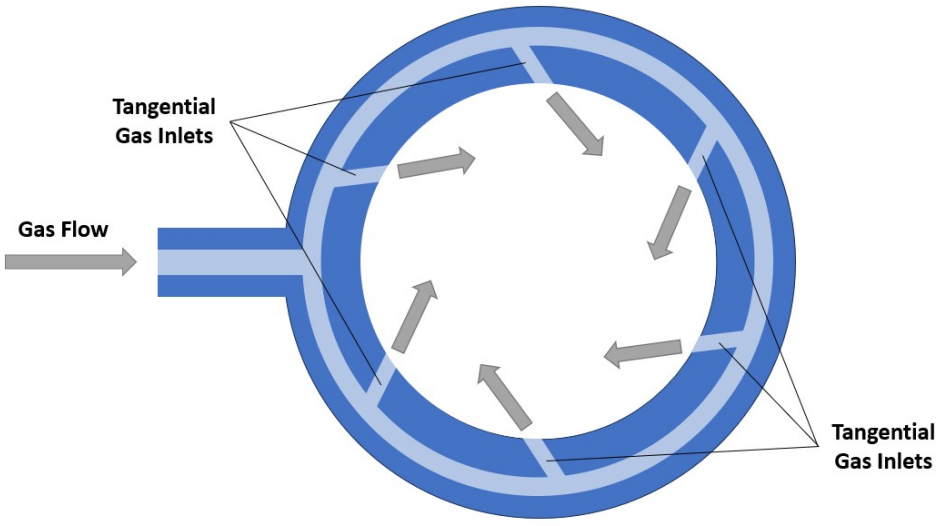

Figure 2.9: Horizontal section of the swirl generator indicating the tangential inlets of the GAP. The gas is directly injected between the electrodes.

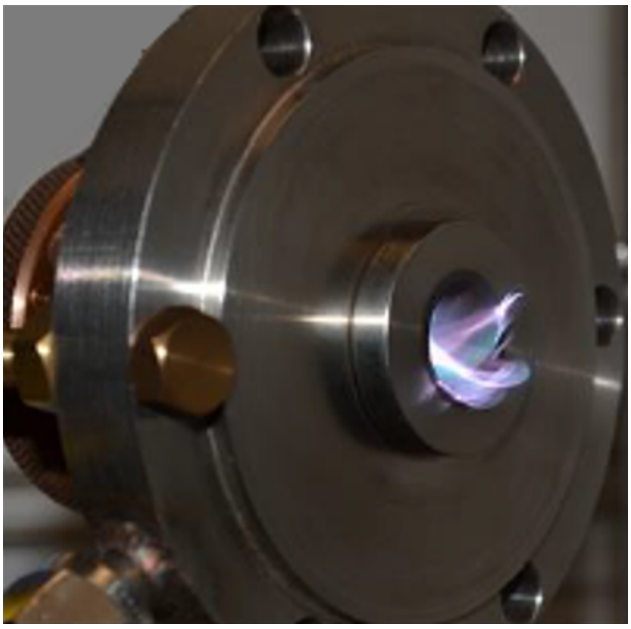

Figure 2.10: Photo of a GAP anode. Adapted from [47].

Similarly to what was discussed for the GA, once the breakdown voltage is reached, the arc ignites between the shortest gap among the electrodes and is then pushed by the gas flow towards the center as indicated in figure 2.8(b). One of the ends of the arc then anchors at the center of the cathode as the other rotates along the anode dragged by the vortex flow [47]. The flow can cause the extension of the arc which, according to the operating conditions, can extend inside the anode and well after it. As the arc overextends and rotates, the voltage difference between a section of the arc and the anode can be enough to break the dielectric between them and abruptly shorten the arc. According to the inner diameter of both the cathode and the anode, the flux can evolve in two different regimes [47, 48].

- If the inner diameter of the anode is larger: the gas flow along the walls is directly ejected in what is known as the forward vortex flow.
- If the inner diameter of the anode is smaller: the gas initially flows backward along the cathode walls and, once its closed end is reached, a secondary vortex forms at the center of the cathode which flows towards the gas outlet. This regime is known as the reverse vortex flow.

The RVF regime provides better heat insulation and arc confinement and, therefore, is generally preferable.

Another more recent and widely used three-dimensional evolution of the GA design is the rotating gliding arc (RGA). The main difference with a GAP is the shape of the electrodes, shown in figure 2.11, where the cone-shaped cathode is placed in a hollow anode.

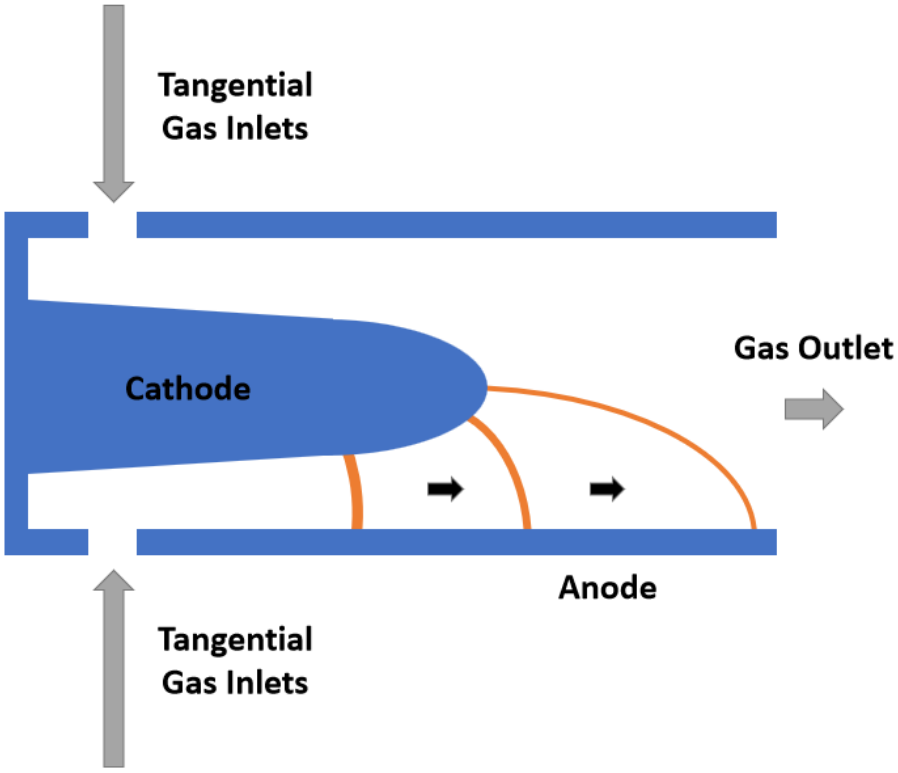

Figure 2.11: Basic schematics of a rotating gliding arc.

2.5.2 Microwave plasma

A microwave (MW) plasma is generated by heating the free electrons through a microwave electromagnetic field (i.e. with a frequency between 300 MHz and 10 GHz) which will transfer their energy to the neutral particles in the gas by collision. Through electron impact ionization and excitation, the plasma can ignite and be sustained. Since MW plasmas do not use electrodes and are AC discharges, they differ from the cases discussed in section 2.5. However, the typical characteristics of a glow discharge can be identified in a MW plasma, such as the formation of a plasma column whose size is inversely proportional to the gas pressure [49].

Among the different variations of MW plasmas, surface wave discharges are the most popular option for plasma gas conversion. The typical design of a surface wave discharge, briefly schematized in figure 2.12(a), consists of a quartz tube, which is transparent to MW radiation and confines the gas flow, intersecting with a waveguide used to provide the MW radiation necessary to initiate the discharge. The radiation then propagates on the plasma column where its energy is absorbed, effectively sustaining the plasma. Often, a second quartz tube is present as in figure 2.12(a) to introduce a flow of cooling oil to control the gas temperature in the discharge. MW plasmas can operate in a wide range of pressures, from a few tens of mTorr up to atmospheric pressure. However, it must be noted that, as the pressure increases and the higher collisionality favors energy transfer to rotational modes, MW plasmas approach thermal equilibrium with consequent loss in terms of energy efficiency [21].

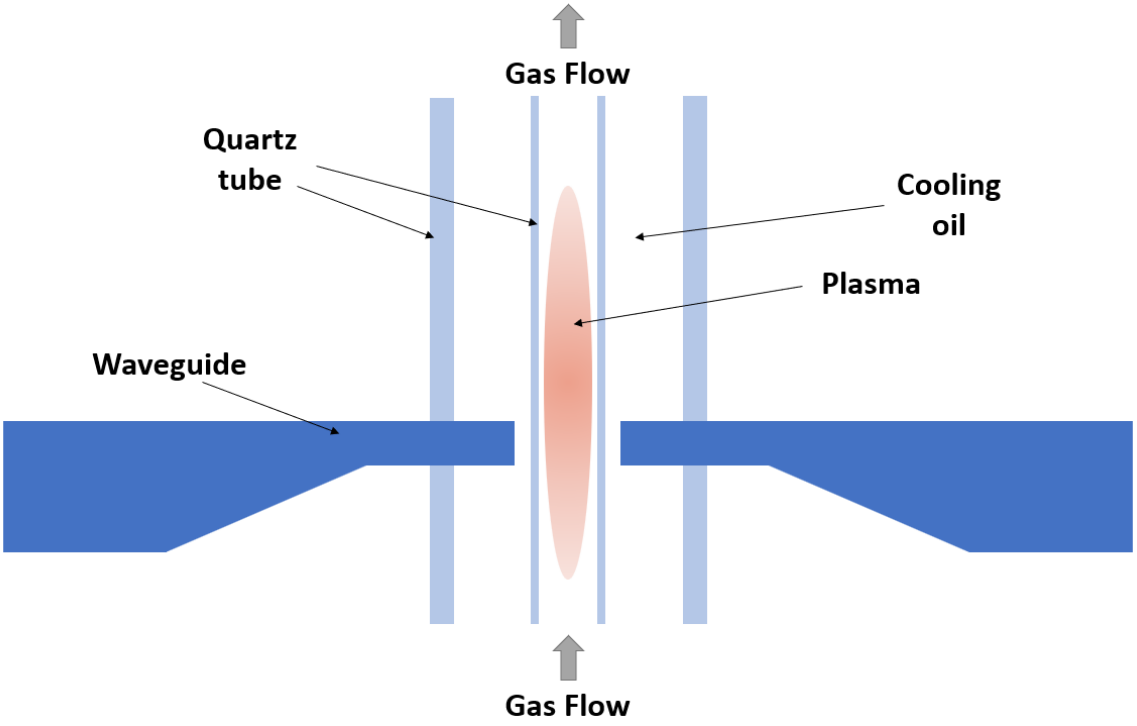

(a)

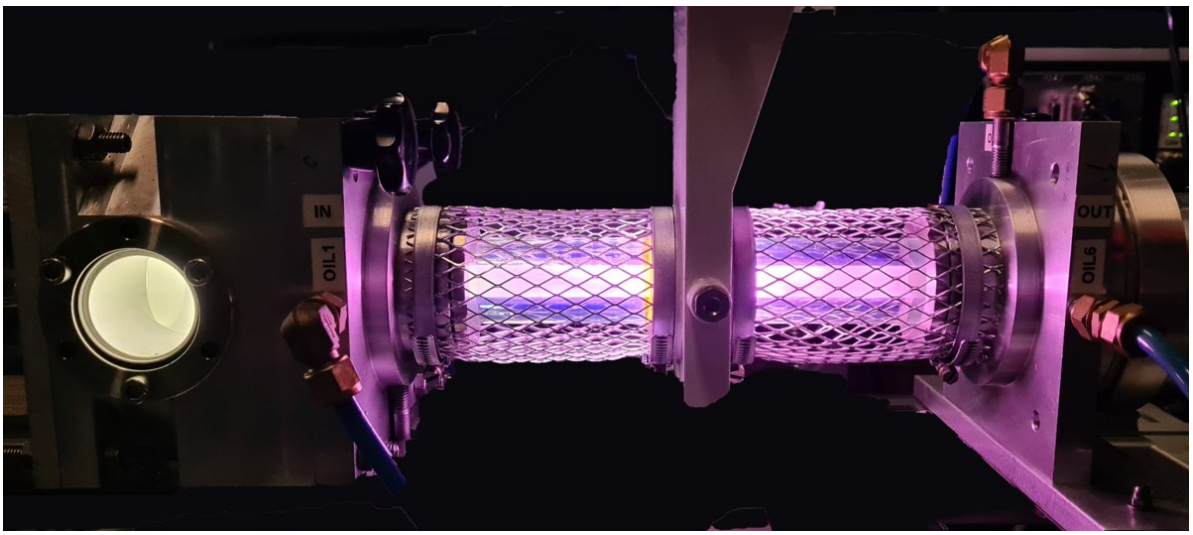

(b)

Figure 2.12: Basic schematics of a surface wave microwave discharge (a) and a photo of a MW discharge, courtesy of Omid Samadi Bahnamiri (b).

2.6 State-of-the-art of plasma nitrogen fixation

Plasma-based NF has, thus far, achieved the most promising results in the NO_x synthesis because of the lower energy costs compared to NH_3 synthesis and of the possibility of using air as the feed gas [21]. The main results discussed in this section are summarized in table 2.1. As previously mentioned, GAPs (and their RGA variants) and MW discharges are among the most efficient reactors for plasma NF.

2.6.1 Performance

Table 2.1: Summary of the NO_x yield and energy cost from different plasma sources. The results obtained using an air-like (80% N_2 - 20% O_2) feed gas instead of oxygen-enriched air (50% N_2 - 50% O_2) are marked (*). Adapted from [19, 21, 50].

Plasma type	NO_x yield (%)	Energy cost (MJ/mol N)	Reference
GAP & RGA			
GAP *	1.5	3.6	[41]
GAP	2.9	2.8	This work
RGA	3.4	2.4	[51]
RGA with effusion nozzle	5.9	2.1	[52]
High pressure RGA	4.9	1.8	[53]
MW			
Pulsed MW discharge	7	8	[54]
MW discharge	3.8	2	[55]
MW discharge with MoO3 catalyst	6	0.84	[56]
MW discharge with magnetic field	14	0.29	[57]
DBD	0.6	56-140	[58]
Packed DBD (γ-Al_2O_3)	0.5	18	[59]
Pin-to-plane DC glow discharge	-	7	[58]
Propeller arc discharge	0.4	3.5	[58]
Pin-to-pin DC glow discharge	0.7	2.8	[60]
Pulsed plasma jet	0.02	0.42	[61]

Using the GAP design Vervloessem et al. [41] report an energy cost of 3.6 MJ/mol N and a NO_x yield of 1.5 % using an air-like feed gas ratio. One of the main limitations of this result, which is a common flaw of the currently used GAP design, is the limited fraction of gas that passes through the arc. Indeed, the authors estimate, through fluid dynamics simulations that only 15% of the gas interacts with the arc. If the feed gas was to entirely pass through the arc, the energy cost and NO_x yield figures would be expected to improve to 0.5 MJ/mol N and 8.2 %, respectively. It should also be noted that the composition of the feed gas mixture plays an important role in the reactor's performance. The energy cost and NO_x yield reach their minimum and maximum, respectively, with, approximately a 50-50 N_2-O_2 gas composition. Slightly better results have been obtained with an RGA by Jardali et al. [51] who report an energy cost of 2.4 MJ/mol N and a NO_x yield of 2.4 %. This work is particularly significant as it highlights the effect of the RGA/GAP

operating regime on the overall reactor performance since the best results have been obtained when the hot plasma region covered a larger portion of the reactor body. These results have been further improved with the introduction of an effusion nozzle by Van Alphen et al. [52], improving the energy cost to 2.1 MJ/mol N and the yield to 5.9 %. This notable performance improvement is attributed to the effusion nozzle acting as an efficient heat sink close to the plasma. This causes a faster quenching of the gas and the consequent inhibition of NO_x recombination in N_2 and O_2 through the Zeldovich back reaction. Recently, the best result of 1.8 MJ/mol N with an RGA has been achieved by Tsonev et al. [53] operating at 4 bar. This study shows how an increase in pressure, an often overlooked parameter, can improve the NO equilibrium concentration.

As for MW discharges, the best results in terms of both energy cost and NO_x yields were reported in 1980. Asisov et al. [57] studied a MW plasma at low pressure with a magnetic field reporting an energy cost and NO yield of 0.29 MJ/mol N and 14 %, respectively. Similar results were obtained four years later by Mutel et al. [56] with the introduction of a MoO_3 catalyst, who reported an energy cost of 0.84 MJ/mol N and NO yield of 6 % However, caution should be applied when comparing these results with the rest of the literature as these results have not been reproduced in recent years. Additionally, in both cases the reactors were cooled with a constant flow of liquid nitrogen, the cost of which is not included in the energy costs reported. Notable recent results have been obtained by Samadi et al. [54] reporting a high NO yield of 7 % with an energy cost of 8 MJ/mol N using a pulsed MW plasma in a low-pressure range of (0.5 - 15) Torr. This study highlights the role of the pulse repetition rate in enhancing the vibrational excitation of the N_2. More success was obtained by Kelly et al. [55] with a MW operating at atmospheric pressure. Similar to what is done with GAPs and RGAs, in the study the gas was introduced in a vortex flow. An energy cost of 2.0 MJ/mol N and a NO_x yield of 3.8 % are reported.

Other designs have also been implemented and tested for non-thermal plasma NF. Most notably the performance of a pin-to-pin DC glow discharge was reported to be a NO_x yield of 0.7 % and an energy cost of 56 MJ/mol N [60]. DBDs proved to be inefficient in terms of energy efficiency, with the current best results of 0.5 % of NO_x at a cost of 56 MJ/mol N. The energy cost was lowered to 18 MJ/mol N with the introduction of an γ-Al_2O_3 catalyst [59]. More recently an energy efficiency below the 0.42 MJ/mol N, lower than the current energy cost of the H-B process, was obtained with a pulsed plasma jet [61], although with a low NO_x yield of 0.02 % that would be an obstacle to the upscaling of the technology.

Direct plasma-based conversion from N_2 and H_2 to NH_3 is generally reported to be more energy demanding as most of the results in the literature report an energy cost of the order of 10 MJ/mol N or higher and typically requires the presence of a catalyst [62], with only two studies reporting a lower energy consumption by Kim et al. [63] and by Peng et al [64]. The current best result was obtained by Kim et al. [63] using a pulsed plasma between two concentric cylindrical electrodes, painted with silver paste, with a Ru(2)-Mg(5)/γAl_2O_3 catalyst, reporting an energy cost of 1.7 MJ/mol N. Using a similar reactor design Peng et al. [64] report an energy cost of 2.9 MJ/mol N using a $MgCl_2$ catalyst. These results, however, cannot be directly compared with

the H-B process as the energy cost associated with the H_2 synthesis is not included. Another interesting result was achieved by Hollevoet et al. [65, 66] by performing plasma NF to NO, which was then captured by a $Pt/BaO/Al_2O_3$ catalytic trap. The trap was then fed with a mixture of 5 % H_2 in N_2 causing the catalyst to release NH_3 (more details in section 6.3). Taking into account the energy needed for H_2 production and NH_3 separation the reported energy cost is 4.6 MJ/mol N [65] when combined with a RGA [51], and 2.9 MJ/mol N [66] when combined with a pulsed plasma jet [61]. This result is particularly relevant as it shows a similar energy cost compared to the direct conversion of N_2 and H_2 to NH_3.

2.6.2 Diagnostics and plasma characterization

Laser-induced fluorescence (LIF, explained in section 3.3) is a widely used optical diagnostic tool, often used for the determination of the absolute density of the species in the plasma [67, 68]. Gromov et al. [69, 70] used LIF to directly measure the density of NO(X) by exciting the $J = 4.5$, $J = 13.5$, $J = 10.5$ rotational lines in a ns-pulsed discharge at atmospheric pressure. Van Gessel et al. [71] used LIF for the determination of NO(X) absolute density and T_{rot} in a microwave plasma jet. The temperature determination is performed by a wide scan in the wavelength range between, approximately, 226.3 and 226.9 nm with a high-repetition-rate UV laser system. At low pressure, Chatterjee, Samadi et al. [in preparation] studied the temporal evolution of both NO and O atoms for a MW system, highlighting the role of energy transfer between vibrational levels in the formation of NO. To the author's knowledge, no LIF-based studies exist on a gliding arc system used for NF.

Optical Emission Spectroscopy (OES) is widely used in literature for the study of the so-called N_2 second positive system, describing the spontaneous emission from the state $C^3\Pi_u$ to $B^3\Pi_g$, [39, 40, 72]. OES is typically used, together with software simulating emission spectra to determine T_{vib} and T_{rot}. In atmospheric arc discharges, OES is typically only used for air-like compositions (79 % N_2 - 21 % O_2), often fed with additional N_2. This is the case, for example, for Wu et al. [73] who used OES to characterize an air plasma, or by Zhao et al [74], who studies the spectra of a N_2 discharge in a GAP. As the fraction of O_2 increases, the use of OES is not reported to the author's knowledge.

The electrical characterization of arc discharges is not often tackled. In the past, different versions of bi-dimensional arc discharges have been studied, focusing on the thermal stability of the arc itself by Fridman et al, in 1999 [45]. The work reports that the power dissipated by the arc per unit of length plays an important role in defining the dynamics of the arc and its stability. More recently, Wu et al. [75] studied the electric characteristics of a RGA, identifying the relationship between the fluctuation of the voltage and current and the arc behavior.

2.6.3 Economic feasibility of the technology

A crucial topic, that is not often discussed in the literature, is the economics of plasma-based NF. As one of the main goals for the study of plasma-based NF is the implementation of the technology

at an industrial scale, feasibility studies are important. A great contribution on the topic is provided by Rouwenhorst et al. [19, 23] and by Anastasopoulou et al. [76, 77]. In the current scenario, plasma-based NF into NH_3 is not a viable alternative to the H-B process due to its prohibitively high energy cost [23]. Only in the best-case scenario of assuming the theoretical energy cost limit of 0.2 MJ/mol N, the plasma-based NH_3 production costs are expected to approach the production costs associated with the H-B process. The results are more encouraging if the combination of H-B and Ostwald processes for the production of NO_x is considered for the comparison with plasma-based NO_x production. In such case, as the plasma-based counterpart does not require H_2, it is estimated that an energy cost of 1.1-1.5 MJ/mol N would be necessary for an economically viable implementation of plasma-based NF (in an update to ref. [19]). Similarly, Anastasopoulou et al. identify plasma-based NO_x production as an interesting alternative [77]. With an in-depth description of the ecological advantages of the technology, they show how the operative expenses (OpEx) for plasma-based NF could reach the H-B-based ones, arguing how this would allow for the implementation of the technology as a green and local alternative. Finally, Sarafraz et al. [11] study a specific combination of plasma NF with plasma pyrolysis of the methane released from biomass, demonstrating its feasibility at small scales.

2.7 Thesis motivation, objective, and strategy

2.7.1 Motivation

As explained in detail in section 1.2.3, for over a century the H-B process dominated the landscape of industrial NF. Despite the H-B process energy efficiency, plasmas are currently studied as a promising candidate to be a green alternative due to several potential advantages, among which:

- a lower theoretical energy consumption for non-thermal plasmas, predicted to be 0.2 MJ/mol N [6]. This limit is lower than the current best energy consumption reported for the H-B process (0.49 MJ/mol N) and the theoretical limit of the H-B-based technology (0.35 MJ/mol N).
- The absence of direct CO_2 emissions and the compatibility of plasma-based NF technology with intermittent renewable energy sources would greatly reduce the environmental impact of NF.
- Unlike the H-B process, non-thermal plasma NF can be performed close to atmospheric pressure and at relatively low temperatures. This allows plasma-based NF to be implemented at a much smaller and local scale compared to the H-B process with a small impact due to the economy of scale [11]. This could prove to be beneficial in providing a local source of N-based fertilizers to regions that are disconnected from main fertilizer production centers and, thus, would suffer from high transport costs.

Plasma-based NF technology is, however, still in an "early stage" as the current best results have either an energy cost of, at least, one order of magnitude higher than the theoretical limit for non-thermal plasmas (the current best results approach a thermal regime, limiting the effectivity of

the Zeldovich mechanism) or a low NO_x yield, decreasing its industrial competitivity. Due to this, together with the drawbacks of the current NF system based on the H-B process, there is an urgent need for a wide scientific effort to further deepen the understanding of plasma-based NF and enhance the capabilities of the technology. Crucial are, therefore, the study of N_2-O_2 plasma kinetics through the implementation of experimental diagnostic techniques and the analysis of the potential of plasma-based NF for an industrial application, both performance-wise and economically.

2.7.2 Objective and strategy

This thesis is part of the excellence of science (EOS) project "NITROPLASM", which includes all the major Belgian groups in the field of plasma-based gas conversion and was funded by FNRS-FWO (Fonds National de la Recherche Scientifique - Fonds voor Wetenschappelijk Onderzoek). The goal of the project was to acquire an in-depth understanding of the N_2 fixation mechanisms in N_2-O_2 and N_2-CH_4 plasmas by combining experimental and numerical investigations of a wide range of gas and plasma-liquid discharges.

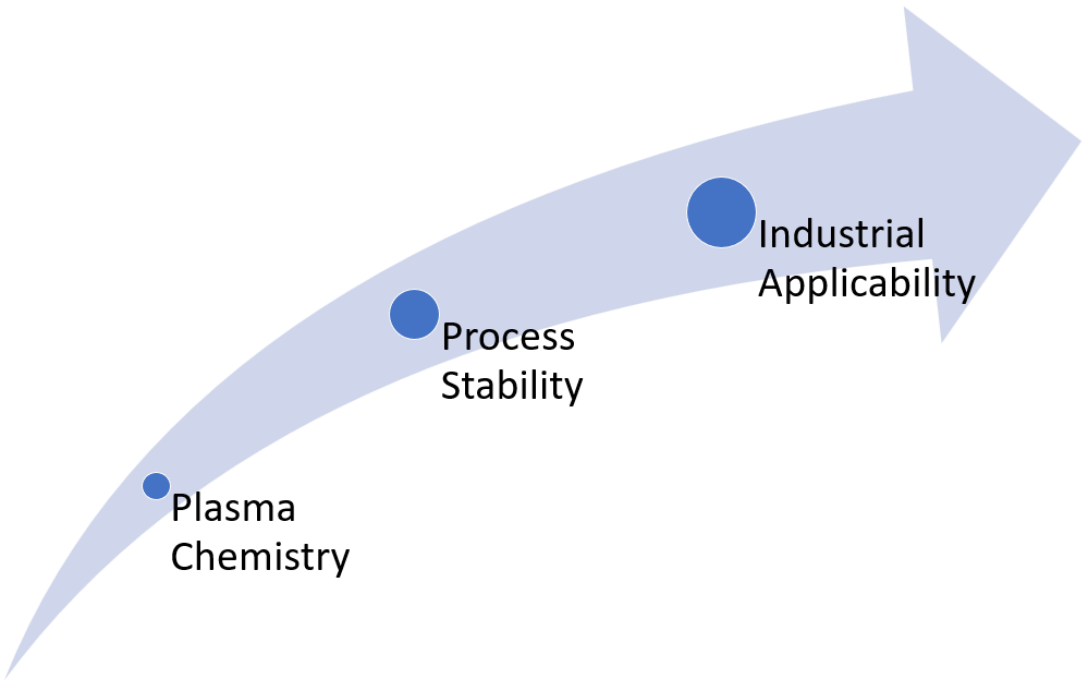

Figure 2.13: Illustration of the objectives of this thesis.

The objective of the thesis is to contribute to a better understanding of the NF process in a GAP operating at atmospheric pressure at different, complementary, levels, as visually schematized in figure 2.13.

At a fundamental level, the **plasma chemistry** is studied with the characterization of temperature and density distributions in the GAP afterglow. This is achieved with the use of advanced

optical diagnostic tools such as Fourier transform infrared spectroscopy (FTIR) and laser-induced fluorescence (LIF). Most notably, for the latter, a novel approach for LIF, developed by adapting existing methods to the study of atmospheric discharges with a high concentration of absorbers, proved to be necessary. In this context, OES is not used since in the emission spectra, in the presence of a high percentage of O_2 in the input gas (i.e. the 50 % N_2 - 50 % O_2 composition used during this thesis), a strong overlap between the O_2 Schumann-Runge bands and the N_2 second positive system was observed, effectively disallowing the extraction of information on the plasma temperatures as typically done in literature.

At a performance level, the study of the **process stability** and performance is crucial to understanding and improving the industrial applicability of plasma-based NF. This is done by investigating the effects (usually neglected in the literature) on key parameters such as its energy cost, and the NO_x yield of introducing external components in series with the GAP. Concerning this level, part of the strategy consists in developing and testing a better, less energy-consuming, alternative to stabilize a GAP.

And, finally, at an economic level, the **industrial applicability** of plasma-based NF is investigated by analyzing the requirements for an industrial application of plasma-based NF to be economically viable. A hypothetical application based on the current state-of-the-art is proposed and its production costs are compared with the currently dominant production chain based on the H-B process.

Chapter 3

Setup and Methodology

All the information concerning the experimental apparatus used for this thesis is discussed in this chapter. The crucial theoretical concepts for each diagnostic tool are described together with their implementation on the apparatus.

3.1 Experimental setup

A GAP operating at atmospheric pressure with a N_2-O_2 gas mixture was used for this thesis. The gas flow was regulated by two mass flow controllers (Aera FC-R7710CD). Figures 3.1(a) and 3.1(b) show the electric schematics and a picture of the reactor, respectively. The exhaust tube is grounded and electrically connected to the anode. The cathode of the reactor is connected to a DC power supply (Technix SR12KV-15KW) through a resistor R which can be set to assume resistance values between 1 kΩ and 19 kΩ. The power supply has a negative polarity, providing an output voltage and current up to 12 kV and 1.25 A, respectively. The cathode voltage V_C is measured with a high voltage probe (Picotech TA044 1000:1) and the arc current I is measured with a current probe (Tektronix TCP303) and a signal amplifier (Tektronix TCPA300). Both signals are recorded on a Tektronix TDS 2012B oscilloscope.

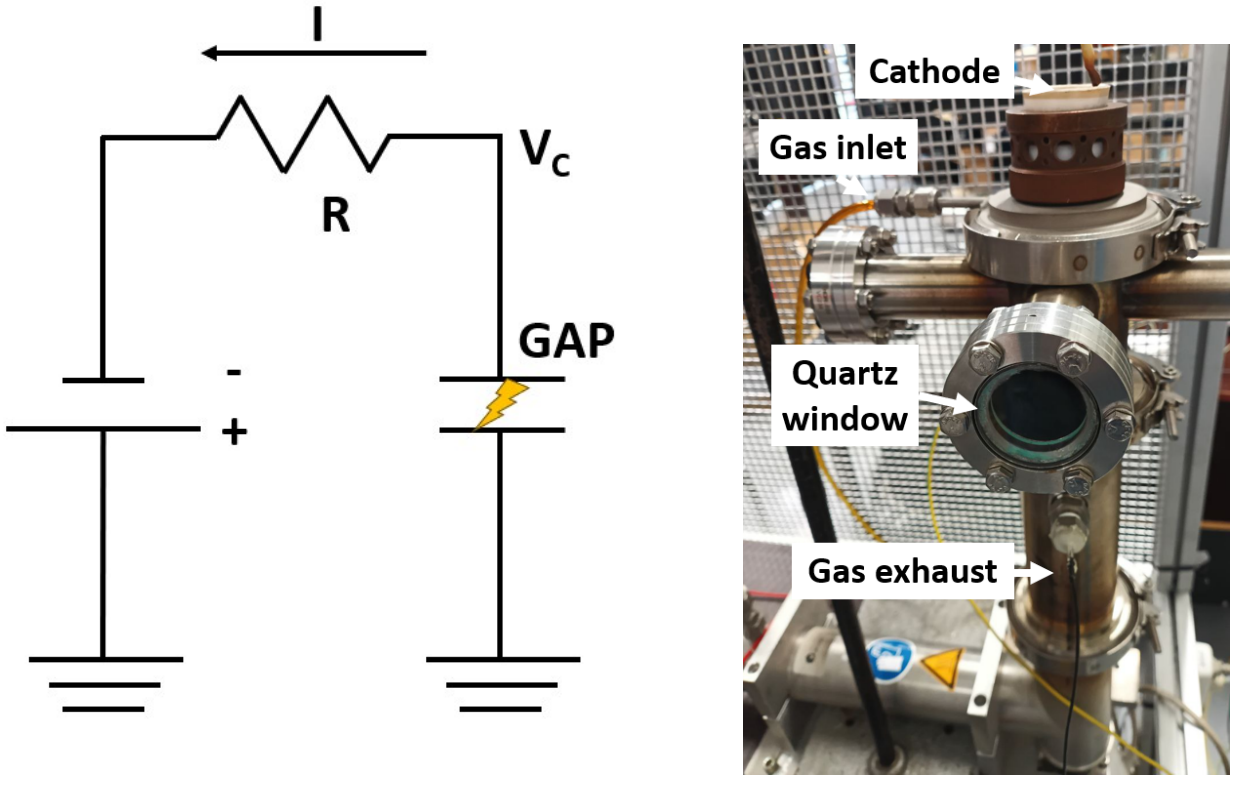

(a) (b)

Figure 3.1: Electric schematics of the reactor (a) and picture of the GAP (b).

The details of the stainless steel electrodes in the gliding arc reactor are schematized in figure 3.2. The inner diameters of the electrodes are 17.5 mm and 14.2 mm for the cathode and the anode, respectively, thus forcing the gas into a reverse vortex flow as explained in section 2.5.1. The cathode is electrically insulated through a Teflon fit and is separated from the anode, which is in direct contact with the exhaust tube, leaving 2 mm between the two electrodes.

The reactor is cooled with a 20 cm diameter industrial fan. The top of the exhaust tube of the

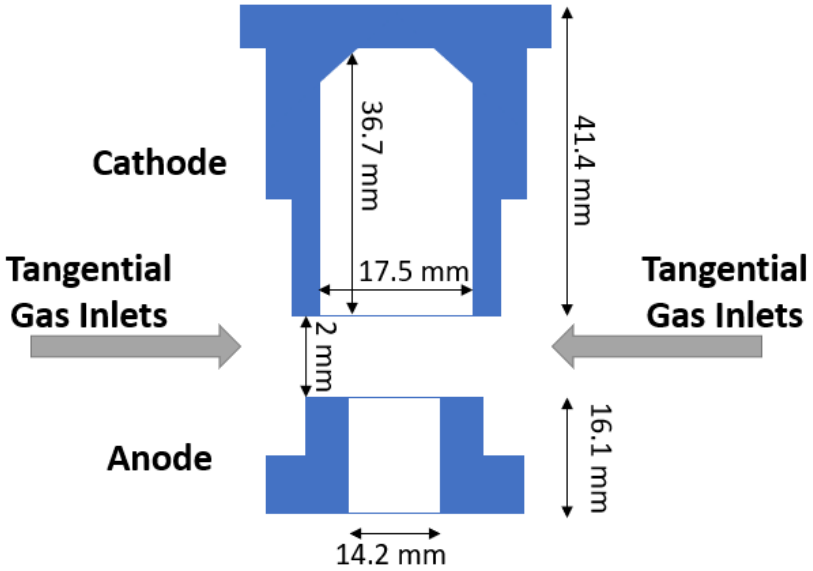

Figure 3.2: Scheme of the electrodes in which some of the most significant dimensions are reported.

Table 3.1: Main parameters of the GAP used in this thesis.

Parameter	Value
Mean power applied	0.2-0.65 kW
Current type	DC
Gas flux	8-10 slm
Gases used	N_2, O_2, Ar
Base pressure	1 atm
Cathode inner diameter	17.5 mm
Anode inner diameter	14.2 mm
Series resistance (R)	1-19 kΩ

reactor is equipped with four CF40 quartz windows allowing the plasma to be optically probed in the distance range of 10 and 40 mm from the anode. The main parameters of the GAP are summarized in table 3.1.

3.2 Fourier-transform infrared

Fourier-transform infrared (FTIR) is a technique used to obtain the infrared (IR) absorption spectrum of a gas. An IR beam is generated and passes through the gas contained in a gas cell where it is attenuated. Assuming a homogeneous density distribution, the intensity I(ν) of the attenuated beam can be described using the Beer-Lambert absorption law [78]

$$I(\nu) = I_0(\nu) \exp\big(-\Sigma_i n_i \sigma_i(\nu) L\big), \tag{3.1}$$

where $I_0(\nu)$ is the initial beam intensity, L is the absorption length, n_i and $\sigma_i(\nu)$ are the densities and the cross sections for photon absorption as a function of the incident frequency of all the sampled species, respectively. From this equation, the transmittance $T(\nu)$ can be defined as:

$$T(\nu) = \frac{I(\nu)}{I_0(\nu)}, \tag{3.2}$$

which, as is the case for this work, is often rewritten in terms of the absorbance $A(\nu)$, defined in equation (3.3) and directly proportional to the density of the absorbing species.

$$A(\nu) = \ln\left(\frac{1}{T(\nu)}\right) = \Sigma_i n_i \sigma_i(\nu) L \tag{3.3}$$

In some cases, it can be useful to refer to the line absorption (A_L), evaluated as [79]

$$A_L(\nu) = 1 - \frac{I(\nu)}{I_0(\nu)} = 1 - T(\nu), \tag{3.4}$$

which describes the fraction of the beam passing through the sampled volume.

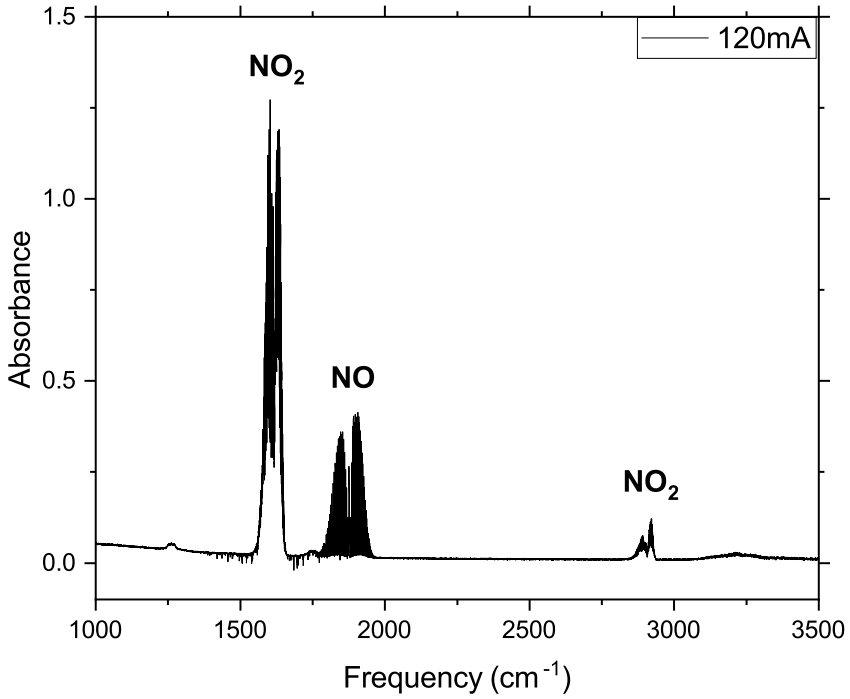

Figure 3.3: FTIR spectra acquired between 1000 and 3500 cm^{-1}. The absorption bands at 1876 cm^{-1} and 2916 cm^{-1} were used for NO and NO_2 respectively.

Figure 3.3 shows an example of an absorption spectrum in this thesis. The only species observed by FTIR absorption spectroscopy are NO and NO_2, measured through their transitions with main band heads at 1876 cm^{-1} and at 2916 cm^{-1}, respectively. The NO_2 band located at 1617 cm^{-1} was not used due to its high absorbance. An absorbance above 1 corresponds to less than 10 % of the incident photons with a specific wavelength reaching the detector. This is generally considered too low for the FTIR measurement to be consistent and for the linear dependency with the NO_2 concentration, described by the Beer-Lambert law to be valid. The considered NO transition corresponds to the absorption due to the excitations from the ground state to the first vibrational level [80]. The mentioned NO_2 transitions are, as well, excitation to low vibrational assignments from the ground state [81]. Considering that there is no overlap between the spectra of the two species, their contribution to the total absorbance can be easily distinguished. The absorbance $A(\nu)$ of NO and NO_2 in the presence of plasma can be integrated and compared with the calibrated spectra in order to deduce their absolute densities using Beer-Lambert's law.

$$\int A(\nu) = \int \sum_i n_i \sigma_i(\nu) d\nu = \sum_i n_i \int \sigma_i(\nu) d\nu = n_{NO} \int \sigma_{NO}(\nu) d\nu + n_{NO_2} \int \sigma_{NO_2}(\nu) d\nu \tag{3.5}$$

As NO and NO_2 are the only species probed by FTIR in the reactor, the equation is simplified in the last step. As a result of the fact that the integral of the cross sections is constant, the ratio between the absorbance of a plasma-generated gas mixture and the calibration gas set of measurements corresponds to their NO or NO_2 density ratio. Once the densities of the species have been determined, the total NO_x yield can be determined as:

$$\text{NO}_x \text{ Yield} = \frac{(n_{NO} + n_{NO_2})}{n_0} 100\%, \tag{3.6}$$

where n_0 is the initial gas density. Sometimes, the NO selectivity is also reported according to the following definition:

$$\text{NO Selectivity} = \frac{n_{NO}}{(n_{NO} + n_{NO_2})} 100\%. \tag{3.7}$$

The statistical error associated with the absorbance value is determined by repeating measurements for the same experimental conditions and estimated to be of the order of 1 % of the measured values.

At last, an important parameter for the characterization of the reactor performance is the energy cost EC, expressed in MJ/mol N, representing the energy used per mole of fixated N,

$$EC = \frac{P_T}{n_{NO_x} F}, \tag{3.8}$$

where F is the input gas flow rate in the reactor, n_{NO_x} is the NO_x density and P_T is the power required by the reactor. In literature, the energy cost is often evaluated by only considering the power of the plasma discharge itself (P_P), thus, neglecting the power losses in other components of the reactor (i.e. the pumping system, resistances placed in series with the reactor, cooling systems). The consequences of this assumption are discussed in chapter 4.

3.2.1 Implementation

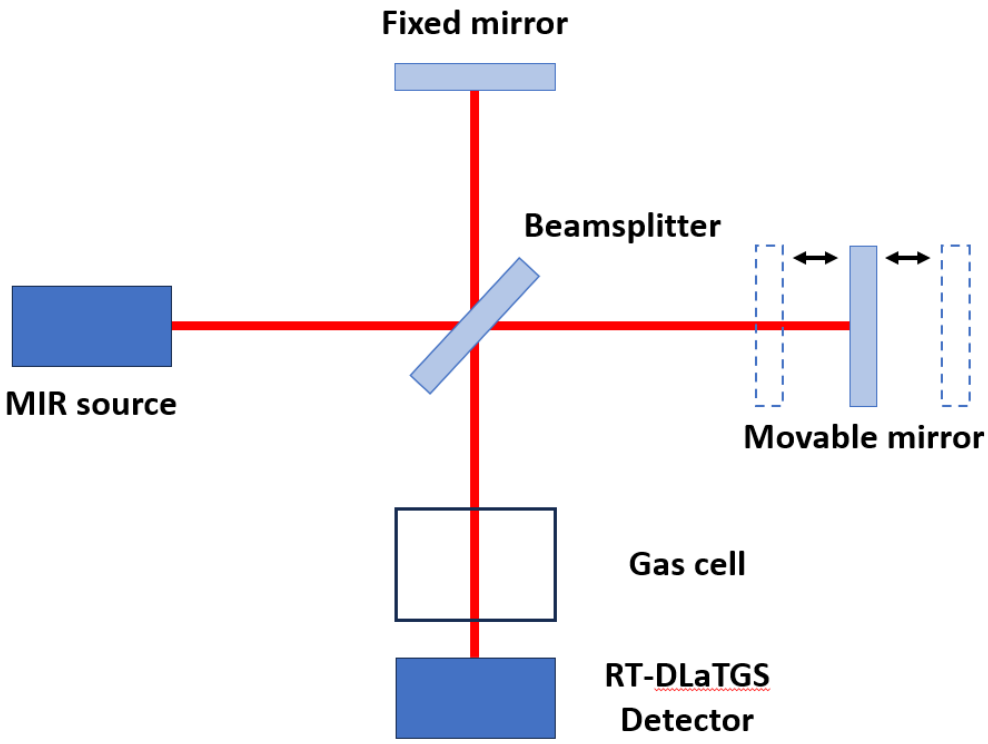

Figure 3.4: Schematic representation of the FTIR layout.

The GAP exhaust is connected to an external gas cell where the NO and NO_2 concentrations are measured with a Vertex 80v FTIR (Bruker) spectrometer. A simplified scheme of the FTIR setup is similar to a Michelson interferometer and is shown in figure 3.4. An FTIR is equipped with an IR light source, for this thesis a mid-IR light source is equipped, allowing for measurements between 350-5000 cm^{-1}. The beam passes through a KBr beamsplitter and reaches two mirrors, one has a fixed position and the other can be moved along the beam propagation axis. Both the beams are reflected again towards the beamsplitter where they interfere and are redirected to the internal RT-DLaTGS (Deuterated Lanthanum α-alanine-doped Triglycine Sulfate) detector, passing through the gas cell containing the gas to be sampled. The beam intensity as a function of the optical path length is measured and, by applying a Fourier transform the absorbance spectrum as a function of the frequency can be obtained.

The gas cell length is approximately 125 mm and is equipped with either two ZnSe or two Si windows. A 2 mm aperture is used, which gives a resolution of 1 cm^{-1}. For each measurement,

Table 3.2: Main parameters of the FTIR used in this thesis.

Parameter	Value
Model	Vertex 80v (Bruker)
IR source	0.2-0.65 kW
Beamsplitter	KBr
Detector	RT-DLaTGS
Spectral resolution	$1\,cm^{-1}$
Interferometer	Michelson
IR beam diameter	2 mm
Gas cell windows	ZNSe or Si
Gas cell path length	125 mm

20 spectra acquired in the range between $1000\,cm^{-1}$ and $3500\,cm^{-1}$ were averaged. In order to obtain the absolute densities for the produced NO_x species, a calibration was performed using gas mixtures of 1 % NO mixed in Ar and 2 % NO_2 in Ar. The main parameters of the FTIR are summarized in table 3.2.

3.3 Laser-induced fluorescence

Laser-induced fluorescence (LIF) is a widely implemented optical diagnostic technique that allows for the detection of ground-state or long-lived metastable atoms and molecules [67, 68]. The principle of LIF, briefly schematized in figure 3.5, can be described in two steps. First, given a molecule (or an atom) in an excitation state j, a laser photon can be absorbed, thus, exciting the molecule to a higher excitation state i. The energy difference between the two states corresponds to the energy of the absorbed photon ($h\nu_{ji}$). At last, the excited molecule can de-excite to a lower excitation state k by spontaneously emitting a photon of energy $h\nu_{ik}$ which can then be captured and observed with an Intensified Charge-Coupled Device (ICCD) camera.

The fluorescence intensity (I_{LIF}), corresponding to the laser-induced excitation from state j to i and the consequent de-excitation from state i to k can be described as:

$$I_{LIF} \propto A_{ik} n_i, \tag{3.9}$$

where A_{ik} is the Einstein transition probability for the spontaneous emission from the excitation state i to k and n_i is the density of molecules in the state i. However, the state i is populated due to the absorption of the laser by molecules at the initial state j. By assuming the laser absorption is not saturated and a laser pulse duration shorter than the measurement time [68], n_i can be expressed as:

$$n_i \propto n_j I_{las} \frac{B_{ji}}{Q_i + \sum_l A_{il}}, \tag{3.10}$$

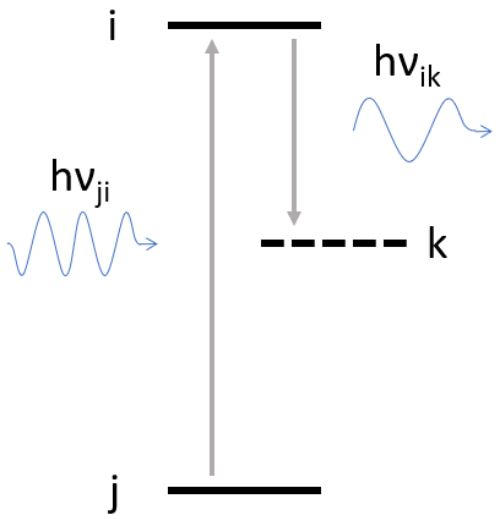

Figure 3.5: Basic scheme for the laser-induced fluorescence process.

where n_j is the density of molecules in the state j, I_{las} is the laser intensity, B_{ji} is the absorption coefficient from state j to i, and Q_i and $\sum_l A_{il}$ are the depopulation rates due to collisional energy transfers and spontaneous emission, respectively. By combining equations (3.9) and (3.10), the following expression for I_{LIF} can be obtained:

$$I_{LIF} = C n_j I_{las} \frac{A_{ik} B_{ji}}{Q_i + \sum_l A_{il}}, \tag{3.11}$$

where C is a constant that depends on quantities such as the camera sensitivity, the sampled volume, and the solid angle covered with the camera.

From the depopulation rates, a decay time τ for the state i can be defined as:

$$\tau = (Q_i + \sum_l A_{il})^{-1}. \tag{3.12}$$

If τ is larger than the laser pulse duration it can be easily measured. This is usually done by setting the camera to repeatedly acquire the I_{LIF} with an increased delay between the beginning of the acquisition and the laser pulse. To ensure that the LIF signal is captured until all the molecules excited by the laser have emitted a fluorescence photon, the camera acquisition time should be set to be much longer than τ.

The complications due to the decay time being comparable to the laser pulse duration are discussed in chapter 5.

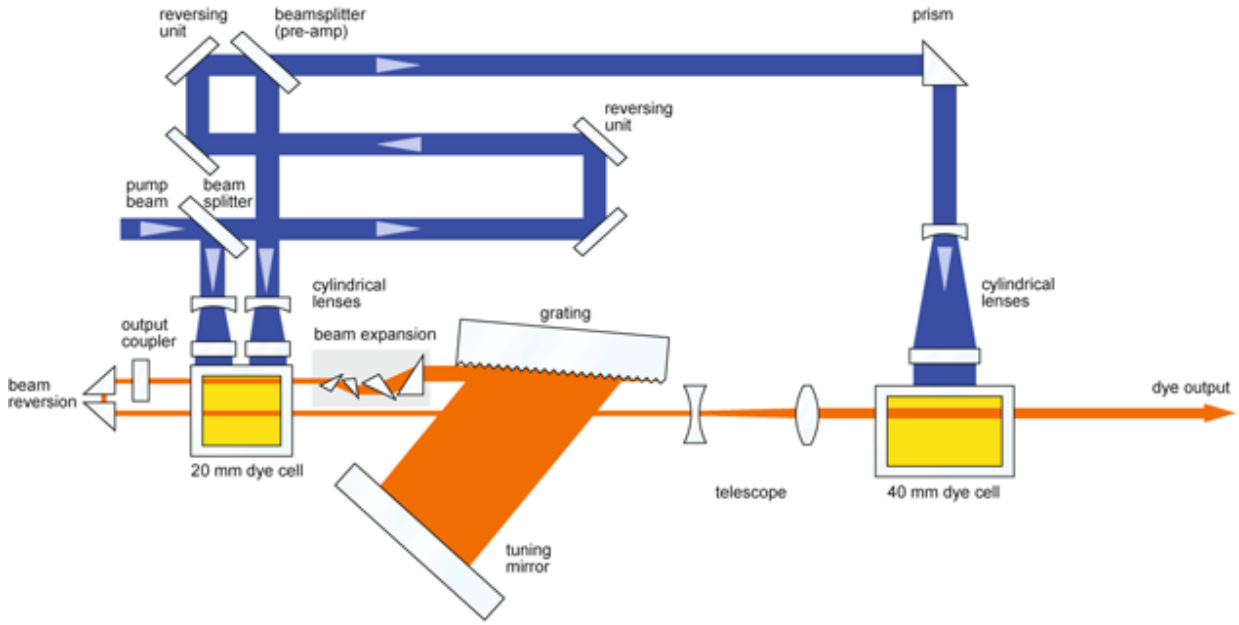

Figure 3.6: Scheme of the dye laser used in this thesis. Reprinted from [82].

3.3.1 Implementation

For this thesis, the Sirah Cobra Stretch pulsed dye laser setup was used (a detailed scheme is provided in figure 3.6), this type of laser source can access a broad range of wavelengths according to the choice of the dye. A Nd:YAG (neodymium-doped yttrium aluminum garnet) laser at 355nm with a 10 Hz repetition rate is used to pump, through a system of mirror, lenses, and beamsplitters, a solution of Coumarin 2 dye in methanol in two dye cells. Such a solution emits photons in a continuous spectrum in the range between 434 nm and 463 nm, with a peak at 448 nm [83]. The emitted light is filtered with a grating which can be tuned to obtain a monochromatic beam at the desired wavelength. The monochromatic beam passes through both the dye cells for its intensity to be amplified. The beam is generated in pulses with a Gaussian profile in time with a 5 ns FWHM.

Generally, dyed lasers cannot generate light with a shorter wavelength than the pump laser and many species of interest require photons in the ultra-violet region to be excited. For this reason, the laser source is equipped with a second harmonic generation crystal. Such a system consists of a nonlinear crystal (a β Barium Borate - BBO crystal is used in this thesis), i.e. a crystal exhibiting an optical nonlinearity, which, through a virtual intermediate state, allows different photons with different or same energies to be converted into a single photon with summed energy [84]. Second harmonic generation implies the participation of two photons and is most often reported for two low-energy photons with the same energy [84], therefore resulting in a photon with half of the initial wavelength. The photons were then separated with a system of prisms, allowing the selection of only the frequency-doubled photons. This allowed to obtain a tunable

beam in the wavelength range between approximately 217 nm and 231 nm.

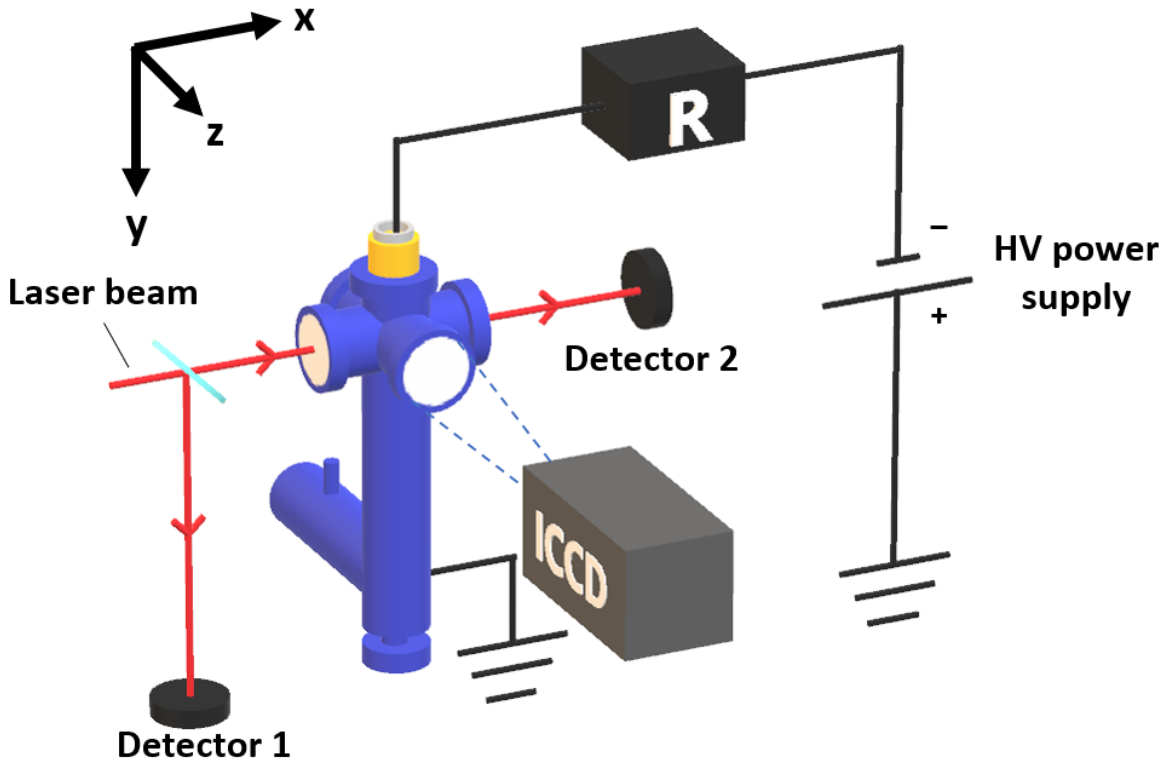

Figure 3.7: Scheme of the experimental setup highlighting the electrical circuit and the laser beam path, which probes the plasma afterglow.

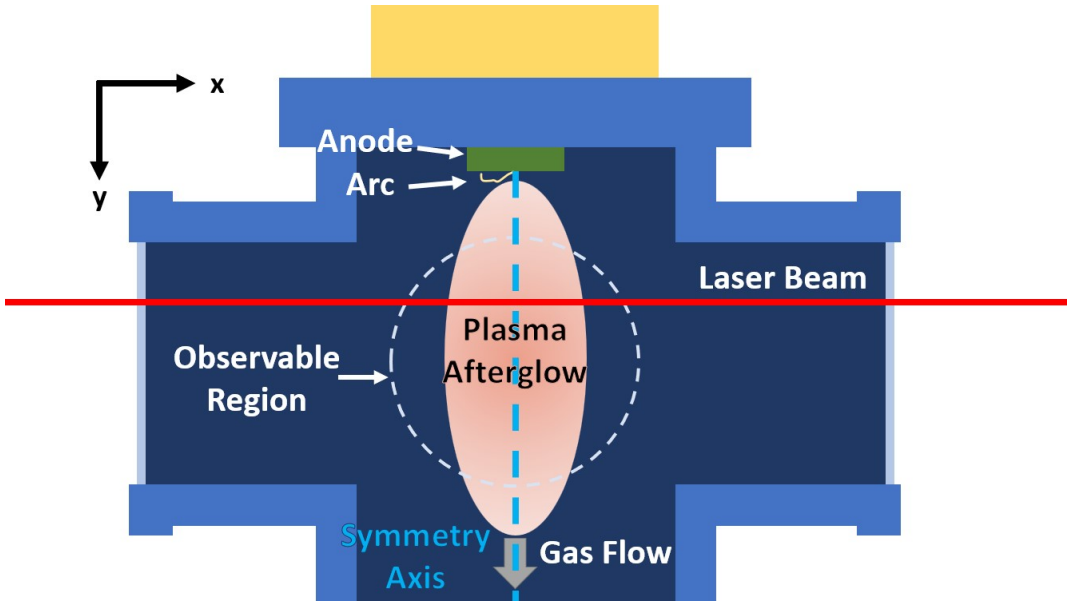

Figure 3.8: Cross section of the GAP system, seen from the ICCD, showing the region of the plasma afterglow. The region where LIF could be observed is shown with a white circular dashed line.

Before being injected into the plasma afterglow, the beam is collimated with a f/50cm spherical lens, focusing the beam in the GAP center. The LIF emission from the plasma afterglow is collected with an Andor iStar 740 Intensified Charge-Coupled Device (ICCD) camera equipped with a CERCO UV f/100cm lens and a 248(10) nm bandfilter. The camera is synchronized with the laser using a DG645 digital delay generator and is placed perpendicularly with respect to the beam propagation path. ICCD cameras are often used as they allow the observation of the spatial distribution of the LIF signal. As shown in figure 3.7, before being injected into the afterglow, a small part of the initial laser beam is redirected toward an Ophir PE-9 energy meter head ("detector 1"). A second identical energy meter head ("detector 2"), also used as a beam dump, was used to measure the beam energy after passing the plasma afterglow. Due to the reactor design, the region that can be probed with LIF is limited and depends on the size of the quartz windows as schematized in figure 3.8. This allowed the plasma afterglow to be optically probed in the distance range (from the anode) of 10 and 40 mm and prevented the electric arcs from being observable with the camera. Near the anode (i.e., GAP reactor outlet) a small arc is drawn, which is typically observed just a few mm outside the GAP [47, 85]. The main parameters of the LIF are summarized in table 3.3.

Table 3.3: Main parameters of the LIF used in this thesis.

Parameter	Value
Dye laser	Sireh Cobra Stretch
Pump laser	Nd:YAG (335 nm)
Dye	Coumarin 2 (in methanol)
Dye emission range	434-463 nm
Pulse repetition rate	10 Hz
Pulse duration	≈5 mm
Energy per laser pulse	100-200 µJ
Non-linear crystal	BBO
Laser wavelength control unit	WS6-200 wavemeter
ICCD model	Andor iStar 740
Camera lens	CERCO UV f/100cm lens
Camera bandfilter	248(10) nm

Chapter 4

Laser-induced fluorescence-based characterization of the afterglow

After introducing the fundamental theoretical concepts and a brief description of the experimental apparatus, the following chapter aims to investigate plasma-based NF on a fundamental level, focusing on plasma chemistry. Most notably, the goal is to provide experimental insights, via optical diagnostics, into a GAP.

Specifically for a N_2-O_2 GAP, this approach is not common due to the difficulty of performing this kind of analysis. Indeed, in atmospheric plasmas, the high concentration of absorbers, such as NO, can cause the laser beam to be strongly absorbed along its propagation in the discharge, effectively posing a challenge to well-established laser-induced fluorescence methods. In this chapter, a new approach dealing with laser-based excitation of separate rotational lines is proposed and used to provide 2D spatial distribution of the gas temperature and the NO concentration in different operating conditions of the GAP and to study the effects of an external cooling system on the GAP's performance.

The results related to this chapter are published in: F. Manaigo, O. Samadi Bahnamiri, A. Chatterjee, A. Panepinto, A. Krumpmann, M. Michiels, A. Bogaerts and R. Snyders, "Electrical stability and performance of a Nitrogen-Oxygen atmospheric pressure gliding arc plasma", submitted (2024)

4.1 Introduction

On a fundamental level, it is necessary to investigate plasma-based NF plasma chemistry to understand and improve the performance of this technology. One of the main tools for this investigation, both for GAP and RGA plasmas, is the use of simulations to model the vibrational and gas temperatures and species concentration (NO, NO_2, N, O) in the active region of the plasma [41, 42, 52, 86]. As an example, a kinetic model proposed in [41] shows the time evolution of the number densities of NO, NO_2, N and O in the GAP operating with N_2 and O_2, but the experimental benchmark was limited to the final NO_x yield and energy cost [41]. There is, therefore, a strong need to experimentally determine the plasma species densities and gas temperature to support these modeling results. However, as discussed in section 2.6.2, to the author's knowledge, no LIF-based experimental studies of a GAP operating at atmospheric pressure with N_2-O_2 are reported. This, together with the limited applicability of OES-based techniques due to the overlapping between the O_2 Schumann-Runge bands and the N_2 second positive system, cause a blind spot on the experimental characterization of the N_2-O_2 GAP plasma chemistry. Hence, the determination of the two-dimensional distribution of both the gas temperature and the NO ground state density with LIF is the main goal of this chapter.

LIF, as a diagnostic method for NO-containing plasmas, is widely used for low-pressure plasmas [70, 87], atmospheric pulsed plasmas [71] or, more in general, when small (up to few tens of ppm) concentrations of NO are involved [88, 89]. Generally in literature, NO bandheads corresponding to high absorption are measured to maximise the LIF signal intensity. However, as GAPs at atmospheric pressure normally produce rather high NO_x densities, the high concentration of relevant absorbers, such as NO, may impose essential restrictions for the use of "classical" laser-induced fluorescence methods (dealing with excitation in the bandhead vicinity), as the laser beam would be strongly absorbed along its propagation. Indeed, the measurement of the beam energy (or of its intensity) is crucial when comparing different LIF signals and is, therefore, necessary to build a LIF line profile. Since this was the case for the studied GAP, a new approach dealing with laser-based excitation of separate rotational lines is proposed. In this case, due to a non-saturated absorption regime, simultaneous and reliable measurements of both the NO density and the gas temperature (using a reference fitting spectrum) are possible. The proposed method is applied to provide a two-dimensional map for both the NO density and the gas temperature at different plasma conditions.

This method is then used to determine the spatial distribution of the gas temperature and NO concentration in the afterglow of the plasma, i.e., a few mm below the arc in a GAP used for NF and to evaluate the impact of the experimental parameters on these features. The study of the afterglow can prove to be important to gain more insight into possible back-reactions, and to study quenching effects. To get a complete picture of the process, the concentration measurements are compared with the gas composition at the exhaust as measured by Fourier transform infrared (FTIR) spectroscopy. The results show that the input gas flow rate strongly alters the plasma shape, which appears as an elongated column at low input gas flow rate and spreads laterally as the flow

rate increases. Moreover, based on temperature map analysis, a clear correlation between the gas temperature and NO concentration is found. The proposed method may be interesting for plasma-chemical analysis of the discharges with high molecular production yields, where knowledge of both molecular concentration and gas temperature is required.

Finally, the novel LIF-based method is used to study the effect of an external cooling system. A few works, using simulation models, have highlighted the critical role of gas temperature quenching on the reaction chemistry [41, 52, 90] preventing the newly formed NO_x molecules to undergo the reverse Zeldovich reaction and decompose back to N_2 and O_2. Therefore, an experimental insight can be of crucial importance for the understanding of the role of gas temperature in the optimization of the process.

4.2 LIF methodology implementation

4.2.1 Temperature measurements

The region near the band head of the $NO(X, v = 0) \rightarrow NO(A, v = 0)$ transition was avoided due to a strong laser absorption causing the absorption signal to scale non-linearly with the absorber density. Therefore, LIF was performed with the wavelengths around the two peaks observed at 224.792 nm and at 224.823 nm where the absorbance was lower, allowing the laser energy to be detectable at detector 2 and, thus, to estimate the beam energy. With this configuration, the J = 33.5 (Q-branch) and the J = 21.5 (R-branch) rotational lines of the transition NO(X, $\nu = 0$) $\rightarrow$ NO(A, $\nu = 0$) could be, respectively excited. The NO then de-excited to the NO(X, $\nu = 2$) state corresponding to a rotational band with a bandhead at about 248 nm. In this thesis, only this line ratio demonstrated high T_{gas} sensitivity, along with a linear absorption regime and a clearly detectable laser beam energy at detector 2 and, therefore, it was chosen for T_{gas} measurements.

Figure 4.1 shows an example of the LIF image captured with the camera. The axes represent the horizontal position and the distance in the afterglow, measured from the anode (as shown in figure 3.8) expressed in mm. To study the evolution of the LIF signal along the laser beam, the region corresponding to the beam path was horizontally subdivided into smaller integration areas where the LIF signal was analyzed separately. In general, the LIF signal intensity (I_{LIF}) corresponding to the laser-induced excitation from state j to i and the consequent de-excitation from state i to k can be expressed as follows [68]:

$$I_{LIF} = C n_j E_{las} \frac{A_{ik} B_{ji}}{Q_i + \sum_l A_{il}}, \tag{4.1}$$

where C is a constant, n_j is the density of the state j, E_{las} is the energy of the laser pulse, A_{ik} and B_{ji} are the Einstein emission and absorption coefficients, respectively, A_{il} is the Einstein emission coefficient from state i to a generic state l and Q_i is the collisional quenching rate. Equation (3.11) represents a linear regime when fluorescence intensity scales with the laser energy. An example

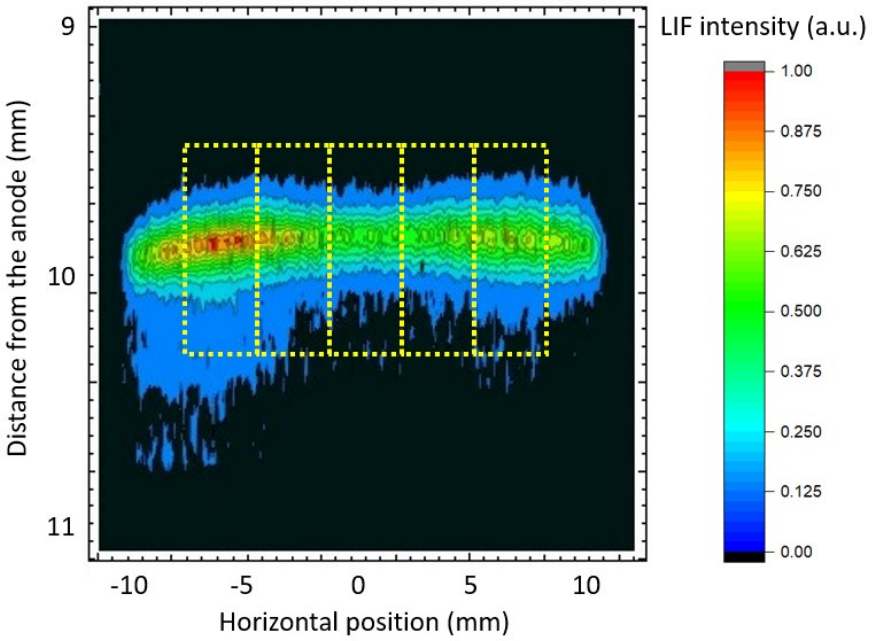

Figure 4.1: Example of a LIF signal measured. The beam path region was subdivided into smaller integration areas highlighted with the dashed boxes. The current was set at 150 mA and the input gas flow rate at 10 slm.

of the LIF intensity spectrum, and the fit evaluated with LIFBASE, a free spectroscopy software, in the vicinity of $J = 33.5$ and $J = 21.5$ NO(X, $\nu = 0$) lines is shown in figure 4.2 together with the line absorption (A_L), evaluated as [79]

$$A_L = 1 - \frac{I_{LIF,f}}{I_{LIF,i}} = 1 - \frac{E_{las,f}}{E_{las,i}}, \tag{4.2}$$

where the indexes i and f refer to the quantity being measured before and after passing through the probed region, respectively. Since the laser frequency and the pulse duration were constant, A_L can be evaluated using the laser energy. As shown in figure 4.2, the laser line absorption values in this chapter are high and, typically, between 0.5 to 0.9. A high A_L was observed between the $J = 33.5$ and the $J = 21.5$ absorption peaks but did not result in a photon emission around 248nm (the LIF intensity in figure 4.2(a) between the two peaks is close to zero). This could be caused by the presence of NO_2, also produced in the GAP, which is known to have a non-negligible and continuous absorption spectrum around 224nm, which results in emission at different wavelengths compared to NO [91].

Due to the high laser absorbance, the energy of the laser in equation (3.11) could not be assumed constant along the absorption path. Additionally, the evolution of the beam energy profile was affected by the NO density profile, which, as discussed in section 4.3 in terms of concentration, greatly varied for different initial conditions. To still be able to restore the laser energy in

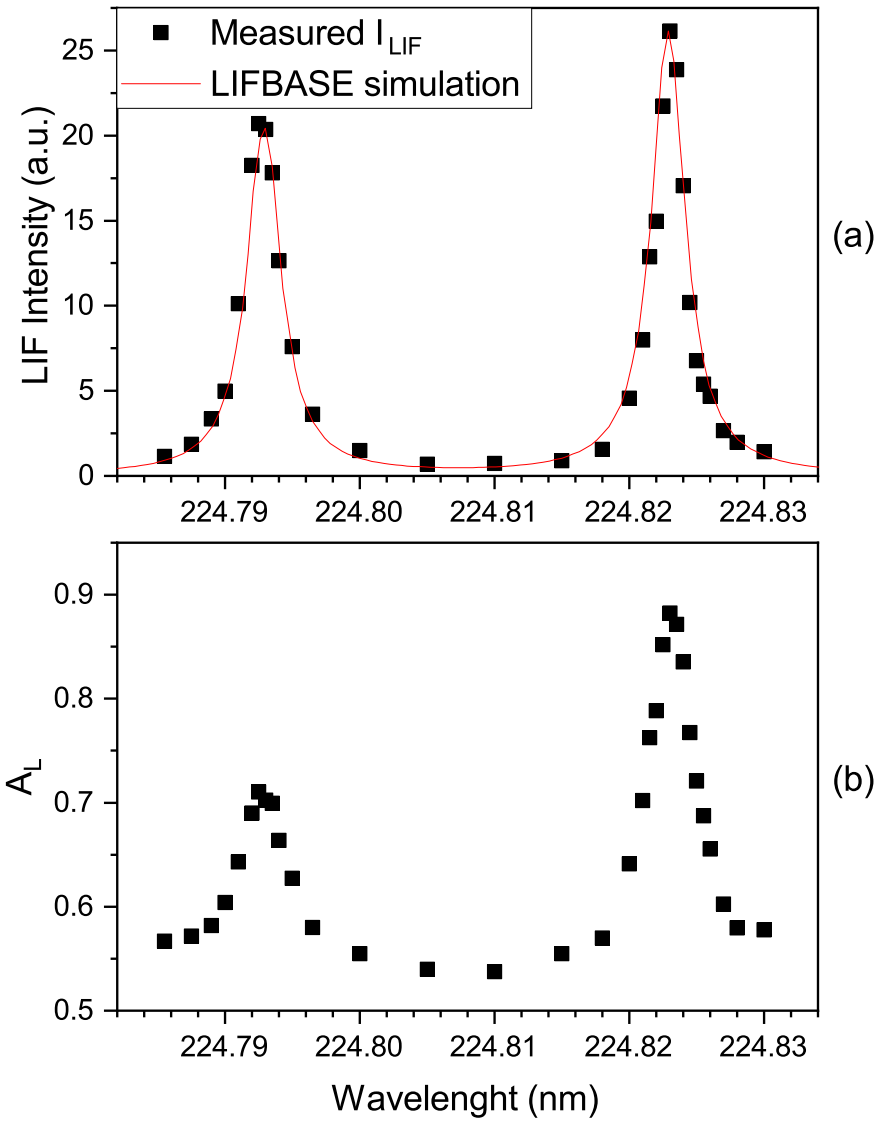

Figure 4.2: Intensity of the LIF signal (a) and laser beam line absorption A_L (b) as a function of the laser beam wavelength. The current was set at 150 mA and the input gas flow rate at 10 slm. The LIF intensity spectrum simulated with LIFBASE is shown in red.

the point of interest (middle of the discharge), considering the geometry of the electrodes and the reactor, a cylindrical symmetry for both the gas temperature and species density in the discharge volume was assumed. In figure 3.8 the symmetry axis, corresponding to the center of the anode and, thus, of the reactor, is marked with a vertical light blue dashed line. The horizontal position is centered on the symmetry axis. With this assumption, the symmetry axis separates the laser beam

path into two sections characterized by the same length and the same NO concentration (which is not uniform, but equal between the two regions), thus allowing the laser beam intensity at the center of the GAP to be evaluated with the Beer-Lambert law. If L is the optical length of the GAP and c is the average NO concentration, from the general equation, the laser intensities measured at detector 2 $I_{las}(L)$ and at the center $I_{las}(L/2)$ are

$$I_{las}(L) = I^0_{las} e^{-\epsilon c L}, \tag{4.3}$$

$$I_{las}(L/2) = I^0_{las} e^{-\epsilon c \frac{L}{2}}, \tag{4.4}$$

where, I^0_{las} is the initial laser intensity and ϵ is the molar absorption coefficient. By multiplying equation (4.3) by I^0_{las}, the relation between $I_{las}(L/2)$ and the measurable laser intensities I^0_{las} and $I_{las}(L)$ becomes

$$I_{las}(L) \cdot I^0_{las} = I^0_{las} I^0_{las} e^{-\epsilon c L} = \left(I_{las}(L/2)\right)^2 \tag{4.5}$$

Since the laser intensity and the laser energy are linearly dependent, the energy of the beam at the center of the GAP can be expressed as

$$E_{las}(L/2) = (E^0_{las} E_{las}(L))^{\frac{1}{2}}. \tag{4.6}$$

The LIF spectra, as the one shown in figure 4.1, were then integrated and normalized to $E_{las}(L/2)$. For each experimental condition, the laser beam wavelength was scanned between 224.785 nm and 224.830 nm, as shown in figure 4.2(a).

It should be noted that using $E_{las}(L/2)$ to normalize the LIF signal from an integration area that is not centered in the symmetry axis is a simplification. The inaccuracies caused by this approach are corrected by imposing the symmetry hypothesis previously discussed and averaging the T_{rot} and NO density calculated from integration areas with the same distance from the symmetry axis. The peaks of the LIF intensities followed a Lorentz distribution, which is usually associated with collisional broadening, which becomes dominant at atmospheric pressure [92].

The 224.792 nm and 224.823 nm ($J_{33.5}/J_{21.5}$) line ratio showed a rather high sensitivity to T_{rot}. Its evolution was simulated with LIFBASE 2.1.1 software [93] and is shown in figure 4.3. For this reason, the $J_{33.5}/J_{21.5}$ line ratio was used to evaluate the T_{rot} of NO(X, $\nu = 0$). As the rotational-translational relaxation is estimated to be in the ns range [94], much shorter than the duration of the arc and the time the gas requires to reach the probed region, both of the order of a few ms [48], T_{rot} is assumed to be equal to the gas temperature T_{gas}. The measured T_{rot} were then adjusted to impose the cylindrical symmetry by averaging the two points at the same distance from the symmetry axis.

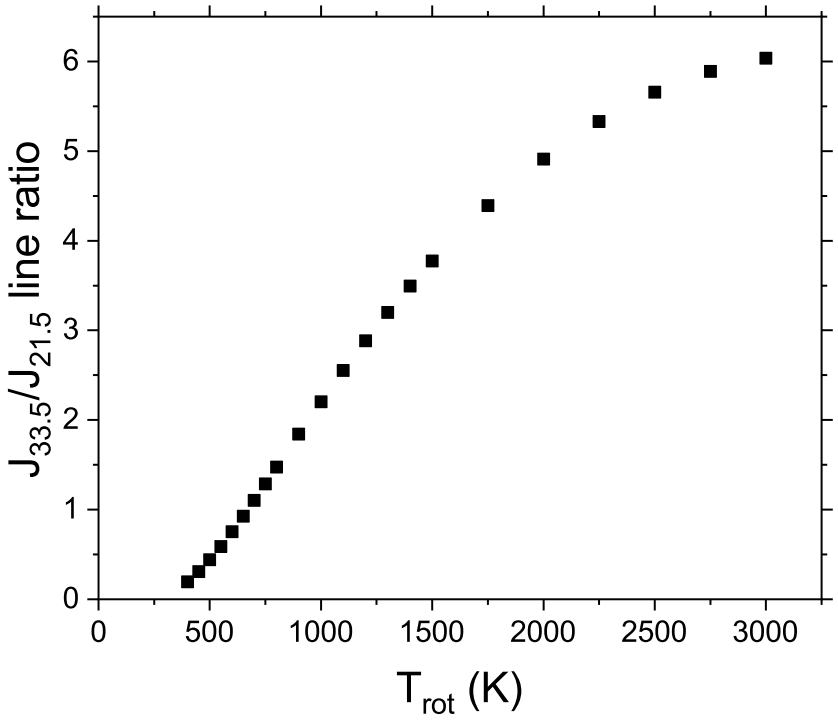

Figure 4.3: $J_{33.5}/J_{21.5}$ line ratio, simulated with LIFBASE software, as a function of T_{rot}.

4.2.2 Density measurements

For the density determination, the $J = 21.5$ peak (at 224.823 nm) was taken due to the I_{LIF} intensity of the $J = 33.5$ peak being too low in the calibration spectra. The density n_j can be extracted from equation (3.11):

$$n_j \propto \frac{I_{LIF}}{E_{las}(L/2)} \frac{1}{\tau}, \tag{4.7}$$

where j corresponds to the NO$(X, v = 0, J = 21.5)$ state and τ is the decay time (whose measurement is discussed in section 4.2.3) defined as:

$$\tau = (Q_i + \sum_l A_{il})^{-1}. \tag{4.8}$$

n_j can be obtained by comparison with the I_{LIF} from the calibration gas mixture. Considering equation (4.7) for both the measurements and the calibration, the relation between n_j and the NO$(X, v = 0, J = 21.5)$ density of the calibration gas ($n_{j,cal}$) becomes:

$$n_j = n_{j,cal} \frac{I_{LIF}}{E_{las}(L/2)} \frac{E_{las,cal}(L/2)}{I_{LIF,cal}} \frac{\tau_{cal}}{\tau}, \tag{4.9}$$

where the index *cal* refers to the quantities relative to the calibration gas mixture. The fraction of the NO(X) molecules in the NO$(X, v = 0, J = 21.5)$ state is described by the vibrational and rotational statistical factor $\Phi_{J=21.5}$ and $\Phi_{v=0}$, respectively, which depend on T_{gas}. Thus, in order to link n_j with the NO(X) density (n_{NO}), an additional correction is required.

$$n_{NO} = n_{NO,cal} \frac{\Phi_{J=21.5,cal}}{\Phi_{J=21.5}} \frac{\Phi_{v=0,cal}}{\Phi_{v=0}} \cdot \frac{n_j}{n_{j,cal}}, \tag{4.10}$$

where both $\Phi_{J=21.5}$ and $\Phi_{v=0}$ are normalized ($\sum_J \Phi_J = \sum_v \Phi_v = 1$). The statistical factors were simulated with LIFBASE [93], using the T_{rot} measured by LIF. Considering the pressure and T_{gas} in the GAP, the vibrational-translational relaxation time is estimated to have the order of magnitude of few μs [49, 94]. As, both the time required by the gas to reach the probed duration and the typical duration of the arc is of the order of a few ms, $T_{vib} = T_{rot}$ is assumed for the evaluation of $\Phi_{v=0}$. This is a reasonable assumption as, in atmospheric pressure GAPs, T_{vib} and T_{rot} are generally considered in equilibrium [21].

Finally, as in this chapter, rather than n_{NO}, the NO(X) concentration (c_{NO}) is used, an additional correction is introduced using the ideal gas law.

$$c_{NO} = c_{NO,cal} \frac{T_{gas}}{T_{gas,cal}} \cdot \frac{n_{NO}}{n_{NO,cal}} \tag{4.11}$$

where $c_{NO,cal}$ is the NO(X) concentration of the calibration gas mixture, which is known.

4.2.3 LIF effective decay time

Table 4.1: Parameters of the fit shown in figure 4.4.

	slope (ns^{-1}/Ar%)	y-intercept (ns^{-1})
J=33.5	$-(3.28 \pm 0.08) \cdot 10^{-3}$	0.333 ± 0.007
J=21.5	$-(3.2 \pm 0.2) \cdot 10^{-3}$	0.32 ± 0.02

The effective decay time, τ, is a crucial parameter for the calibration. As a consequence of equation (4.7), its measurement is required to determine n_j, and thus c_{NO}. While for the calibration gas mixture (NO in Ar), the measurement of τ_{cal} is relatively simple, it can prove to be more challenging when plasmas at atmospheric pressure are involved since τ can be comparable to or shorter than the laser pulse duration.

In this chapter, as O_2 is known to be the main quencher for NO [95], τ was measured by diluting the input gas flow of N_2 and O_2 with Ar, a relatively weak quencher. This allowed to keep tau in the ns range and measure it directly with the 5 ns pulsed dye laser [96, 97]. More specifically, it has been shown that the NO(A) decay rate, defined as τ^{-1} decreases linearly as the Ar concentration increases [98]. Figure 4.4 shows the evolution of τ^{-1} as the Ar fraction increases for both the

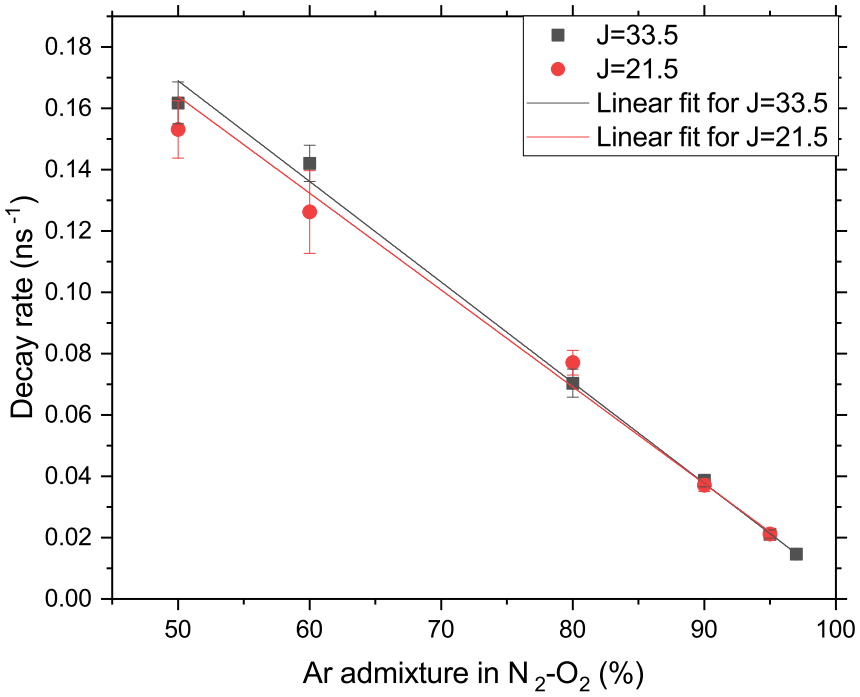

Figure 4.4: decay rate of NO($X, \nu = 0, J = 33.5$) (224.792 nm) and NO($X, \nu = 0, J = 21.5$) (224.792 nm) excited states as a function of the Ar percentage of the N_2-O_2 input gas mixture.

fluorescence lines. The total input gas flow rate was kept at 10 slm, the current at 150 mA and the beam distance from the anode was set at 10 mm. The measurements were fitted with a straight line, whose parameters are listed in table 4.1. From the y-intercept of the fit, τ associated to the $J = 33.5$ and $J = 21.5$ states is estimated to be (3.00 ± 0.07) ns and (3.1 ± 0.2) ns, respectively.

As previously mentioned, for the calibration gas mixture a direct measure of the decay time, $\tau_{cal} = 102$ ns, was possible.

4.2.4 Self-absorption

With a high density of absorbers, self-absorption, i.e. the absorption in the plasma of the fluorescence light, can lower the measured I_{LIF}. While this effect would introduce an underestimation of c_{NO}, it can be neglected for the T_{gas} determination, assuming that both the peaks $J = 33.5$ and $J = 21.5$ suffer from the loss of the same fraction of I_{LIF} and, thus, their line ratio should not be affected.

More generally, a critical NO density for self-absorption to become non-negligible is reported to be 2×10^{17} cm^{-3} [99]. In this chapter, as described in section 4.3, the highest n_{NO} is obtained for 8 slm and 250 mA, where a c_{NO} and T_{gas} of 1.2 % and 610 K is measured, respectively. Using the ideal gas law, this corresponds to a n_{NO} of approximately 1.4×10^{17} cm^{-3}. Overall, n_{NO} is

measured to be in the range between 3.5×10^{16} cm^{-3} and 1.4×10^{17} cm^{-3}, which is lower than the critical NO density, allowing to neglect the effects of self-absorption in this chapter.

4.3 Process evaluation

The 2D temperature maps in the plasma afterglow for different discharge conditions show spatial non-uniformity. This can be observed in figures 4.5(a) and 4.5(b), which show the spatial evolution of the T_{rot} distribution for NO(X,$v = 0$) for two different input gas flow rates of 8 slm and 10 slm with the same composition (50% N_2 + 50% O_2). As described in section 3.3.1, the y-axis measures the vertical distance in the afterglow, measured from the anode (reactor outlet) and the x-axis represents the horizontal position i.e. the distance from the center.

It is observed that the difference in the temperature distribution between the two measurement sets of 8 slm and 10 slm correlates with the different plasma shapes. A higher input gas flow rate pushes the plasma radially, causing it to expand towards the reactor walls. This generates a central region where T_{gas} is cooler than on the sides and limits the axial extension of the plasma. It is therefore observed that the T_{gas} distribution shows a rather high sensitivity to the input gas flow rate. With the lower input gas flow rate, the plasma region forms a column and remains confined along the center of the reactor, showing little difference within the region probed with the laser beam. Since, in this case, the plasma has a longer extension, additional measurements at 30 mm from the anode were acquired for 8 slm. Similarly to what is discussed with 10 slm, an elongation of the vertical plasma column is observed as the current increases, however, due to the constraints of the reactor design, probing further away from the anode was not possible.

Similarly, the spatial evolution of c_{NO} is shown in figures 4.6(a) and 4.6(b). In comparison with the 2D T_{gas} map, c_{NO} is higher in areas where T_{rot} is lower, reaching concentrations up to 1.1 %. To explain this trend, the oxidation of NO into NO_2 should likely be considered as the rate for $NO + O \rightarrow NO_2$ becomes dominant in the temperature range between 1000 and 2000 K [53].

Figure 4.7 summarizes the maximum c_{NO} measured in each experimental condition. The relative error on c_{NO} is estimated to be of approximately 9 %. Such estimation is obtained by propagating the errors on the measurement of τ and E_{las} (the latter is estimated to be approximately 5 % of E_{las}). The instrumental error due to the ICCD measurement is considered to be negligible. As a comparison, the NO + NO_2 yield (i.e. the final NO + NO_2 concentration) and the NO yield measured with the FTIR are also provided. The statistical error associated with the NO and NO_x yield is determined by repeating measurements for the same experimental conditions and estimated to be of the order of 1 % of the measured values. The maximum c_{NO} measured with LIF (which corresponds to regions where the fraction of NO(X) is higher) is consistently higher than the NO yield measured by FTIR. This is expected, as previously mentioned, due to the loss of NO caused by the Zeldovich back-reaction and by the conversion to NO_2. On the other hand, the NO_x yield is higher, suggesting that the conversion into NO_2 in the region probed with LIF is already significant.

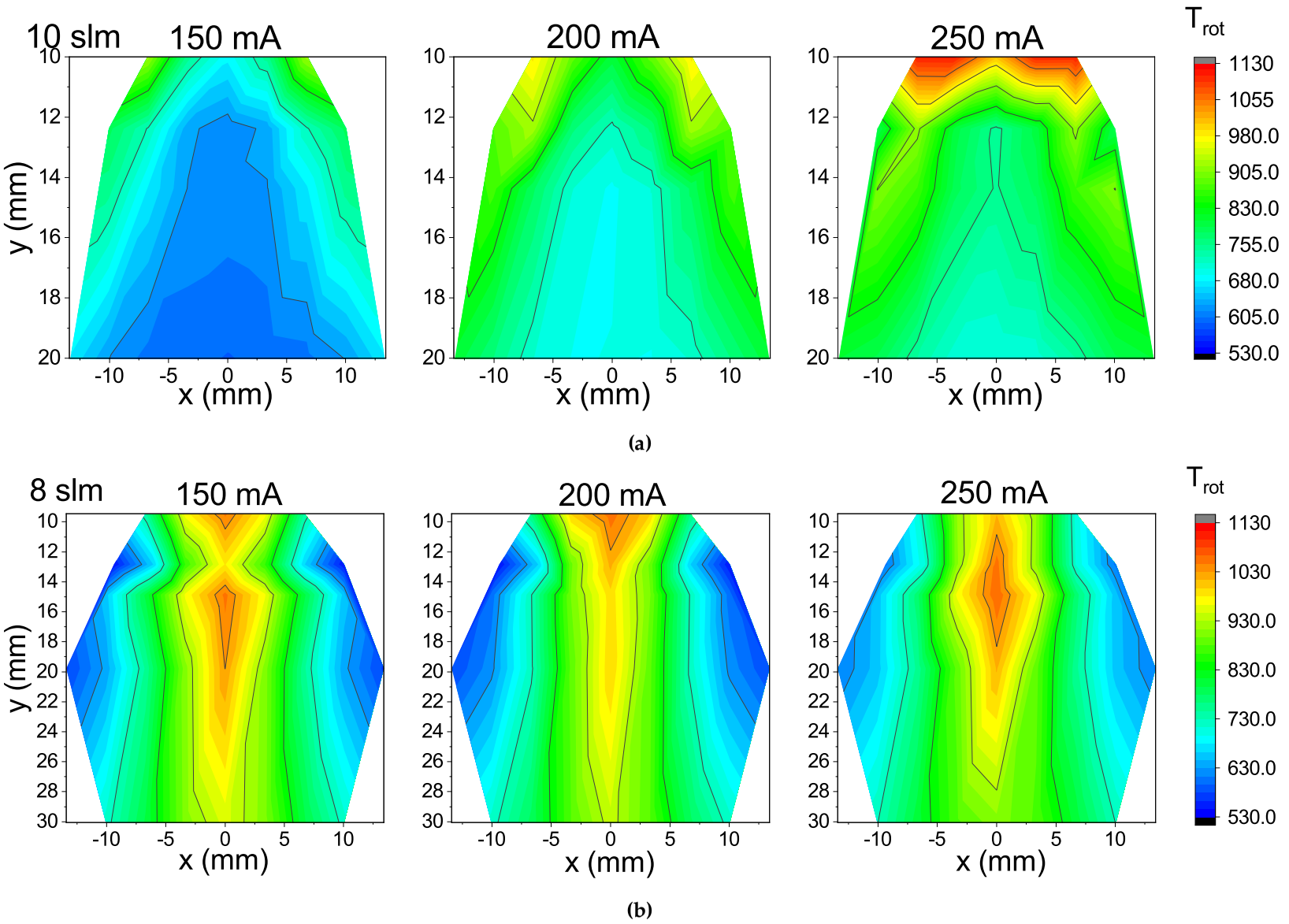

Figure 4.5: 2D vertical section of the T_{rot} distribution in the plasma afterglow at 10 slm (a) and 8 slm (b) with currents of either 150 mA, 200 mA or 250 mA.

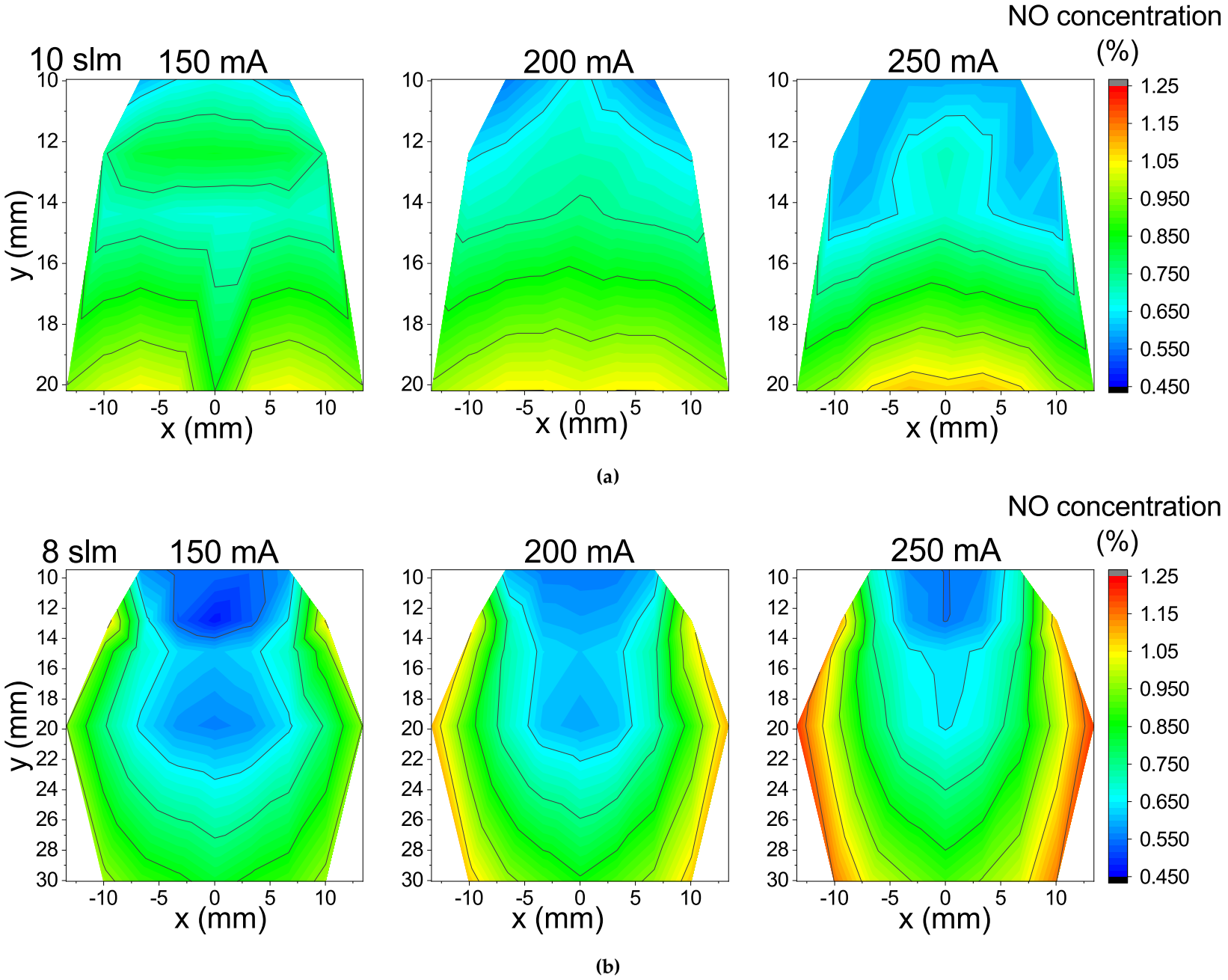

Figure 4.6: 2D vertical section of the NO(X) concentration distribution in the in the plasma afterglow at 10 slm (a) and 8 slm (b) with currents of either 150 mA, 200 mA or 250 mA.

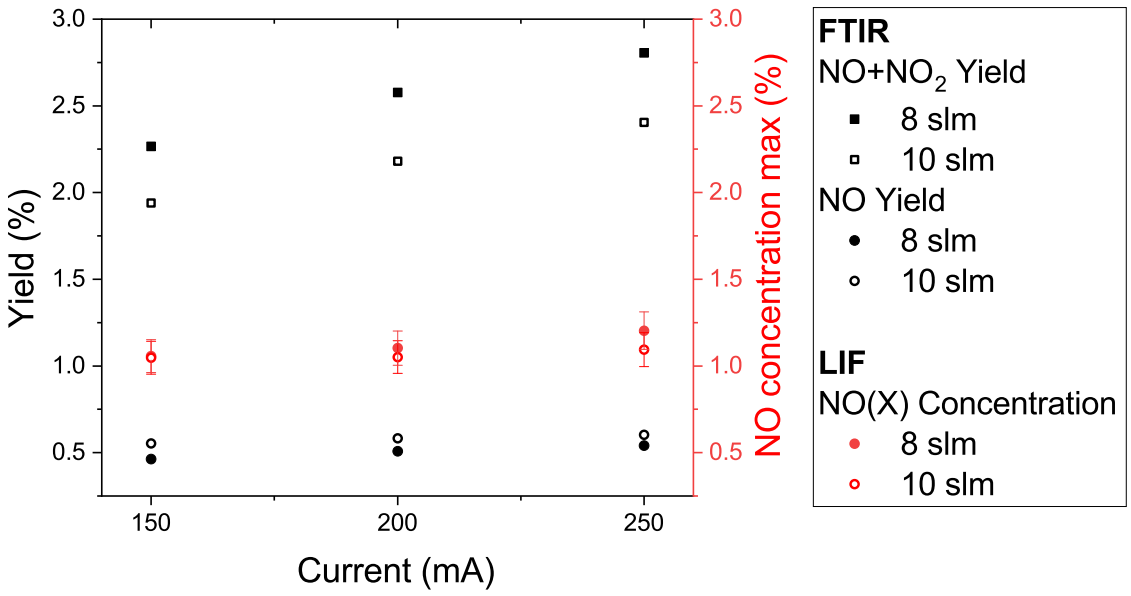

Figure 4.7: Maximum values for the LIF-measured NO(X) concentration in the afterglow (red, right y-axis) compared with the FTIR-measured yields (black, left y-axis) as a function of the current for 8 slm and 10 slm.

Finally, the difference in NO and NO_2 yields measured with 8 and 10 slm is mostly associated with a higher specific energy input (SEI), defined as [100]

$$\text{SEI} = \frac{P_P}{\text{gas flow rate} \cdot (1/22.4)(\text{mol/L})}, \tag{4.12}$$

where P_P is the plasma power. This can be observed in figure 4.8 where the NO and NO_2 yields measured at 8 slm and 10 slm show a similar dependency on the SEI.

4.4 Gas temperature cooling

As mentioned in the state-of-the-art discussion in Chapter 2, a few works have highlighted the critical role of T_{gas} quenching on the reaction chemistry [41, 52, 90] preventing the newly formed NO_x molecules to undergo the reverse Zeldovich reaction and decompose back to N_2 and O_2. Therefore, the LIF-based method for temperature determination was used to study the effect of an external cooling system on the GAP performance and to understand how both T_{gas} and the plasma power can affect the NO and NO_2 concentrations, and the NO selectivity, defined as in equation (3.7). In this section, cooling is performed via a 20 cm diameter industrial fan and the temperature on the walls is monitored through two thermocouples, located at, approximately, 1 cm (T_1) and at 18 cm (T_2) from the GAP anode as schematized in figure 4.9.

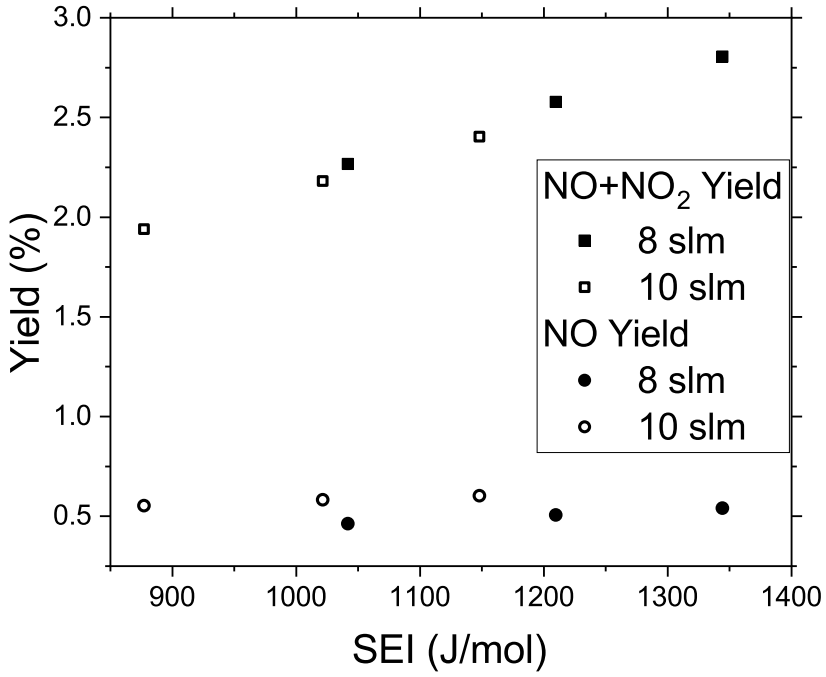

Figure 4.8: FTIR-measured yields as a function of the specific energy input (SEI) for 8 slm and 10 slm.

Two different configurations for the cooling system were tested and are compared. The results obtained in each configuration are labeled according to the air cooling system: "no cooling" if turned off, and "normal cooling" if the industrial cooling fan cools the cathode and the top 10 cm

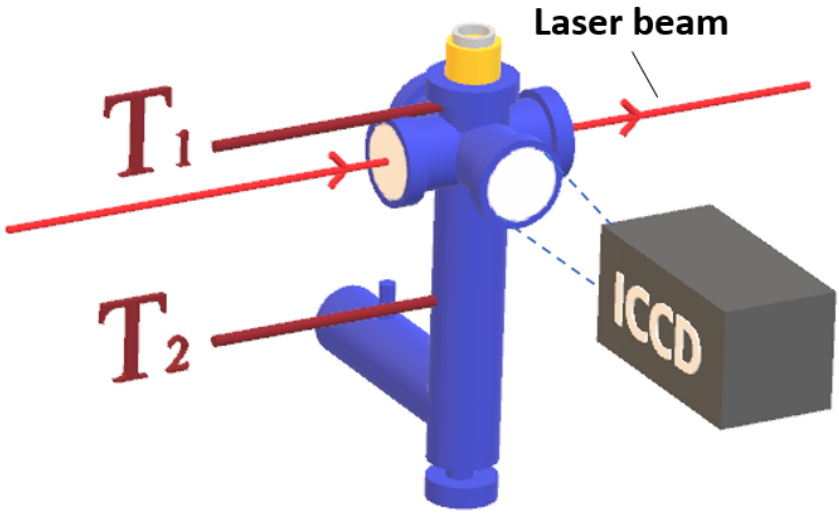

Figure 4.9: Scheme of the position of the thermocouples on the GAP.

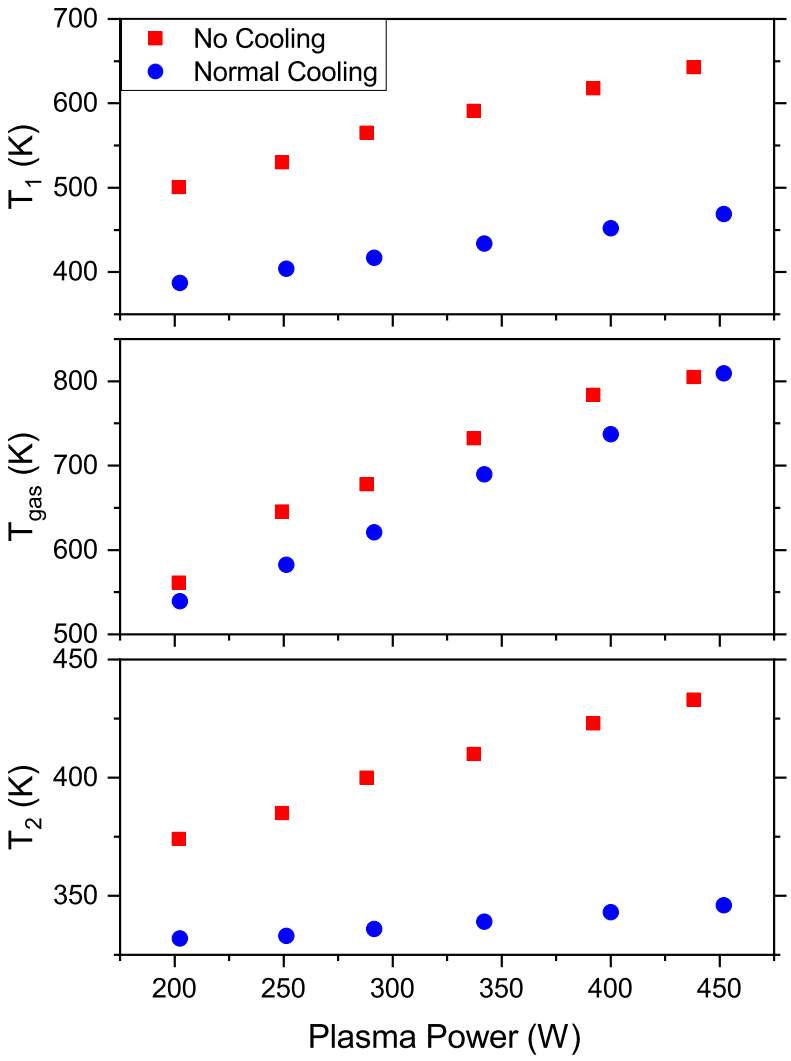

Figure 4.10: Wall (T_1 and T_2) and gas (T_{gas}) temperatures evolution as a function of the plasma power for the different cooling setups.

of the stainless steel tube connected to the GAP's anode. For each of the configurations, the temperatures on the wall (T_1 and T_2) and the T_{gas}, measured as discussed in section 4.2.1, are reported in figure 4.10. The input N_2-O_2 gas flow rate was set at 10 slm and T_{gas} was measured at the center of the exhaust tube at 15 mm from the anode

Lowering the temperature of the wall influences the heat transfer between the gas and the walls affecting the T_{gas} in the plasma, especially close to the discharge region, up to approximately 170 K. This allows the plasma to dissipate more heat on the walls, which can be observed by the T_{gas} measurements.

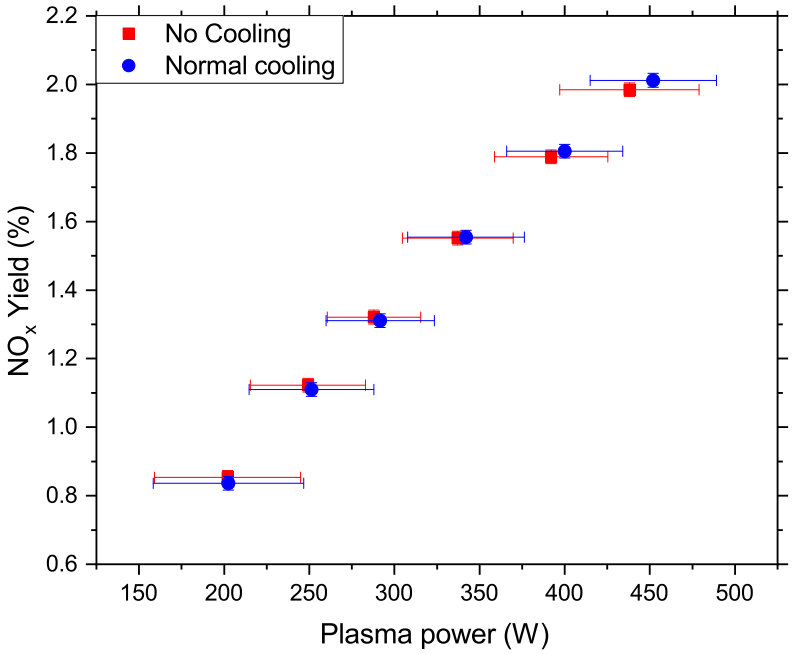

Figure 4.11: NO_x yield as a function of the plasma power for two different sets.

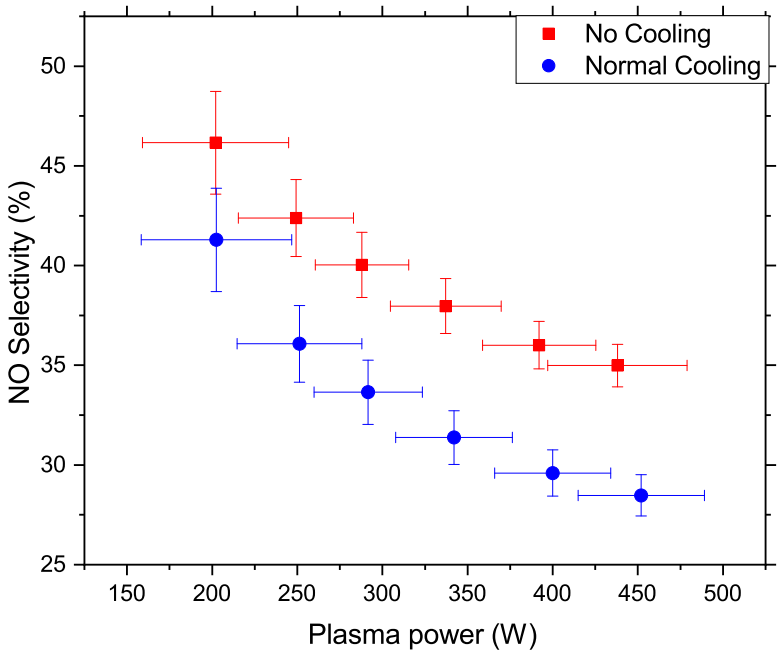

Figure 4.12: NO selectivity as a function of the plasma power for two different sets.

Figures 4.11 and 4.12 show the behavior of the total yield and of the NO selectivity respectively as a function of plasma power for the two configurations. For both cooling conditions, the total yield shows a linear dependency on the plasma power, which is consistent with what is described more in detail in section 5.3. While the total yields measured, taking into account the error bars, are comparable within the different sets, the measurements of the NO selectivity show that the NO_2 production tends to be favored as the cooling is applied. Additionally, increasing the plasma power also favors the production of NO_2 as the NO selectivity is observed to decrease by approximately 10 % in the range between 200 W and 450 W.

Considering the design of a GAP, an external cooling fan might not be effective to quickly quench the region between the two electrodes, thus explaining why a comparable NO_x yield is observed between the two cases. However, its effects are visible in the afterglow region, affecting the NO selectivity. As mentioned in section 2.3, as the gas cools down, the "slower" oxidation pathway (2.11) ($2NO + O_2 \rightarrow 2NO_2$) is reported to become dominant. While the gas mixture is not expected to fully reach equilibrium in the gas cell in the FTIR, the equilibrium constant for reaction (2.12) ($NO + O \rightarrow NO_2$) favors the formation of NO_2 at lower T_{gas} [90], thus, possibly explaining the trend observed in figure 4.12. Finally, the NO selectivity is observed to increase as more plasma power is applied. This is an expected effect since, as the power increases, more atomic O is expected to form in the discharge region [101], thus favoring the initial formation of NO_2 through reaction (2.12).

4.5 Conclusions

This chapter proposes a novel method for the determination of the NO(X, $v = 0$) rotational temperature T_{rot} based on the line ratio between the $J = 33.5$ and the $J = 21.5$ LIF peaks, which is compatible with atmospheric plasmas where a high absorbance can prevent the use of more well-established methods. The $J_{33.5}/J_{21.5}$ line ratio is studied with LIFBASE and shown to be a monotonic function of T_{rot}. Such a method is then applied to study the afterglow of a gliding arc plasma operating at atmospheric pressure with N_2 and O_2 a few mm below the anode (i.e., the reactor outlet). The T_{rot} measured with such method are then used to determine, using the $J = 21.5$ LIF peak, the NO(X) concentration, measuring up to 1.2 % NO.

The NO(X) concentration measurements performed with LIF in the plasma afterglow are compared with the NO and NO_x yields detected at the exhaust with an FTIR. For each of the experimental conditions, the maximum LIF-measured concentration is observed to be (i) higher that the NO yield, which is expected taking into account the NO losses due to the conversion into NO_2 and the back Zeldovich reaction, and (ii) lower than the NO_x yield, which, taking into account that only NO in the electronic ground state is observed, suggests that the conversion into NO_2 is already significant in the plasma afterglow region.

The obtained 2D spatial evolution of T_{rot} and of the NO(X) concentration highlights the NO(X)

concentration being higher as T_{rot} decreases. The input gas flow rate is found to be a crucial parameter affecting the temperature gradients in the plasma afterglow region, which likely happens as a result of changes in the plasma shapes. This is particularly important as a fast T_{rot} quenching is known to inhibit the NO Zeldovich back-reaction.

The LIF-based T_{rot} determination method is then used to study the effect of an external cooling system on the GAP performance. The NO_2 production is shown to be favored with a higher power as, for each of the sets, a decrease of approximately 10 % of the NO selectivity has been measured by increasing the plasma power from 200 W to 450 W. The NO conversion speed into NO_2 can, therefore be enhanced by tuning both the power and the cooling rate for the gas temperature in the afterglow region. This is a desirable effect as NO_2 is required to produce nitric acid HNO_3, a fundamental component in the ammonium nitrate fertilizer production chain.

Chapter 5

Electrical stability and performances

Having discussed the more fundamental aspects and given a possible industrial application of plasma-based NF, it is important to tackle the subjects of performance and process stability of a N_2-O_2 GAP. The latter is not often discussed in the literature despite being relevant as, often, to optimize the arc stability, important energy costs, which are not considered in the wider comparison between plasma-NF reactors, are introduced.

Therefore, in this chapter, the conventional approach of using external resistors and its repercussions on the GAP performance are discussed. More specifically, this chapter proposes a study of the electrical stability, NO_x yield, and energy cost of the GAP for different values of the external resistance. As an alternative approach, replacing the resistors with an external inductor is proposed and its effects are discussed.

The results related to this chapter are published in: F. Manaigo, A. Chatterjee, A. Bogaerts and R. Snyders, "New insight in NO synthesis in a gliding arc plasma via gas temperature and density mapping by laser-induced fluorescence", submitted (2024)

5.1 Introduction

In the literature, a lot of effort is dedicated to the optimization of the energy cost and the NO_x yield for plasma-based NF. Lowering the process energy cost is, in particular, crucial for any future industrial implementation of the technology (further discussion on this is provided in Chapter 6). In order to be up-scaled at an industrial level, it will still be necessary to also improve the electrical stability and the reproducibility of the technology. For this reason, studies on the electrical characterization have been performed on different GA designs [75, 102].

Nowadays, the conventional approach to stabilize this plasma process is to use external resistors [41, 51, 52, 103–106]. Although this indeed allows for an enhancement of the plasma stability, very little is reported about what the impact of those resistors, whose value can be up to a few tens of kΩ, is on the process efficiency, both in terms of NO_x yield and energy cost. Indeed, often, the reported values for the energy cost are calculated by considering the power directly injected in the plasma as an input value without an estimation of the loss of power into the resistors due to the Joule effect. As further discussed in this chapter, this is an important contribution to the overall energy cost of the reaction, which should be reported for any application-based discussion.

Therefore, in this chapter, a variable resistor is implemented in series with the DC power supply to stabilize the plasma. Both the performance and the stability of the plasma are reported as a function of the resistance R, which could be set to assume equivalent resistance values between 1 kΩ and 19 kΩ. In a second step and because of the obtained results, as an alternative solution, it is demonstrated that the replacement of the resistor by an inductor ($L = 100$ mH) is promising since it allows to decently stabilize the plasma while it does not affect either the energy cost of the process or the NO_x yield. Again, a complete characterization of the stabilization efficiency but also of the process performance in terms of NO_x yield and energy cost has been realized. This approach is found to offer several advantages, most notably, (i) a lower energy cost is associated with the overall process whereas the use of a resistor, in certain condition, is reported to increase the energy cost by almost a factor of 3, and (ii) the possibility of operating the GAP with higher plasma powers, which is an important step toward the upscaling of the technology.

5.2 Electrical characterization

In this configuration, as only the internal resistance of the power supply is limiting the current provided, arcing occurs, however, due to the high current and voltage fluctuations, the arc extinguishes before it can be extended. This rapidly results in the electrodes being damaged. When adding such elements to the electrical circuit, the plasma can be sustained. As an example, figure 5.1 shows, for $R = 19k\Omega$, the evolution of the time-resolved signal of the cathode voltage ($V_C(t)$) and the arc current ($I(t)$) for two values of the mean arc current (I) in the GAP. The signal oscillation from the DC components of $V_C(t)$ and $I(t)$ is shown both in terms of absolute and relative variations. $V_C(t)$ (corresponding to the voltage difference between the electrodes as the anode is grounded) describes the length of the arc as a function of time [75]. With a constant input gas

flow rate, the fluctuations of $V_C(t)$ decrease as I is increased, moving to a so-called "steady" state. This is in agreement with the characteristic behavior reported and studied for a GAP [75]. Despite the difference in the I range used for the measurements with R and L not allowing for a direct comparison, a milder effect is observed with L, as shown in figure 5.2, where the relative variations of $V_C(t)$ and $I(t)$ are comparable for the two values of I and are, overall, stronger than what was observed with the resistance at I equal to 200 mA. The difference in the timescales should be noted.

It is important to mention that without a resistor or an inductor, it is not possible to sustain the plasma in the studied conditions because the discharge is too unstable. In this configuration, arcing occurs, however, due to the high current and voltage fluctuations, the arc extinguishes before it can be extended. This rapidly results in the electrodes being damaged. When adding such elements to the electrical circuit, the plasma can be sustained. As discussed in detail by Fridman et al. [45], for an arc discharge to be stable, the differential resistance, defined as the derivative on I of the open circuit voltage (V_0) provided by the power supply of a resistive circuit (as is the case for the configuration in figure 3.1(a)), should be positive, as in the following equation [45]:

$$\frac{dV_0}{dI} = 2R - \frac{V_0}{I} > 0 \tag{5.1}$$

which is true if:

$$I > \frac{V_0}{2R} \tag{5.2}$$

as a consequence, a higher value of R allows the arc to be sustained at lower I.

In order to strictly evaluate the instability level as a function of the studied conditions in this work, the standard deviations associated to the mean cathode voltage V_C and the mean arc current I values measured on the oscilloscope signals, normalized by V_C and I, are considered representative of the instability level. As a consequence, a larger relative variation can be associated with a higher instability level of the system. Using this definition, it can be observed in figure 5.1 that the instability level decreases as I increases and that, overall, the use of resistors seems to better stabilize the plasma.

The power provided to the plasma P_P through the arc is evaluated as the integral over an arbitrary period of time t_0 of the product of $V_C(t)$ multiplied by the arc current $I(t)$.

$$P_P = \frac{\int_0^{t_0} V_C(t) I(t) dt}{t_0} \tag{5.3}$$

This has to be distinguished from the total power P_T provided by the power supply, which takes into account the dissipation through the Joule effect on the resistor R. With the assumption that

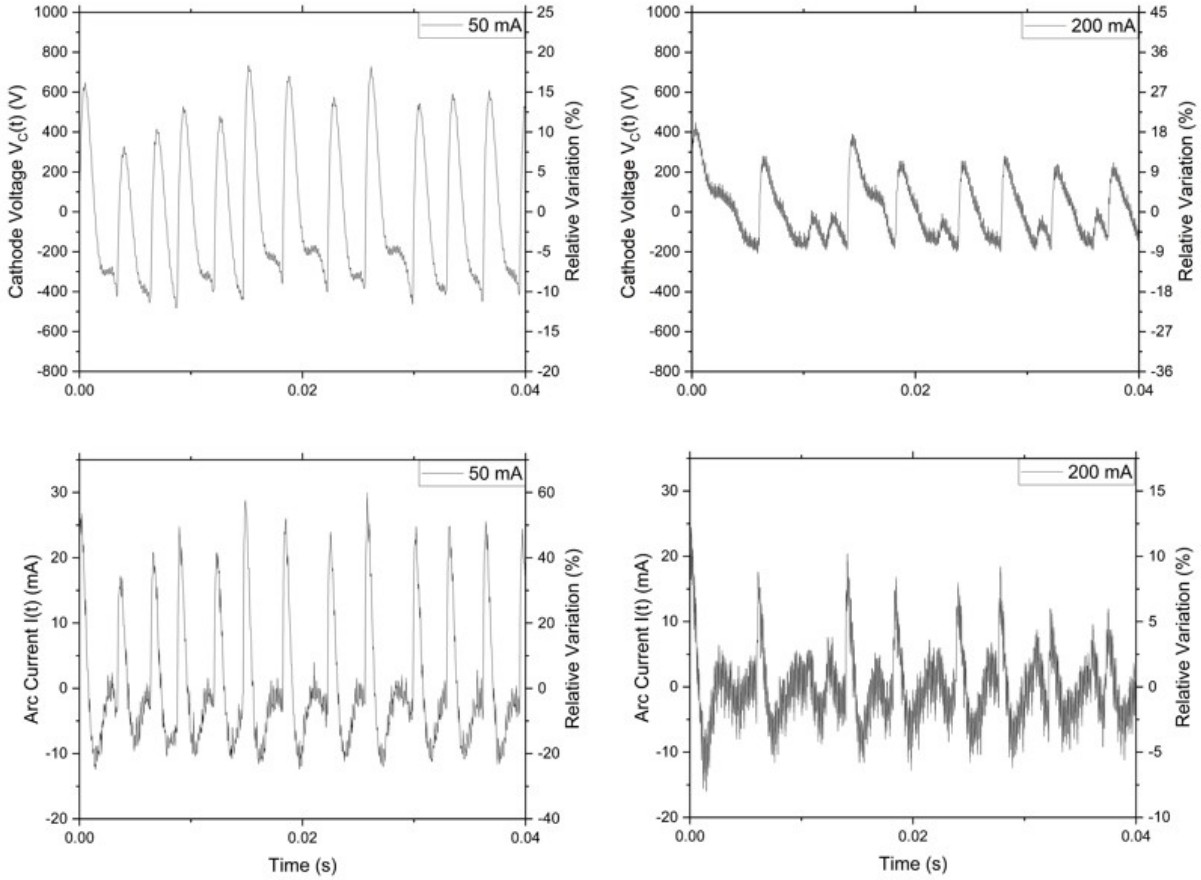

Figure 5.1: Temporal behavior of $V_C(t)$ (top) and $I(t)$ (bottom), where only the AC component is shown. R was set at 19 kΩ. The spectra were acquired with I equal to 50 mA (left) and 200 mA (right). The same curve also represents the relative variation, expressed as a percentage of the DC component of the signal, with the corresponding numbers given at the right y-axis.

the losses due to parasitic capacities and inductances are negligible, P_T can be evaluated with the following equation.

$$P_T = P_P + I^2 R \tag{5.4}$$

Different versions of bi-dimensional gliding arc discharges exist and have been studied in the past, focusing on the thermal stability of the arc itself [45]. Notably, it is reported that the power dissipated by the arc per unit of length plays an important role in defining the dynamics of the arc and its stability. Nevertheless, because of the specific geometry of the GAP, probing the region between the electrodes (where the arc develops) was not possible, making measurements of the arc length and radius or of the local gas temperature not possible.

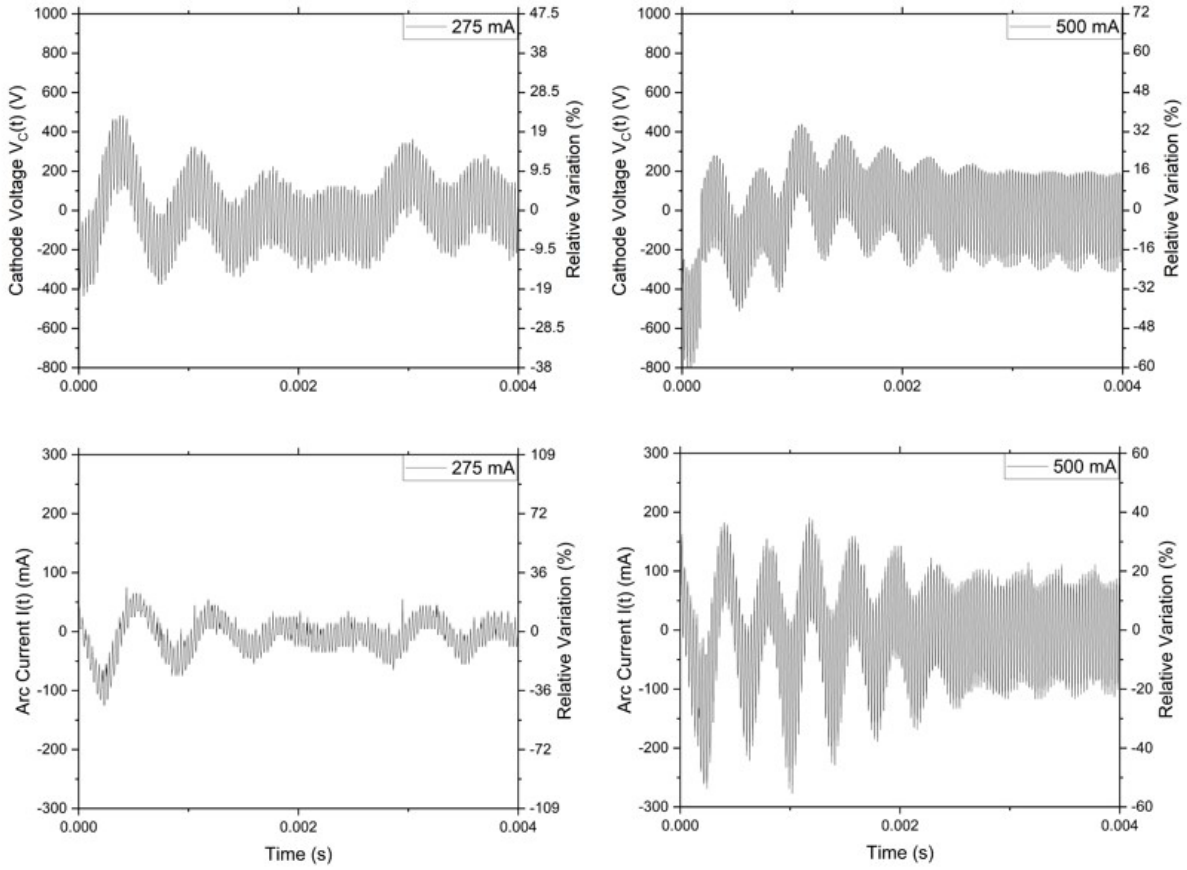

Figure 5.2: Temporal behavior of $V_C(t)$ (top) and $I(t)$ (bottom), where only the AC component is shown. L was set at 100 mH. The spectra were acquired with I of 275 mA (left) and 500 mA (right). The same curve also represents the relative variation, expressed as a percentage of the DC component of the signal, with the corresponding numbers given at the right y-axis.

5.3 Results and discussions

5.3.1 Resistor

Figure 5.3 shows, on the top, the typical voltage-current characteristics for an arc discharge, as discussed in section 2.5, and, on the bottom, the plasma power (P_P) as a function of I for two different values of R and for L. According to the Steenbeck channel model for the column of an arc discharge, P_P/l presents a weak dependency on the arc current I, described by the following equation [35] :

$$\frac{P_P}{l} = \frac{k_1}{(k_2 - \ln I)^2} \tag{5.5}$$

where k_1 and k_2 are constants, explaining both the trend observed for P_P in figure 5.3 and, considering equation 5.3 , for V_C in figure 5.3. It is observed that V_C as a function of I is not affected by R and thus, only the results corresponding to the two extreme values used ($R = 2k\Omega$)

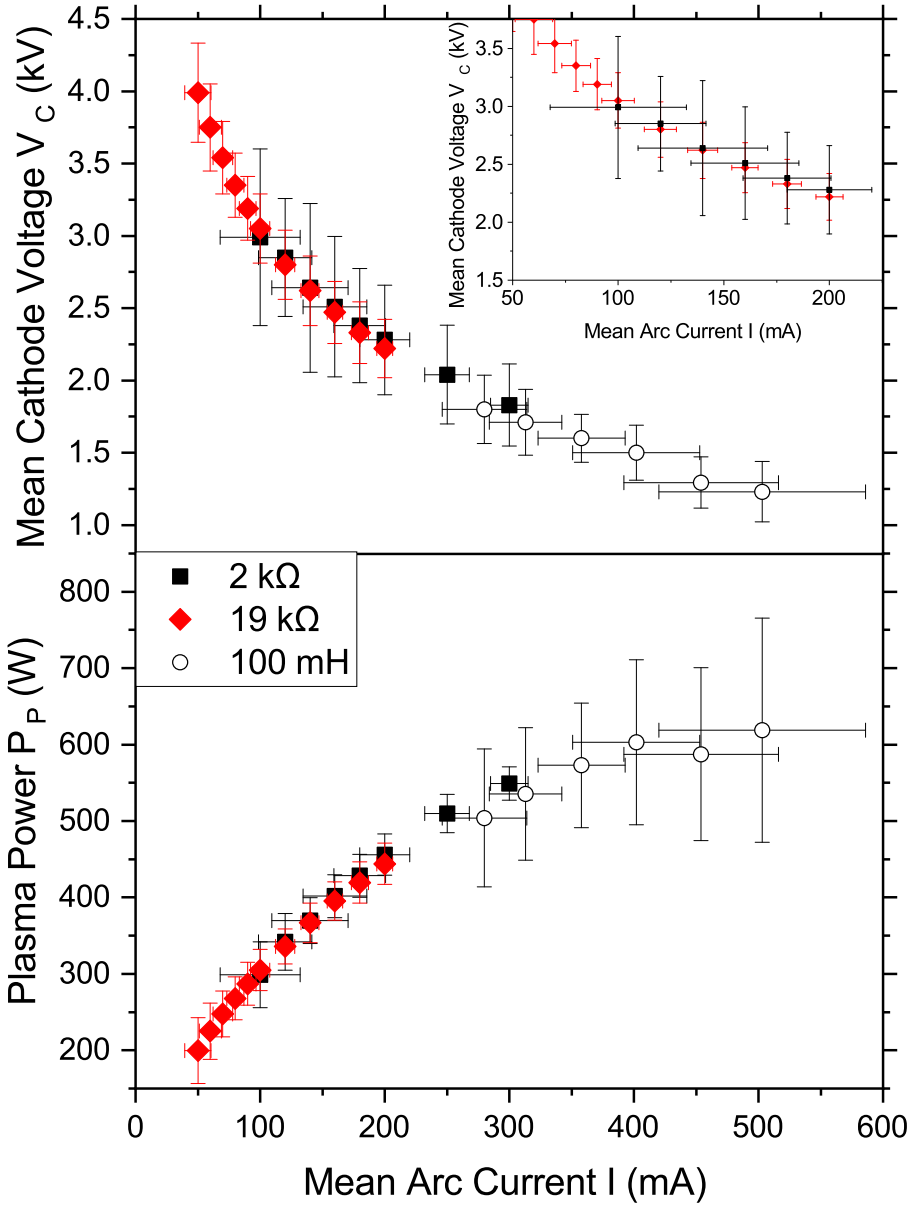

Figure 5.3: The mean cathode voltage (top) and the average P_P (bottom) as a function of the mean arc current I for two different values of R and for L.

and $R = 19k\Omega$) are shown. Likewise, the same behavior is observed for P_P. On average, it can be concluded that the arc elongation is not affected by any resistance in series with the reactor. The reported error bars correspond to the standard deviation measured for I and V_C based on the results shown in figure 5.1 and are, as explained, associated to the instability of the discharge.

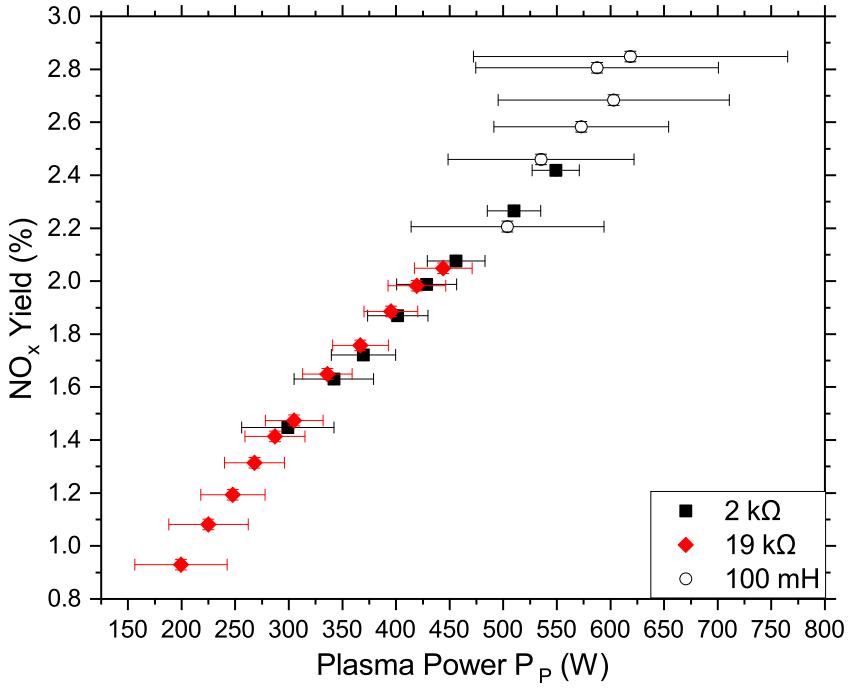

Figure 5.4: NO_x yield as a function of P_P. The yield linearly increases with the plasma power.

From the discussed results, it appears that for a given value of I, the instability decreases when increasing R. This highlights the importance of the resistance in order to improve the stability of the discharge by limiting the I fluctuations. A direct effect of increasing the arc stability through the value of R is that the plasma can be sustained using lower I and P_P when increasing R. In this work, for each value of R, the lowest applied values of I and P_P correspond to the minimum value that allowed the plasma to be sustained. The maximum I applied using R was instead limited by the power rating of the resistors. The R value could also be set to $1k\Omega$, however, with this configuration the plasma failed to ignite presenting a similar behavior as described at the beginning of section 5.2 in the absence of any resistor or inductor. These data confirm the previous reports revealing the efficiency of an external resistor in order to stabilize GAP discharges.

Concerning the effect of the resistor on the process in terms of yield and EC, the yield of NO_x (NO_2 and NO) as a function of P_P was measured for the two extreme values of R and is shown in figure 5.4. It is observed that the NO_x yield linearly increases with P_P, reaching a maximum of $2.08(2)$ % (R = 19 $k\Omega$) and $2.42(2)$ % (R = 2 $k\Omega$). The results are in line with the previous works reporting a linear dependency between the NO_x concentration and the specific energy input (i.e. P_P per liter of input gas) [107]. The yield is therefore found to be independent on the choice of R. As previously discussed, the value of R affects $I(t)$ and $V_C(t)$ fluctuations of the arc rather than their mean value. Thus, the specific energy input is, on average, not affected by the R value, explaining the obtained trend.

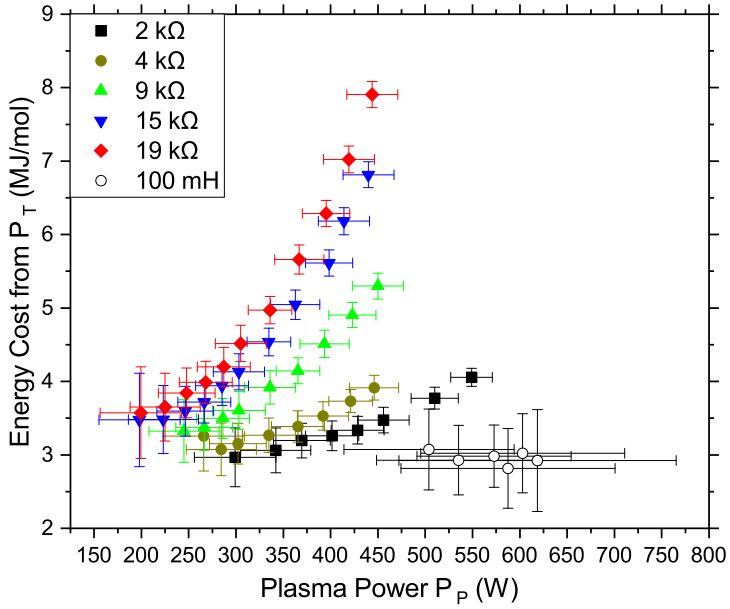

(a)

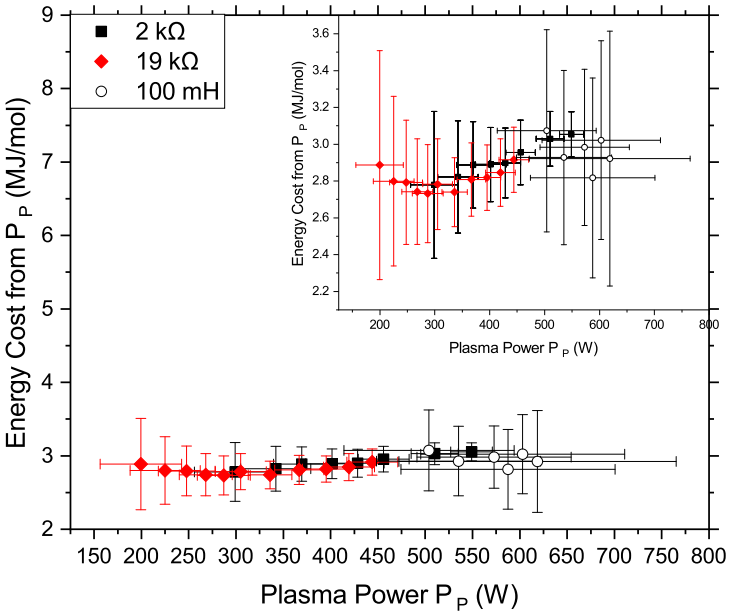

(b)

Figure 5.5: Evolution of EC as a function of P_P, when calculated based on (a) P_T, hence including the Joule dissipation by R, and (b) P_P, hence only due to the energy injected in the plasma. The latter is reported with two different scales and only two sets of points (i.e. $R = 2k\Omega$ and $R = 19k\Omega$) out of five are reported, to avoid excessive overlapping.

Figures 5.5(a) and 5.5(b) report the EC, evaluated according to equation 3.8, using as input power P_T (5.5(a)) and P_P (5.5(b)), respectively. Focusing on figure 5.5(b), considering the error bars, it is shown that increasing P_P does not significantly impact the EC. In this case, the average value of the EC evaluated from P_P is estimated to be 2.82(6) MJ/mol, close to the best reported results in literature [52, 53, 55]. On the other hand, when P_T is used to calculate the EC (figure 5.5(a)), a strong dependence of the EC as a function of P_P, which is strongly affected by R, is observed. Indeed the EC asymptotically increases with P_P, especially for high values of R for which, in the worst case, EC = 7.9(2) MJ/mol. The difference in EC between the two situations obviously originates from the power dissipated on the resistor by the Joule effect. In order to better visualize this effect, figure 5.6 shows the percentage of power effectively injected into the plasma as a function of P_P for different values of R. It clearly appears that for the worst conditions (R = 19 kΩ and Pp = 450 W), only 35 % of P_T is utilized by the plasma, while the rest is lost by the Joule effect. This clearly demonstrates that even if the utilization of an external resistor to stabilize the plasma is successful, the price to pay is a sometimes very strong decrease of the energy efficiency of the process when considering the applied power, which is indeed required for evaluating the industrial applicability.

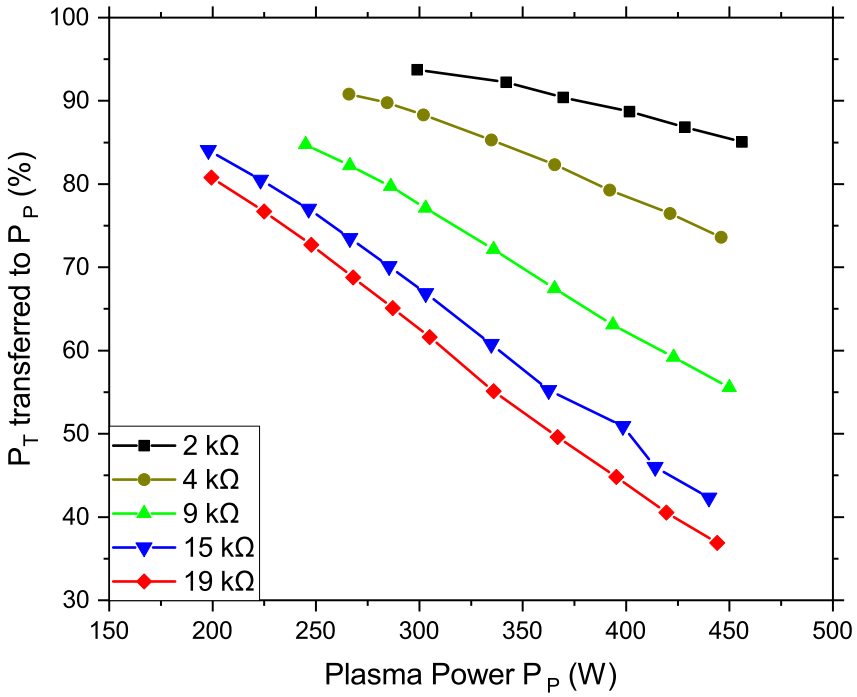

Figure 5.6: Fraction of P_T transferred to P_P, for different values of R, as a function of P_P. At higher R, a larger fraction of the power is lost through Joule heating.

5.3.2 Inductor

In order to avoid the loss in energy efficiency, this work suggests, as an alternative, the use of an inductor instead of external resistors. Therefore, it has been evaluated how this approach allows for a stabilization of the plasma and how it affects the process performance. In terms of plasma stabilization, a first observation is that it was not possible to ignite the plasma for I lower or equal to 250 mA because of the instabilities at low I. On the other hand, it can be observed in figures 5.3 and 5.4 that the results obtained when utilizing the inductor are consistent with the ones obtained in the conventional setup (utilizing R), but reveal bigger standard deviations on the I, V_C and therefore P_P values. In terms of relative instabilities, the measurements obtained with L show an average standard deviation of 12 % for I and of 13 % for V_C, which is comparable to what was observed for the measurements with R when the lower possible I was approached. It can therefore be concluded that the stabilization effect when utilizing the inductor approach is lower than when utilizing the external resistor. Nevertheless, this does not prevent the ignition of the plasma for electrical conditions that are compatible with industrial application (high current, high power i.e., higher than with the resistors). Overall a positive effect was observed on both NO_x yield (figure 5.4) and EC (figure 5.5). Indeed, figure 5.4 clearly shows a higher NO_x yield (up to 3%) when using an inductor, due to the higher P_P. Figure 5.5 illustrates that the EC based on P_P is only slightly higher (3 MJ/mol, again due to the higher P_P), but importantly, the EC based on P_T is also limited to this 3 MJ/mol, hence much lower than when using resistors, where the EC went up to 7.9 MJ/mol. This is very striking, and shows that, in combination with the clearly higher NO_x yield, using an inductor is really promising for industrial applications, where the EC based on the total power should be considered.

5.4 Conclusions

This chapter discussed the impact of passive electric components used to stabilise a GAP discharge on the stability level and on the process performance (NO_x yield and EC). Resistors are the dominant choice in literature, as they enhance the stability of the arc discharge by limiting the fluctuations of the arc itself. However, the impact on the overall EC due to external resistors should not be neglected since, as reported, it can dramatically increase the total power consumption of the system. The GAP presented in this work achieved a lowest energy cost, based on the energy provided to the plasma (P_P), of 2.82(6) MJ/mol, which is quite close to the most recent best results in literature, i.e., 2.1-2.5 MJ/mol for a RGA [51, 52], 2.0 MJ/mol for atmospheric pressure MW plasma [55], and 1.8 MJ/mol for an enhanced pressure RGA [53]. However, after considering the power lost due to Joule dissipation, this translates to an overall energy cost up to 7.9 MJ/mol according to the choice of the resistance. It has been demonstrated that replacing the resistor with an inductor also allows for a decent stabilization of the discharge and, most importantly, allows to avoid the loss of power through Joule dissipation. Both the passive electric components tested in this work generally seem to play a negligible role in the chemistry of the plasma. Both with the resistor and with the inductor, the NO_x yield showed a linear dependence with P_P, with a best

measured value of 2.85(2) % corresponding to the highest P_P. By increasing it further, higher NO_x yields could be achieved with little repercussions on the EC due to P_P alone if the highlighted trend is valid for higher P_P. Furthermore, when using an inductor, also the EC based on total (applied) power remains constant upon increasing power, being as low as 3 MJ/mol. This is in contrast to the case when using external resistors, where the EC based on total power rises with power. To conclude, this work strongly suggests that an inductor should be preferred for the discharge stabilization in order to achieve a competitive overall EC (i.e., based on applied power) for plasma NF with a GAP.

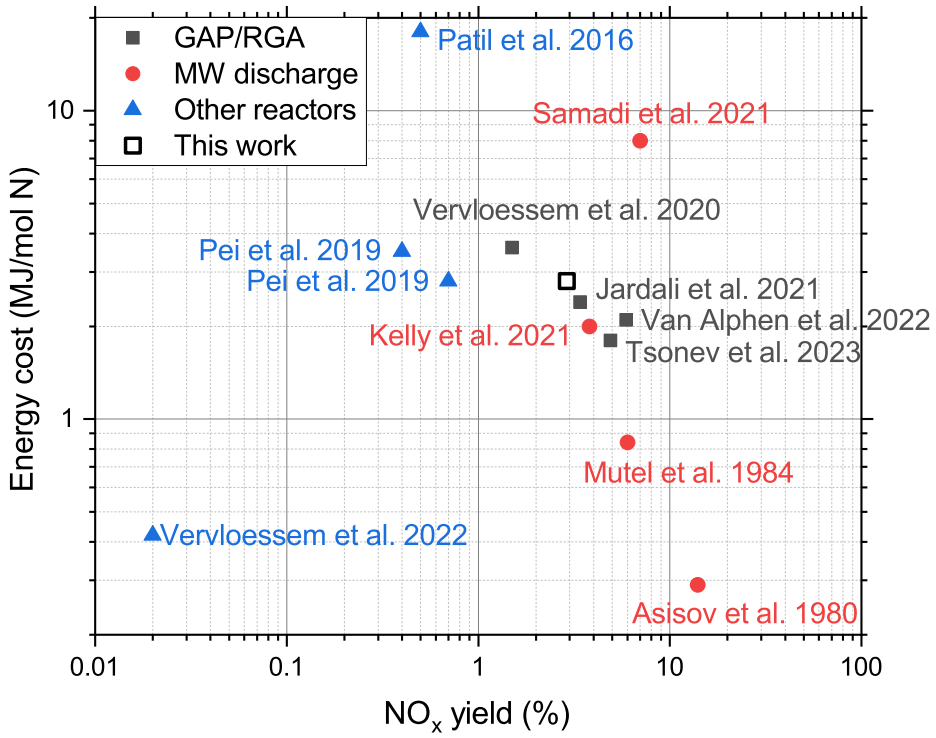

Figure 5.7: Comparison of the energy costs and NO_x yields for various plasma reactors. The data are based on table 2.1

Figure 5.7 graphically shows how the energy cost and NO_x yield obtained in this chapter compare with the values listed in table 2.1. Excluding the results reported by Asisov et al. [57] and by Mutel et al. [56], that have not been reproduced in recent years, in terms of energy cost and NO_x yield, there are better results in the literature compared to what is reported for the setup used for this thesis. Therefore, the following chapter, discussing about the industrial perspectives of plasma-based NF, is not based on the performance of the GAP used for this thesis.

Chapter 6

Feasibility study of a small-scale fertilizer production facility

To complete the given picture of plasma-based NF, an overall view of the industrial applicability of the technology is discussed. As one of the final goals, using the currently best available technology, the industrial applicability in the fertilizer manufacturing industry of plasma-based NF is studied.

Plasma-based NF is often presented as a technology that could be implemented at a small local scale. This chapter aims to verify this assumption by studying the economic feasibility of a small-scale nitrogen fertilizer facility that uses plasma-based technology and comparing it with the H-B process, both electrified and coupled with SMR. Capital expenditures, gas price, CO_2 allowances, levelized cost of energy, and transport costs are considered in this comparative model which is used to understand the impact of such parameters on the fertilizer production costs.

The results related to this chapter are published in: F. Manaigo, K. Rouwenhorst, A. Bogaerts and R. Snyders, "Feasibility study of a small-scale fertilizer production facility based on plasma nitrogen fixation", *Energy Convers. Manag.* in press (2024)

6.1 Introduction

As discussed in section 1.1, the nitrogen fertilizer production scene has been dominated by the H-B process for over a century despite being recognized to be environmentally impacting. While the lowest reported energy cost for the H-B process is 0.49 MJ/mol N [6, 31], the average performances of the technology correspond to an energy cost of 0.65 MJ/mol N and a CO_2 emission of 2.16 t per t of NH_3 [33]. As a reference, in 2019, a global production of 185 Mt of NH_3 was recorded and is associated with approximately 1% of the world energy consumption and 1% of the world total CO_2 emissions [31].

The typical fertilizer production facility covers all the steps from natural gas reformation to the synthesis of the final product. As its components greatly benefit from an economy of scale, in order to optimize the production costs, the process is currently performed in large-scale facilities [7, 23]. This has repercussions on the fertilizer supply chain. As the typical fertilizer production facility can supply up to approximately 100 000 km^2 of arable land, it is not uncommon for the final product to be shipped across distances of the order of 100-1000 km. As, with the current best available technology, the energy cost for plasma-based NF is too high to directly compete with the H-B process and due to the impact of the H-B-based technology in terms of CO_2 emissions, plasma-based technology is often presented as a technology that could be implemented at a small local scale together with renewable energy sources.

With a few exceptions [19, 23, 76, 77], the literature lacks in studies discussing the economic perspectives of plasma-based NF. Therefore, this chapter aims to offer a more general discussion of the current applicability of the technology from an economic point of view, using the current best available technology.

More specifically, this chapter presents a study on whether a hypothetical small-scale fertilizer production facility, producing NH_4NO_3 and based on a RGA, can be a local competitive alternative to a classical H-B and steam methane reforming-based facility. The hypothetical plasma-based alternative is then compared with a state-of-the-art H-B-based fertilizer facility. Capital expenditures, gas price, CO_2 allowances, levelized cost of energy, and transport costs are considered in this comparative model which is used to understand the impact of such parameters on the fertilizer production costs. As the energy cost for plasma-based NF is currently the main drawback to the industrial implementation of the technology, the energy cost requirement for a plasma-based facility to be an economically viable alternative in the upcoming years is studied as a function of the prices of energy and natural gas. Additional focus is put into understanding how transport costs and CO_2 emission allowances affect the results. As the comparison depends on many factors that can strongly vary with time, a sensitivity analysis is also presented to appreciate how the results can evolve due to different market conditions.

Finally, while water electrolysis is considered to meet the H_2 consumption of the studied plasma NF setup, a short comparison with the H_2 production costs based on methane plasma pyrolysis is provided in Appendix C.

6.2 Methodology

Production costs can be divided into two main categories, capital expenditures (CapEx) and operational expenditures (OpEx). The CapEx mainly includes the expenditures to engineer, construct, maintain or improve physical assets such as, for example, properties, plants and equipment (PPE costs) of any kind. These are usually "one-time" expenses and their effect on the production cost is normalized by the NH_4NO_3 annual production (P_a) and its depreciation period (d), i.e. the number of years the asset is estimated to be able to operate. In this chapter, the following definition of (annual) CapEx [108], expressed in euro per metric ton of NH_4NO_3 ($€/t_{NH_4NO_3}$), is used:

$$CapEx = \frac{\text{PPE costs}[€]}{d[y] \cdot P_a\left[\frac{t_{NH_4NO_3}}{y}\right]} \cdot (1 + r_p) + \frac{\text{M}\left[\frac{€}{y}\right]}{P_a\left[\frac{t_{NH_4NO_3}}{y}\right]} \tag{6.1}$$

where M is the annual maintenance cost and r_p is the project interest rate. For both the plasma-based and SMR-HB fertilizer production facilities, a depreciation period of 20 years is assumed. It should be noted that this definition, for the sake of simplicity, does not take into account permits or legal costs. The annual maintenance cost (M) is usually assumed to be between 2 % and 5 % of the replacement asset value (RAV). In this chapter an intermediate estimation of 3 % is used. Additionally, as the prices for the PPE costs reported in this chapter, mainly account for plants and equipment, for the estimation of the maintenance costs the RAV is assumed to be, approximately equal to the PPE costs reported. r_p is evaluated according to equation 6.2 [109]

$$r_p = \frac{r_c}{(1 - (1 + r_c)^{-d[y]})} \tag{6.2}$$

where r_c is the cost of capital, which includes the costs of equity and debt. The r_p is assumed to be a constant amount over an amount of years equal to d. In this chapter r_c = 9% is assumed [110], thus, resulting in an r_p of 11%.

Table 6.1: Market prices for gas and CO_2 allowances assumed in this chapter.

Parameter	unit	price	reference
Natural gas	€/MWh	47.08	Dutch TTF (01 mar 2023)
CO_2 allowances	$€/t_{CO_2}$	98.91	EU ETS (01 mar 2023)

The estimations of the PPE costs discussed in this chapter are based either on cost reports for existing chemical facilities or from other feasibility studies. The PPE costs are then scaled according to the annual production P_a according to equation 6.3 [108],

$$\frac{\text{PPE costs}}{(\text{PPE costs})_{ref}} = \left(\frac{P_a}{P_{a,ref}}\right)^c \tag{6.3}$$

Table 6.2: LCOE for photovoltaic electricity production in 2020 and the predictions for its evolution in 2030 and 2050.

Parameter	LCOE (€/MWh)	reference
PV (2020)	51	[111, 112]
PV (2030 prediction)	27	[111]
PV (2050 prediction)	19	[111]

where, the subscript ref indicates the reference values and c is the scaling exponent which depends on the type of chemical facility [108]. This chapter uses the values reported by Peters et al. [108] of 0.6 and 0.65 for the HNO_3 and NH_4NO_3 facilities, respectively. As for the NH_3 production step $P_a = P_{a,ref}$, equation (6.3) was not used in that case.

The OpEx includes the expenses for consumable goods. This chapter mainly focuses on electricity, natural gas and CO_2 emission allowances prices. The natural gas price is taken from the Dutch TTF index and expressed in €/MWh. The CO_2 emission allowances price considered is the current market price for a ton of CO_2 in the EU emission trading system (EU ETS). Table 6.1 summarizes the prices which are assumed in this chapter. As for electricity, the prices in European markets (EPEX, IPEX, OMIE) are generally higher and much more volatile than the reported energy production cost from renewable sources. Thus, this chapter considers the levelized cost of energy (LCOE) for photovoltaic plants (PV) as discussed and studied in an article by Sens et al. [111]. Among other renewable energy sources, on-shore and off-shore wind power generation are not included in the model as they are associated with a higher LCOE prediction for 2050 [111]. The LCOE is defined as the sum of costs over the power plant lifetime normalized by the energy produced in the same timeframe. The values reported in the study are shown in table 6.2. Especially for small and localized producers, this approximation offers a baseline for the evaluation of the energy cost. Its accuracy is influenced by the degree of electric self-sufficiency and the contract agreements on selling the energy in excess during the daytime, when PV production peaks, to the grid and buying it during nighttime. It should be noted that the PV LCOE should be intended as a reference on the minimum LCOE that is currently predicted for 2022. For this reason, the cost comparison discussed in section 6.5 treats the LCOE as a variable parameter. Additional entries that would affect the OpEx, such as salaries, are not included in the model.

6.3 Plasma nitrogen fixation setup

To synthesize NH_4NO_3, both HNO_3 and NH_3 are required. This chapter considers plasma NF to NO_x as the first step for the production of both chemicals. The use of an RGA operating at atmospheric pressure is considered with an energy cost of 2.1 MJ/mol [52]. Such a system was tested with an input gas flow rate ranging from 1 slm to 10 slm and provided NO_x concentrations up to 5.9 % when set at 2 slm. Two lower energy cost values were reported for plasma-based NF, as mentioned in the introduction, however, to simplify the CapEx evaluation, this chapter focuses

on atmospheric pressure plasmas and chooses an RGA as it has a simpler and cheaper design. Nevertheless, in later sections, a range of energy costs is discussed to evaluate the, more general, requirements for plasma-based NF technology. Half of the produced NO_x would follow a similar process to what has been discussed for SMR-HB facilities: the NO is further oxidized to NO_2 as described in equation 1.7 and then absorbed in an absorption column with a water sprayer to form HNO_3 according to equation 1.8. As for the plasma NH_3 synthesis, this chapter considers a setup proposed and tested by Hollevoet et al. in 2020 [65] and in 2022 [66], respectively, which is schematized in figure 3.2.

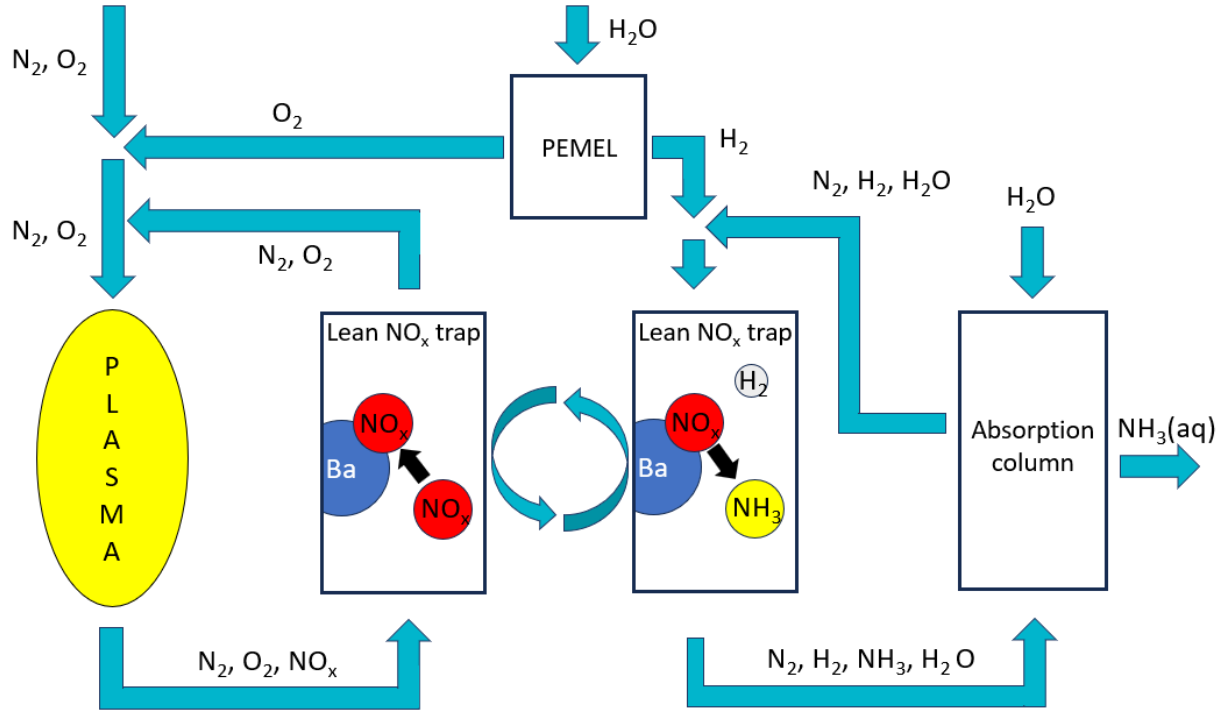

Figure 6.1: Scheme of the plasma-based production chain for the synthesis of NO_x and NH_3, from the polymer exchange membrane electrolyzers (PEMEL) to the absorption column, readapted from [65, 66].

The RGA plasma exhaust is connected to a lean NO_x trap where the produced NO_x contained in the gas mixture is absorbed. The lean NO_x trap is then fed with H_2 in N_2 carrier gas for the trapped NO_x to be reduced to NH_3. A $Pt/BaO/Al_2O_3$ catalyst can be used in the lean NO_x trap to favor the reduction to NH_3 [113].

$$3NO_2 + BaO \rightarrow Ba(NO_3)_2 + NO \tag{6.4}$$

$$Ba(NO_3)_2 + 5H_2 \rightarrow BaO + N_2 + 5H_2O \tag{6.5}$$

$$Ba(NO_3)_2 + 8H_2 \rightarrow BaO + 2NH_3 + 5H_2O \tag{6.6}$$

Where, according to the choice of the $Pt/BaO/Al_2O_3$ catalyst, the selectivity towards NH_3 can

vary between 75% and 87%. However, as part of the H_2 is lost in H_2O, 4.6 mol H_2 are needed to produce 1 mol NH_3 [65]. Switching between a series of lean NO_x traps is proposed in order to allow the system to operate continuously. The produced NH_3 can then be extracted as an aqueous solution in a spray column. Finally, HNO_3 and NH_3 would combine to form NH_4NO_3 following the same process used for SMR-HB facilities. In this chapter, water electrolysis is assumed to be used for H_2 production. The O_2 obtained as a byproduct can be used, together with air, as the gas feed input for the RGA because O_2-enriched air typically increases NO_x yields and lowers the energy cost [41, 42, 51, 52, 55].

The paper in which this setup is first proposed reports an energy cost of 4.61 MJ/mol NH_3, four times lower than the current best available technology for direct plasma-catalytic NH_3 synthesis [65]. This result can be lowered to 3.9 MJ/mol NH_3 if the use of a better performing RGA is assumed [52] and by including polymer exchange membrane electrolyzers (PEMEL) with 70 % efficiency. In terms of the final product, this would translate in 20.9 MWh/$t_{NH_4NO_3}$, of which 6.25 MWh are required for H_2 production and 14.6 MWh for NF. Further tests have been performed using a Soft Jet plasma [66] obtaining the lowest energy cost of 2.1 MJ/mol NH_3. However, such a result is currently limited by the relatively low NO_x concentration and input gas flow rate, 0.12 % NO_x and 0.2 L/m respectively. Thus, this result was not considered for this analysis due to concerns about its compatibility with high-scale production.

Finally, the energy costs associated to the production of HNO_3 and NH_4NO_3 are estimated, according to different reports [32, 114], to be of the order of a few tens of kWh/$t_{NH_4NO_3}$ and are, thus, neglected.

6.4 Cost evaluation

6.4.1 SMR-HB facility

Table 6.3: Summary of the NH_4NO_3 production costs for a SMR-HB facility.

name	price (€/$t_{NH_4NO_3}$)	references
CapEx (d = 20 years)	137	[31, 115]
Natural gas	160	[6, 31]
CO_2 allowances	111	[31, 33]

This chapter considers as a reference for comparison a SMR-HB facility with a P_a of 2000 kt/year of NH_4NO_3, which corresponds to an NH_3 annual production of 850 kt/year. The price for the SMR and the NH_3 plants, according to evaluations from IEA's ammonia technology roadmap [31], can be estimated to be 1570 million €, which can increase by 380 million € if a CCS system is included. The price for building the HNO_3 and the NH_4NO_3 plants is evaluated to be 1150 million €. Such an estimation is based on the reported upgrade costs for two existing facilities [115, 116] which have been adjusted for inflation and have been rescaled to meet the reference quota using

equation 6.3. These contributions sum to 3100 million €, thus, using equation 6.1 the CapEx is estimated to be 131 €/$t_{NH_4NO_3}$.

The main contributor to the OpEx is natural gas as 0.49 MJ/*mol* N are currently required [6, 31]. Natural gas is used both as a feedstock for the SMR process and as a fuel for the facility. This translates into 3.4 MWh/$t_{NH_4NO_3}$ which, taking into account the price for natural gas, results in an OpEx contribution of 160 €/$t_{NH_4NO_3}$. Additional costs come from the CO_2, which is mainly emitted during the SMR process. Assuming a CCS system is implemented to reduce the CO_2 emissions, the estimation of the average CO_2 emissions per ton of NH_4NO_3 is 1.12 t according to the GREET 2021 database [33] which corresponds to an OpEx contribution of 111 €/$t_{NH_4NO_3}$ according to the EU ETS allowances price.

6.4.2 Plasma-based NF facility

Table 6.4: Summary of the NH_4NO_3 production costs for a plasma NF-based facility discussed in this chapter. The electricity expenses are based on the LCOE for PV listed in table 6.2.

name	price (€/$t_{NH_4NO_3}$)	references
CapEx (d = 20 years)	288-342	[19, 23, 115–118]
Electricity (PV_{2020} prediction)	1060	[52, 65]
(PV_{2030} prediction)	560	[52, 65]
(PV_{2050} prediction)	395	[52, 65]

In this chapter, a plasma-based facility with the setup discussed in section 6.3 is proposed. As previously stated, a hypothetical plasma-based fertilizer production facility would not require the upscaling needed for the typical SMR-HB plant to be economically advantageous. This, combined with the generally higher requirements in terms of energy, pushes for plasma alternatives to be more interesting on a small scale. Therefore a P_a of 8000 t/year of NH_4NO_3 is used as reference. This quota would sustain between 30 and 100 km^2 of arable land. Considering that the average farm in the EU has an area of 0.17 km^2 [119], this would correspond to 180-600 average-sized farms. Such a reference quota was arbitrarily chosen as it would supply an area considered "local" by the authors. Based on the molar weights, such an amount would require 1700 t/year of NH_3 and 6300 t/year of HNO_3. As previously mentioned, 4.6 mol H_2 are required to produce 1 mol NH_3 [65] since, during the NO reduction to NH_3, part of the H_2 is lost due to conversion in H_2O as shown in equations 6.5 and 6.6. In order to meet the production quota, 920 t/year of H_2 should be produced through water electrolysis. Using the higher heating value for H_2 (HHV = 142 MJ/kg) and assuming a production efficiency $\epsilon = 70\%$, a 5.9 MW electrolysis plant is required to meet the quota based on the following equation [120].

$$P[MW] = \frac{P_a(\mathrm{H_2})\left[\frac{t_{H_2}}{y}\right] \cdot HHV_{\mathrm{H_2}}\left[\frac{MJ}{kg}\right]}{\epsilon} \frac{1000}{365 \cdot 24 \cdot 3600} \tag{6.7}$$

where P is the power required and $P_a(H_2)$ is the H_2 production quota of H_2. If the use of PEMELs is assumed, the production price can be expected to be around 800 €/kW [117], resulting in a total price of 4.7 million €. This price per unit of power is based on a recent study by Reksten et al. [117] which analyses and models the price dependency of different water electrolyzer technologies as a function of the annual production and of the year of commission. As for the RGA, the main contribution to the CapEx comes from the power supply. Considering the scale of the facility, a wide price range between 0.9 €/W and 0.05 €/W is often assumed [23, 121]. However, the lowest reported price for a power supply was found to be 0.2 €/W for a 1 GW power supply [122]. The described facility would require 9200 t of NO_2 to be produced yearly, which corresponds to 2×10^8 mol N each year. Assuming the plant to be operational throughout the year and an energy consumption of 2.1 MJ/mol N, an average power of 13.3 MW is required. Considering the scale, a price of 0.4 €/W is assumed, resulting in 5.3 million € as the cost estimation for such power supply. As the cost of power supplies is an important component of the CapEx, it becomes clear how reducing energy cost for NF is crucial, not only to lower the OpEx but the CapEx as well, because a lower power supply would be required to meet the same quota. Finally, a small-sized plant for the synthesis of HNO_3 and NH_4NO_3 would be required. As the reports for a plant with an annual production close to the target quota are not available, the estimation is based on the downscaling, using equation 6.3, of facilities with an annual production which is of 3-4 orders of magnitude higher [115, 116] and, as such, might suffer from an overestimation. Additionally, as the plasma-based NF facility proposed would directly produce NO_2, the Oswald process, which is one of the two processes normally covered in an HNO_3 plant, is not necessary. From these considerations, a cost range between 17 and 22 million € is assumed. The costs for the RGA structure and the lean NO_x trap are assumed to be negligible compared to the other prices listed. The sum of these contributions, which are summarized in table 6.5, give a PPE cost of 28.6-31.6 million € Using equation 6.1 a CapEx between 288 €/$t_{NH_4NO_3}$ and 342 €/$t_{NH_4NO_3}$ is estimated.

Table 6.5: Summary of the PPE costs for the plasma NF-based facility discussed in this chapter.

name	PPE cost (million €)	references
Power supply	5.3	[23, 121, 122]
PEMEL	4.7	[117]
NH_4NO_3 plant	17-22	[115, 116]

As listed at the end of section 6.3, the main contribution for the OpEx is electricity as, per ton of NH_4NO_3, 6.25 MWh are required for H_2 production and 14.6 MWh for NF. The OpEx is evaluated as the energy cost per ton of NH_4NO_3 times the LCOE. Therefore, the LCOE is of primary importance for the determination of the OpEx. If the photovoltaic generation LCOE in 2020 shown in table 6.2 is assumed, the OpEx would be approximately 1060 €/$t_{NH_4NO_3}$ which, alone, would not make plasma-based NF an interesting option in 2020 with the current performances. The cost predictions become more interesting as photovoltaic technology develops and the LCOE from renewable sources decreases. Using the LCOE listed in table 6.2, the OpEx would be expected to diminish to 560 €/$t_{NH_4NO_3}$ in 2030 and to 395 €/$t_{NH_4NO_3}$ in 2050. However, as

previously mentioned, these energy costs should be considered as a lower limit for the OpEx as, in order to sustain a continuous NH_4NO_3 production, a mix of different energy sources, as well as a grid integration to sell the energy excesses and buy when needed, should be preferred. The implications of cheaper renewable energy are further discussed in section 6.5.

6.4.3 Transport costs analysis

Due to the large production scale, transportation costs for the final product to be delivered to retail sellers should be taken into account for the classical SMR-HB facility. This is not the case for the plasma-based NF facility since its production scale is meant to be sufficient to only meet the demand of the local farmers. The transport costs are based on a market report from Upply [123] which shows the relation between the average freight rate, expressed in €/km, and the journey length. As stated in the introduction, the typical HB-based plant can produce enough fertilizer to meet the demand of an order of magnitude of 100 000 km^2 of arable land. Thus, two typical distances of 100 km and 1000 km are studied to understand the effects of shipments on NH_4NO_3 prices. The average reported price is between 300 € and 1500 € for a standard 22t cargo [123], increasing the final price by 14 to 68 €/$t_{NH_4NO_3}$. The estimation presented might suffer from an underestimation as NH_4NO_3 requires additional safety procedures whose impact on the transport cost is difficult to quantify.

6.5 Cost comparison

Figure 6.2 summarizes the costs per ton of NH_4NO_3. With the assumptions of this chapter, in both cases, the OpEx is responsible for most of the NH_4NO_3 production cost. While the CapEx is expected to be only slightly higher for a plasma-based facility, the Opex of the HB-based plant is currently expected to be lower by a factor of 4, effectively making plasma-based NF nonappealing even if transport costs are considered. As, for a hypothetical plasma-based NF facility, the largest contribution by far is due to the electricity, the OpEx needs to be reduced by improving the energy cost of plasma-based NF and by lowering the LCOE. While the predicted decrease in the LCOE from renewable sources would result already in a reduction of the production cost from 1348 to 683 €/$t_{NH_4NO_3}$ by 2050, the plasma-based NF production cost would still be higher with the current natural gas price.

More generally, as the LCOE from renewable sources is predicted to decrease and the natural gas price fluctuates, the plasma-based NF energy efficiency needed to obtain an economically competitive alternative evolves accordingly. This is shown in figures 6.3(a) and 6.3(b) where, for different values of the energy cost for plasma NF into NO_x, each line represents the LCOEs and gas prices for which the plasma NF-based NH_4NO_3 production cost is equal to its classical SMR-HB counterpart according to equation 6.8.

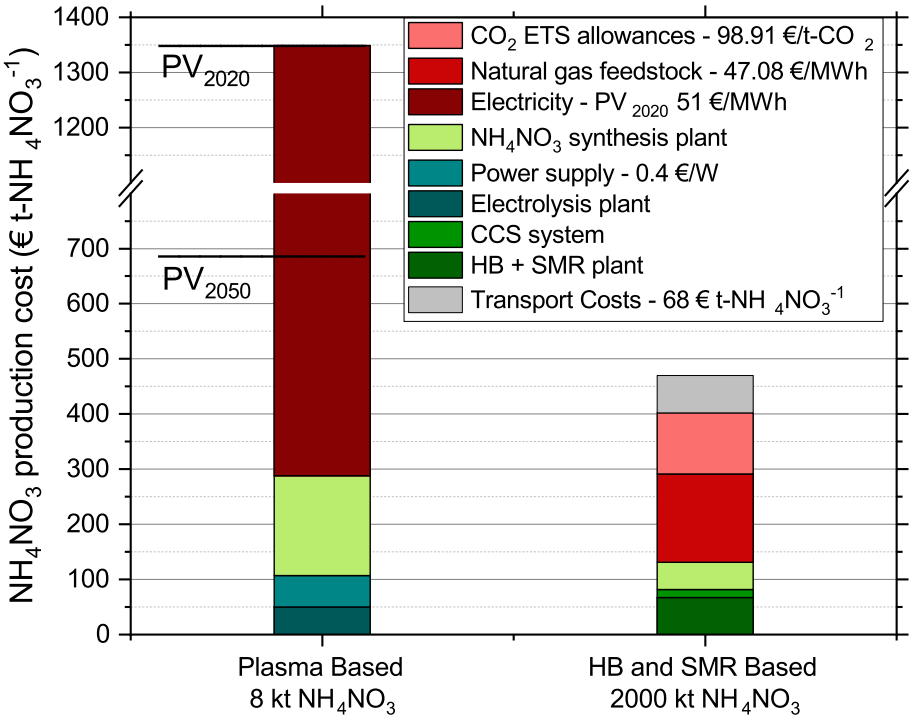

Figure 6.2: NH_4NO_3 production cost comparison using plasma-based NF and SMR-HB divided into its CapEx (green) and OpEx (red) components. With the 2050 predictions for the LCOE, the price for plasma-based NF would evolve to approximately half of the current estimation.

$$\begin{aligned} (CapEx + OpEx)_{plasma} = \\ = (CapEx + OpEx)_{SMR-HB} + \text{transport costs} \end{aligned} \tag{6.8}$$

The transport cost is assumed to be 68 €/$t_{NH_4NO_3}$ in figure 6.3(a) and 14 €/$t_{NH_4NO_3}$ in figure 6.3(b). The current gas price and photovoltaic LCOE, as in tables 6.1 and 6.2 respectively, are highlighted with a red dashed line. The current plasma NF energy cost is plotted in blue. The region that would require a plasma NF energy cost below its theoretical limit is excluded (upper left corner). It should be noted that the energy cost for NF also affects the CapEx by determining the requirements for the power supply.

The effect of the transport cost, as expected, becomes more noticeable as both the LCOE and gas prices decrease, especially as electricity is the main responsible for the production costs of a plasma-based NF facility. It should be noted, when discussing figures 6.3(a) and 6.3(b), that the lower the LCOE and the gas price are, the more the model is sensitive to the assumptions done

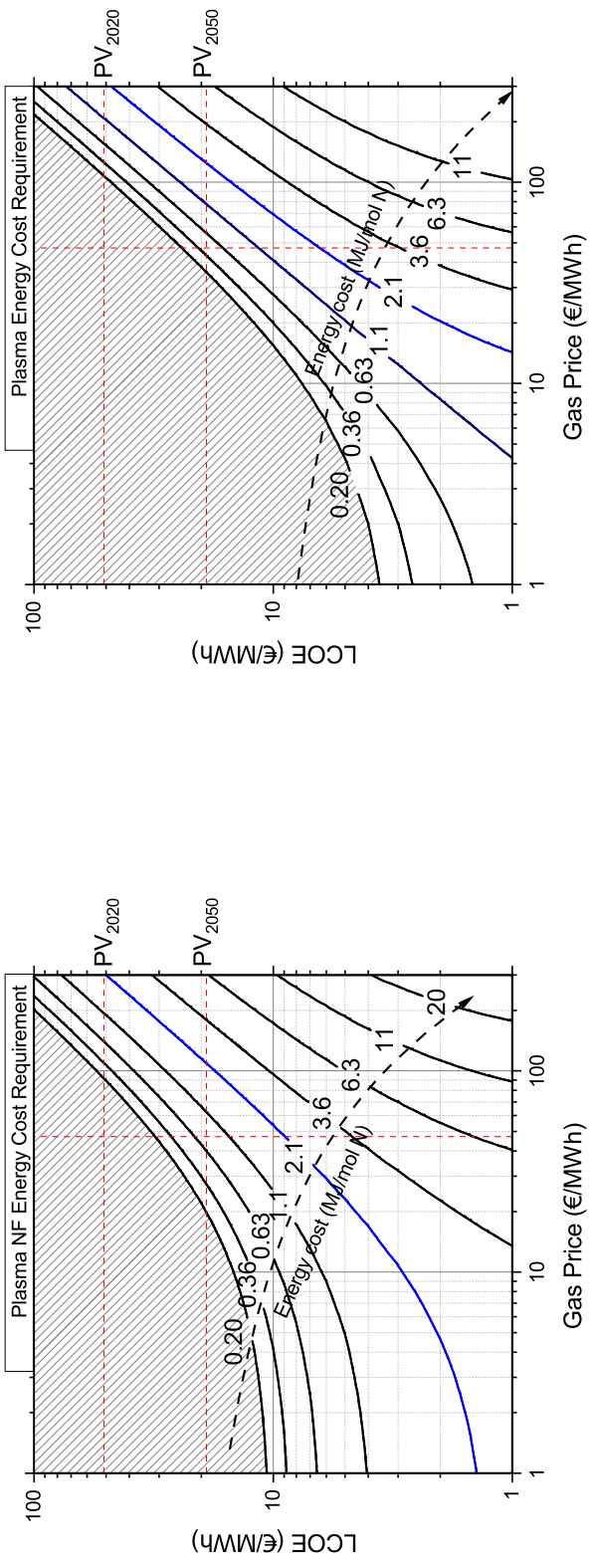

(a) (b)

Figure 6.3: LCOE required for Plasma NF NH_4NO_3 production cost to be equal to SMR-HB as a function of the gas price and for different plasma NF energy efficiencies (black contour lines). The blue contour line indicates the best plasma-based NF EC reported so far at atmospheric pressure [52], while the red dashed lines indicate the LCOE for 2020, its predicted evolution in 2050 and the current market price for natural gas. The transport costs are assumed to be 68 €/$t_{NH_4NO_3}$ (a) and 14 €/$t_{NH_4NO_3}$ (b).

when evaluating the CapEx. From figure 6.3(a) considering the current plasma-based-NF performances (i.e. 2.1 MJ/mol N [52]), the hypothetical facility discussed in this chapter would be an economically viable alternative only if LCOE dropped to 9 €/MWh or if natural gas was sold at more than 300 €/MWh. This LCOE is a factor of five lower than the LCOE for PV electricity production in 2020 and approximately 50% lower than the LCOE for PV electricity production predicted for 2050, while the gas price of 300 €/MWh is at least six times higher than the current price. The result is worse if the lower extreme of the transport costs range proposed is considered, as in figure 6.3(b), where the required LCOE would be 7 €/MWh. For the current market scenario, the implementation of the plasma-based setup proposed is thus not a viable option regardless of its energy cost. This is caused by the cost of H_2 production. While a SMR-HB facility requires 3 mol H_2 per mol of NH_4NO_3, for the proposed plasma facility 4.6 mol H_2 are required for the same amount of NH_4NO_3 despite producing only half of the NH_3 [65]. As it is clear by crossing the corresponding red dashed lines in figure 6.3(a), however, based on the LCOE estimations of 2050 and a natural gas price of 47 €/MWh, an energy cost lower than approximately 0.8 MJ/mol N would allow plasma-based NF to be a viable alternative depending on the transport costs. This estimation assumes the same CO_2 allowances price. While the market value for the natural gas is hard to predict, the CO_2 allowances price is likely to increase according to the current EU carbon policy, effectively resulting in plasma-based NF to be favored on SMR-HB despite its higher energy cost.

6.5.1 HB electrification

If the market effectively evolves towards a scenario where the LCOE is consistently lower than the natural gas price, it is safe to assume that the fertilizer manufacturing industry will progressively electrify. With the current best available technology an energy cost of 0.59 MJ/mol N has been achieved [22, 31], corresponding to 4.1 MWh/$t_{NH_4NO_3}$. According to IEA's ammonia technology roadmap [31] an electrified HB facility would require a similar investment as a classic SMR-HB one, resulting in the same CapEx for the two.

In such a scenario, NH_4NO_3 production costs for plasma-based NF and HB_{el} should be compared. By studying the case in which the production costs are equal, described by equation 6.9, the energy cost requirement for plasma-based NF can be obtained as a function of the LCOE, as shown in figure 6.4.

$$\begin{aligned} (CapEx + OpEx)_{plasma} = \\ = (CapEx + OpEx)_{HB_{el}} + \text{transport costs} \end{aligned} \tag{6.9}$$

Where, for the HB_{el}, transport cost 68 €/$t_{NH_4NO_3}$ is assumed. When expanding equation 6.9, it should be noted that the energy cost for NF also affects the requirements for the power supply, and thus the CapEx. This result shows that, with the current LCOE predictions for the upcoming

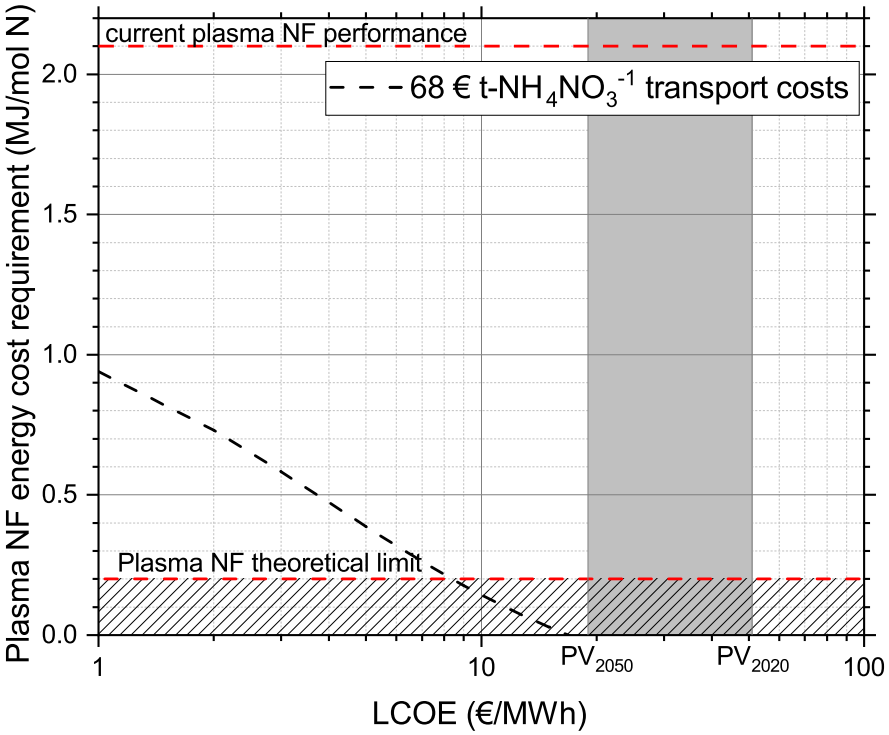

Figure 6.4: Plasma NF energy cost required for NH_4NO_3 production cost based on the discussed setup to be equal to HB_{el} as a function of the LCOE.

decades and the assumptions made in this chapter, the proposed setup won't be able to provide an economically competitive source of NH_4NO_3 until the energy cost for plasma-based NF approaches its theoretical limit and in a scenario characterized by high transport costs. If the lower extreme for the transport costs of 14 €$/t_{NH_4NO_3}$ is assumed, which is not shown in figure 6.4, the $CapEx_{plasma}$ alone would be higher than the NH_4NO_3 production cost with HB_{el} and the transport costs.

Considering that the high amount of losses of H_2 in the catalytic process of the proposed design greatly affects the performance of a plasma-based NF facility, it can be interesting to study what are the requirements for a general small-scale plasma-based facility to produce economically competitive NH_4NO_3. As the CapEx would depend on the design, the condition described by equation 6.9 cannot be studied directly. Therefore, a case study can be proposed by assuming the same CapEx for the two facilities, thus, resulting in a comparison between the OpEx as in equation 6.10.

$$OpEx_{plasma} = OpEx_{HB_{el}} + \text{transport costs} \tag{6.10}$$

Both the transport costs of 14 €/$t_{NH_4NO_3}$ and 68 €/$t_{NH_4NO_3}$ are considered for the HB_{el}. From this equation, the energy cost required for the whole plasma-based NF facility (thus, including the cost for H_2 production) can be obtained and studied as a function of the LCOE as shown in figure 6.5.

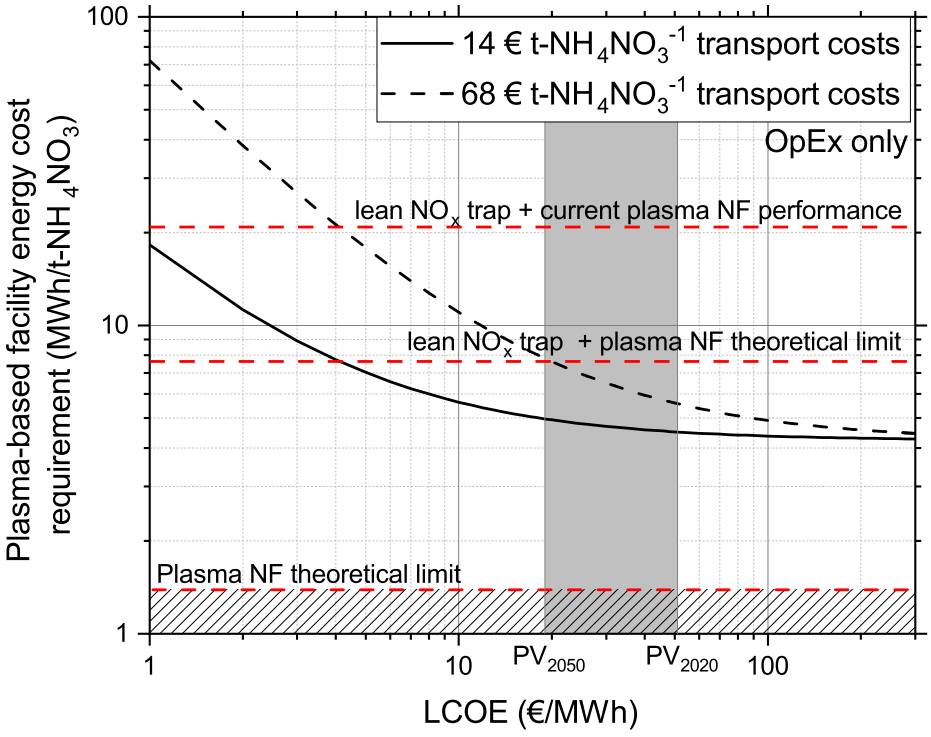

Figure 6.5: Energy cost required for a general plasma-based facility to equal the OpEx of an HB_{el} facility as a function of the LCOE.

As expected, the impact of the transport costs on the plasma-based NF energy cost required becomes more noticeable as the LCOE decreases. Considering the proposed scenario for 2050 energy production and if a transport cost of 68 €/$t_{NH_4NO_3}$ is assumed, it is shown that an energy cost below 8 MWh/$t_{NH_4NO_3}$ would be required for plasma-based NF alternatives to be economically viable. This, with the current LCOE predictions and in agreement with the results previously discussed with figure 6.4, with the implementation of a lean NO_x trap, would only be possible when plasma-based NF reaches its theoretical limit for the energy cost. This highlights how, for the production of NH_4NO_3, optimizing the energy cost for plasma-based NF and limiting the losses of H_2 in the conversion from NO_x to NH_3 are equally important.

As an alternative approach, the NO_x to NH_3 conversion step could be avoided by combining plasma-based HNO_3 production with NH_3 from HB_{el}. In this context, a more encouraging result of 1.1-1.5 MJ/mol N was identified as the necessary energy cost range for plasma-based NF to be an economically viable alternative in another feasibility study by K. Rouwenhorst et. al. [19, 124].

6.5.2 Sensitivity analysis

While the effects of the LCOE are discussed in the previous sections, the analysis presented in this chapter is based on assumptions on a different range of parameters that can vary or evolve with time: market prices are known to experience strong fluctuations in short time periods and assumptions on the CapEx and the depreciation time can vary based on the location and the year of commission. Therefore, a sensitivity analysis showing how the estimation of NH_4NO_3 production costs is affected by variation on the initial assumptions has been conducted and is shown in figures 6.6(a) and 6.6(b) for the classic SMR-HB and the plasma-based NF facilities respectively.

Unsurprisingly, figure 6.6(a) shows that production costs are strongly affected by a variation on the gas price, as a 50 % increase would cause the estimated production cost to increase by 19 % from 405 €/$t_{NH_4NO_3}$ to 483 €/$t_{NH_4NO_3}$. A similar effect is determined by a variation of CO_2 allowances price and of the CapEx, for which a 50 % increase would cause the final product cost estimation to increase by approximately 14 %. In figure 6.6(b) it can be seen that the effects of CapEx and depreciation time are milder in terms of relative increase or decrease on the plasma-based NF facility. However, this is due to the OpEx being responsible for most of the production and, in terms of absolute production cost variation, it is comparable with what is presented in figure 6.6(a). For the same reason, the sensitivity on the energy cost for plasma NF is shown to be crucial, as a 50 % variation would affect the NH_4NO_3 production costs by up to 24%.

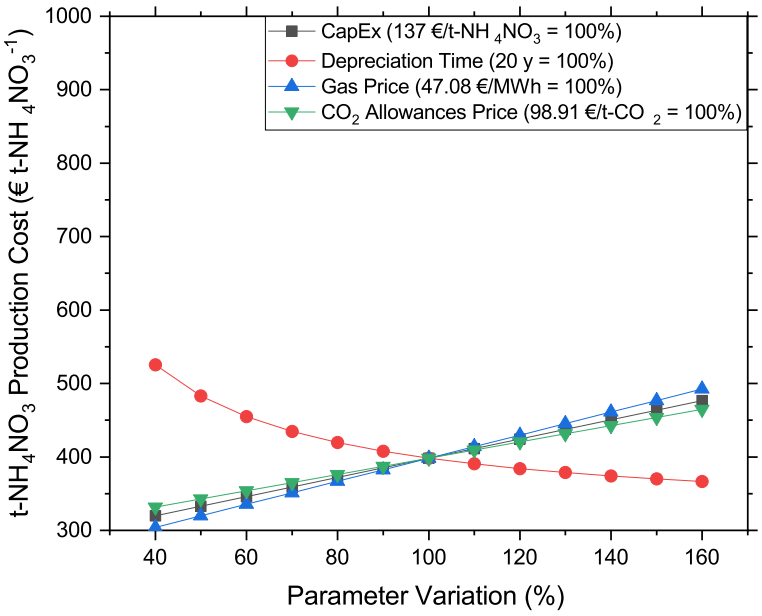

(a)

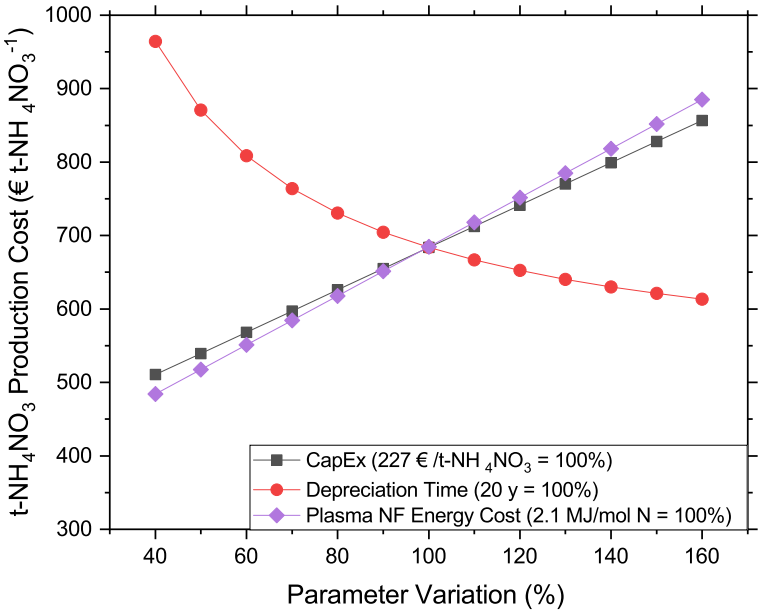

(b)

Figure 6.6: Sensitivity analysis of NH_4NO_3 production costs for a classical SMR-HB (a) and for a plasma NF-based (b) facility.

6.6 Conclusions

This chapter highlights that, in the current state of the art, plasma-based NF is not a viable alternative to the classic combination of HB and SMR due to the high OpEx caused by the current energy cost of plasma-based NF and by the higher amount of H_2 required to form NH_3 from NO_x. This might change in a future scenario where a combination of cheaper LCOE and more expensive CO_2 allowances in the EU would push the fertilizer industry towards electrification. As a reference, the plasma NF theoretical limit would correspond to 1.39 MWh/$t_{NH_4NO_3}$ and only 2 MWh/$t_{NH_4NO_3}$ of H_2 are effectively converted into NH_3. This, if a more efficient H_2 use is obtained, would fix a milder goal for plasma-based NF compared to reaching the current HB_{el} energy cost of 0.59 MJ/mol N, or even to approaching the theoretical limit of 0.2 MJ/mol N for the technology. In this scenario, plasma-based NF can be designed as a complementary technology to the HB in the NH_4NO_3 production industry, supplying regions where high transport costs are necessary for the fertilizer to be delivered.

Until then, alternative implementations of plasma-based NF should be investigated. As an example, plasma-based NO_x production for HNO_3 could be combined with HB_{el} to produce NH_4NO_3 [19]. Additionally, an application that is recently gaining interest is to combine plasma-based NF into NO_x with NH_3 naturally released from manure, effectively avoiding the need for H_2 production to obtain NH_4NO_3 and tackling the problem of nitrogen air pollution and eutrophication [125, 126].

Chapter 7

General conclusions and perspectives

The final chapter discusses the overall conclusions of the thesis, highlighting the main achievements and expanding on the future perspectives of plasma-based NF.

7.1 Conclusions

NF is, nowadays, an essential industrial process thanks to which almost half of the world population is fed. As widely discussed in the introductory chapter, the current most widely used method for the production of nitrogen-based fertilizers is the H-B process which, despite having solidified its role as the dominant industrial for more than a century, presents a few drawbacks. Among these, the most critical are its energy consumption, the strong CO_2 emissions, and the requirement of huge, centralized, production facilities, which can negatively affect the fertilizer logistics. For this reason, the implementation of more sustainable NF processes is one of the crucial challenges of this century and plasma-based NF has been identified as a candidate to overcome this challenge. In this context, this thesis specifically addresses the investigation of plasma-based NF using a GAP discharge operating with an N_2-O_2 gas mixture at atmospheric pressure with a multi-level, transversal, approach.

Focusing on a more fundamental level, this study investigated the N_2-O_2 GAP plasma chemistry with the characterization of the plasma afterglow by non-intrusive optical plasma diagnostics techniques such as FTIR and LIF. Characterizing an atmospheric N_2-O_2 plasma afterglow discharge proved challenging as the more well-established methods normally used for determining the species density and temperatures are incompatible with the studied discharge. The necessity of acquiring such information, therefore, pushed for the development of a novel method for the determination of the NO(X, $\nu = 0$) rotational temperature T_{rot}, a few mm below the anode, based on the line ratio between the $J = 33.5$ and the $J = 21.5$ LIF peaks. The $J_{33.5}/J_{21.5}$ line ratio is then studied with LIFBASE and shown to be a monotonic function of T_{rot} and used to provide a 2D spatial evolution of T_{rot}. With the information on the gas temperature, measuring a 2D spatial profile for the NO(X) density is also possible. The development of a reliable method to directly measure T_{rot} and the NO(X) concentration in the afterglow can prove to be crucial, especially if combined with simulative tools, to gain more insight into the role of possible back-reactions and quenching. Indeed, in this thesis, such a method allowed to determine the importance of the input gas flow rate in affecting the shape of the plasma afterglow, and thus, the temperature and NO(X) density gradients in that region. The role of gas cooling is also investigated by combining LIF and FTIR spectroscopy, which are used to study the NO_x yield and the NO selectivity, two crucial parameters for the success of plasma-based NF technology in industry. An increase in the cooling rate is shown to correspond to a faster NO conversion speed into NO_2 which is beneficial as NO_2 is required to produce nitric acid HNO_3, a fundamental component in the ammonium nitrate fertilizer production chain.

Given a possible future industrial implementation of GAPs, particular attention has been devoted to the energy cost, the NO_x yield, and the stability of the discharge. In the literature, resistors up to tens of kΩ are often introduced in series with any type of GA discharge as they enhance the stability of the arc discharge by limiting the fluctuations of the arc itself. However, their impact on the overall energy cost is usually neglected. This thesis demonstrates that such external resistors can dramatically increase the total power consumption of the system, and therefore, an

alternative approach is suggested. It has been demonstrated that replacing the resistor with an inductor also allows for a decent stabilization of the discharge and, most importantly, allows to avoid the loss of power through Joule dissipation. The effect of the two different passive electric components is compared and observed to play a negligible role in the chemistry of the plasma, effectively allowing the NO_x yield to be unaffected by the choice. The use of an inductor is particularly promising for the upscaling of the GAP technology, both in terms of energy costs as it was observed to remain constant at around 3 MJ/mol upon increasing power, and in terms of limit for the arc current since less power (and thus, heat) is dissipated on an inductor. As a result, an inductor can usually sustain higher currents without overheating and breaking. For this reason, thus far, in the literature, the investigation on GAPs and RGAs has been limited in terms of applied current. As an example, in the context of this thesis, the limit on the arc current is imposed by the power rating of the external resistors (of, at least, 2kΩ) used in series with the GAP, allowing for a maximum of approximately 300 mA, well below the 1.25 A that could be provided by the available power supply. Thus, replacing the external resistors with inductors should be favored, not only for better energy efficiency but also as this would allow further study of GAPs and RGAs with higher powers which are normally avoided due to the constraints imposed by the resistors.

Finally, the economic feasibility of upscaling plasma-based technology is then further investigated by an analysis of the production costs of nitrogen fertilizer, highlighting how, in the current scenario, plasma-based NF is not yet a viable alternative to the classic combination of HB and SMR. The two main drawbacks in the direct production of NH_4NO_3 identified are the high electricity costs associated with the best energy cost of the technology reported so far and the higher amount of H_2 required to form NH_3 from NO_x. The result of the analysis might change as the sector evolves towards electrification thanks to a combination of cheaper electricity production and more expensive CO_2 allowances. In this context, plasma-based technology is compared with the electrified H-B process and it is proved that a better efficiency in the use of H_2 to form NH_3 is required for plasma-based technology to be economically advantageous. Until then, alternative implementations of plasma-based NF should be investigated and more effort should be dedicated to the realization of feasibility studies, conceptually testing the technology requirements for different industrial applications. As an example, plasma-based NO_x production for HNO_3 could be combined with HB_{el} to produce NH_4NO_3 [19]. Also, an application that is recently gaining interest is to combine plasma-based NF into NO_x with NH_3 naturally released from manure, effectively avoiding the need for H_2 production to obtain NH_4NO_3.

7.2 Future perspectives

Despite the recent progress in the field of plasma-based NF, the research effort required to approach the experimental limits of the technology is far from over. This is also true for GA plasmas, for which 3D geometries have proved to be among the most successful designs for NF into NO_x, and are quite promising due to how relatively easily they can be upscaled.

In terms of fundamental plasma chemistry research, the proposed LIF-based technique for the determination of the T_{rot} and NO(X) density in the afterglow could be used on a wider variety of experimental conditions. Most notably, it would be particularly useful to implement this diagnostic method to study the afterglow of RGAs operating at higher pressures or that are optimized for fast temperature quenching, both conditions that are proven to enhance the performance of plasma-based NF [52, 53]. More generally, it would be interesting to probe the active plasma region with this LIF-based method. According to the simulation results, the region covered by the arc is where most of the NO is formed and, thus, the experimental determination of the plasma temperatures and the NO density would allow a thorough understanding of the plasma chemistry for NF and on how to optimize it. Additionally, probing the active plasma region would allow the observation of the atomic species N and O through two photons LIF. In addition to the measurements of the afterglow, having access to the active plasma region to characterize the density and temperatures of the species would allow a direct and valuable benchmark for the simulative tools, allowing them to model the discharge with even greater accuracy.

However, the current 3D geometries based on GA (such as the GAP and the RGA) would need to be adapted to allow for an "experimental accessibility" and, thus, more focus should be devoted to the conceptualization of better 3D gliding arc designs based on this. Additionally, if the operating pressure is increased, it should be considered that NO being a strong absorber would effectively require a short optical length for a LIF-based method to be effective. This, together with addressing the low fraction of gas interacting with the arc and introducing heat sinks for a faster quenching in the afterglow region, suggests that considerable effort should be devoted to the conceptualization of new 3D geometries for gliding arcs.

Concerning the industrial applicability of the technology, as previously mentioned, in the literature, the investigation on GAPs and RGAs has been limited in terms of applied current. If, as suggested, external resistors are replaced with inductors, a wider range of arc current would become available for studying plasma-based NF, allowing for the investigation of plasma conditions that would be closer to the operating conditions of an ideal, upscaled, plasma-based NF facility.

Finally, as shown in Chapter 6, the energy efficiency of the technology is ultimately one of the greatest challenges for the industrial application of plasma-based NF. While it is still crucial to study and improve the performance of the plasma-chemical process itself, additional energy costs induced by the equipment that is necessary for the gliding arc to operate should not be neglected, as the effort to lower these energy costs is equally as important given a possible future industrial upscaling. More effort is, therefore, suggested in this direction, not only in terms of optimizing the stabilization of the process and decreasing the energy cost associated with it through the proper choice of external components, as it is discussed in Chapter 5 of this thesis, but also by integrating these, more efficiently, in dedicated power supply units.

Appendix A

Inductor power consumption

The results in Chapter 4 highlight how replacing the set of external resistors with an inductor is beneficial for the energy cost of the process. In Chapter 4 the power consumption induced by the inductor is considered to be negligible and thus, not included in the calculations. The power loss caused by the inductor is generally difficult to evaluate, as a direct calculation requires parameters that are often not publicly shared by the producers [127, 128].

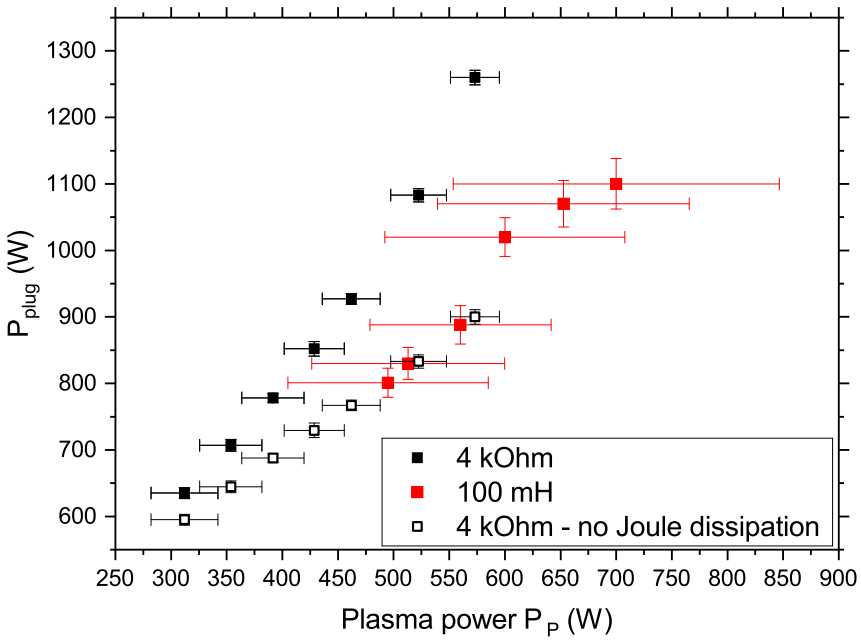

Figure A.1: Power consumption with a 4 kΩ resistance and with a 100 mH inductance measured at the plug for a GAP operating with 10 slm of N_2.

Therefore, to evaluate the power loss caused by the inductor, a digital wattmeter was installed at the plug, measuring the power consumption associated with the entire setup. For this set of measurements, a gas composition of 5 slm N_2 and 5 slm O_2 is used.

Figure A.1 shows the power consumption measured at the plug (P_{plug}) as a function of the plasma power P_P with a 4 kΩ resistance and with a 100 mH inductor. As a reference, the Joule dissipation (IR^2) is subtracted from the power consumption of the GAP with the 4 kΩ resistance for a better comparison with the inductor case. The power consumption due to the mass flow controller (ca. 8 W) and of the cooling fan (ca. 75 W) is included in each set.

The uncertainty on the plasma power measurements do not allow to precisely estimate the power consumption introduced with the inductor. However the P_{plug} measured with the inductor are observed to be compatible with the 4 kΩ case where the Joule dissipation is subtracted, thus, suggesting that the power dissipation introduced with the inductor can be neglected.

Appendix B

LIF

In order to properly measure the NO(X) density, equation (3.11) assumed that the LIF signal is not saturated. This can be verified by ensuring the linearity between the fluorescence intensity (I_{LIF}) and the laser intensity I_{las} (or the beam energy as they are linearly dependent).

$$I_{LIF} \propto I_{las} \tag{B.1}$$

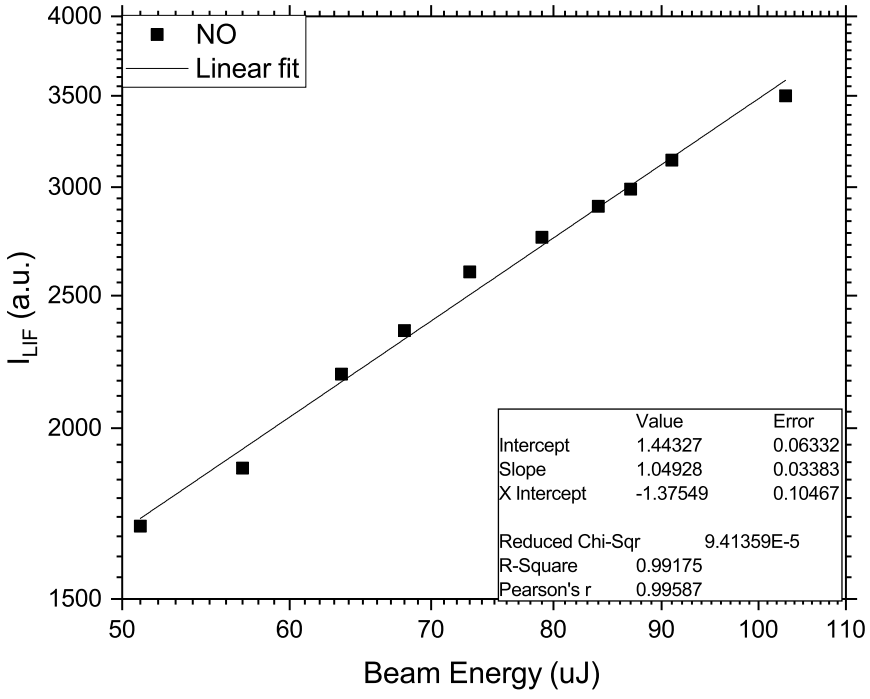

Figure B.1: NO LIF signal intensity observed as a function of the laser beam energy. The beam wavelength is 224.792 nm, the arc current is 200 mA, the input gas flow is 10 slm.

Figure B.1 shows I_{LIF} as a function of the beam energy measured for the $J = 33.5$ transition (at 224.792 nm) with the arc current and the input gas flow set at 200 mA and 10 slm respectively.

Since both the axes are in log-scale, the slope α of the linear fit describes the proportionality

$$I_{LIF} \propto I_{las}^{\alpha} \tag{B.2}$$

where, if $\alpha \simeq 1$, the linearity assumption is verified.

Appendix C

Methane plasma pyrolysis

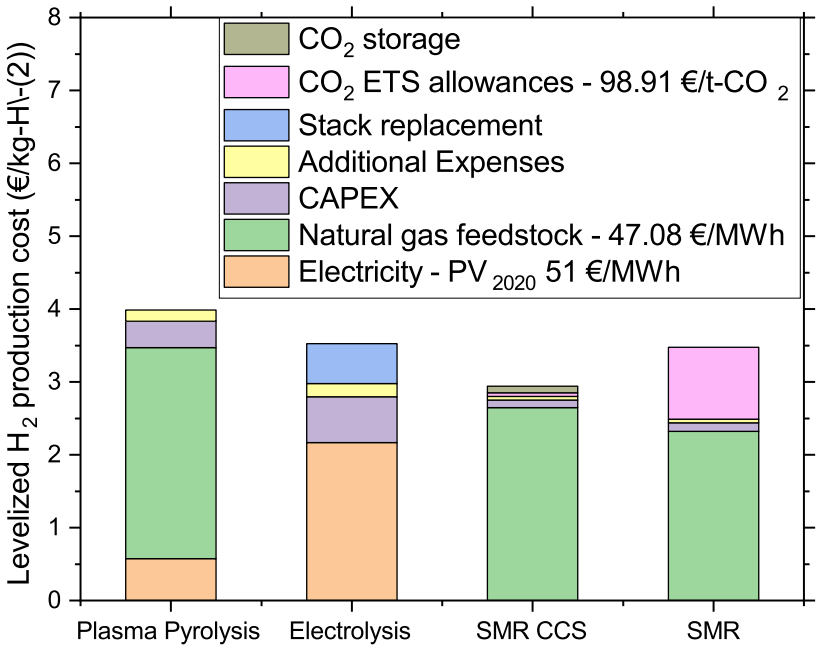

Figure C.1: Levelized H_2 production costs evaluated with the prices in table 6.1 for different methods. Readapted from [129].

Methane plasma pyrolysis has also been considered as an alternative for H_2 production. This process consists in converting methane in the absence of oxygen, or other hydrocarbons, into H_2 and solid carbon

$$CH_4 \rightarrow C + 2H_2, \tag{C.1}$$

where about 3 tons of solid carbon are produced per ton of H_2 as a byproduct. Figure C.1 shows the levelized cost of H_2 production for methane plasma pyrolysis and the two methods discussed

in this work: water electrolysis and SMR with and without CCS. The data shown in the graph are based on what has been reported in a 2020 article by Timmerberg et al. [129] and have been updated with the current prices shown in table 6.1. The result is heavily affected by the gas price and the comparison greatly differs from what was reported in 2020, when natural gas price registered its minimum in the Dutch TTF index. For small-scale applications the H_2 production cost for methane plasma pyrolysis could, in principle, be mitigated by selling the solid carbon obtained as a byproduct, thus potentially becoming a competitive alternative depending on the price for solid carbon. Nevertheless, this work focuses on water electrolysis as it would benefit more than pyrolysis from the LCOE decrease for renewable that is currently predicted in the decades to come.

Bibliography

[1] D. C. Frost, C. A. McDowell, C. E. H. Bawn, *Proc. R. Soc. Lond. A* **1956**, *236*, 278–284.

[2] J. W. Erisman, M. A. Sutton, J. Galloway, Z. Klimont, W. Winiwarter, *Nat. Geosci.* **2008**, *1*, 636–639.

[3] D. A. Daramola, M. C. Hatzell, *ACS Energy Letters* **0000**, *0*, 1493–1501.

[4] Forecast of food, farming & fertilizer use in the European Union 2022-2032, tech. rep., Fertilizers Europe, **2022**.

[5] FAOSTAT statistical database, tech. rep., Food and Agriculture Organization of the United Nations.

[6] N. Cherkasov, A. Ibhadon, P. Fitzpatrick, *Chem. Eng. Process* **2015**, *90*, 24–33.

[7] J. M. Clomburg, A. M. Crumbley, R. Gonzalez, *Science* **2017**, *355*, aag0804.

[8] I. Rafiqul, C. Weber, B. Lehmann, A. Voss, *Energy* **2005**, *30*, 2487–2504.

[9] IEA, Global CO_2 emissions in 2019, tech. rep., International Energy Agency, **2020**.

[10] B. Patil, Q. Wang, V. Hessel, J. Lang, *Catalysis Today* **2015**, *256*, Plasmas for enhanced catalytic processes, 49–66.

[11] M. M. Sarafraz, N. N. Tran, H. Nguyen, L. Fulcheri, R. Burton, P. Wadewitz, G. Butler, L. Kirton, V. Hessel, *J. Adv. Manuf. Process.* **2021**, *3*, e10081.

[12] C. Frink, P. Waggoner, J. Ausubel, *Proc. Natl. Acad. Sci. U.S.A.* **1999**, *96*, 1175–1180.

[13] C. Claudine, K Lindström, C Elmerich, *Plant and Soil* **2009**, *321*, 35–59.

[14] A. Bernhard, *Nature Education Knowledge* **2010**, *3(10)*, 25.

[15] CIMMYT, Nitrogen in agriculture, image retrieved from: https://www.cimmyt.org/news/nitrogen-in-agriculture/, **2020**.

[16] FAO, World fertilizer trends and outlook to 2022, tech. rep., Food and Agriculture Organization of the United Nations, **2019**.

[17] V. Smil, *Enriching the Earth: Fritz Haber, Carl Bosch, and the Transformation of World Food Production*, **2004**.

[18] A. S. Travis in *Nitrogen Capture: The Growth of an International Industry (1900–1940)*, Springer International Publishing, Cham, **2018**, pp. 49–92.

[19] K. H. R. Rouwenhorst, F. Jardali, A. Bogaerts, L. Lefferts, *Energy Environ. Sci.* **2021**, *14*, 2520–2534.

[20] A. S. Travis, *The synthetic nitrogen industry in World War I: Its emergence and expansion*, Springer International Publishing, **2015**.

[21] A. Bogaerts, E. C. Neyts, *ACS Energy Letters* **2018**, *3*, 1013–1027.

[22] C. Smith, A. K. Hill, L. Torrente-Murciano, *Energy Environ. Sci.* **2020**, *13*, 331–344.

[23] K. H. R. Rouwenhorst, L. Lefferts, *Catalysts* **2020**, *10*, 999.
[24] M. Will, *Proceedings of the NH_3 Fuel Conference* **2018**.
[25] P. Pfromm, *J. Renew. Sustain. Energy* **2017**, *9*, 034702.
[26] M. Reese, C. Marquart, M. Malmali, K. Wagner, E. Buchanan, A. McCormick, E. Cussler, *Ind. Eng. Chem. Res.* **2016**, *55*, 3742–3750.
[27] E. Morgan, J. Manwell, J. McGowan, *ACS Sustain. Chem. Eng.* **2017**, *5*, 9554–9567.
[28] H. Vrijenhoef, *Proceedings of the NH_3 Fuel Conference* **2017**.
[29] J. Schmuecker, D. Toyne, *Proceedings of the NH_3 Fuel Conference* **2019**.
[30] Yara, Yara Integrated Report 2020, tech. rep., Yara.
[31] IEA, Ammonia Technology Roadmap, tech. rep., International Energy Agency, **2021**.
[32] Production of ammonia, nitric acid, urea and N fertilizer, tech. rep., Environment Agency Austria Umweltbundesamt, **2017**.
[33] M. Wang, A. Elgowainy, Z. Lu, A. Bafana, S. Banerjee, P. T. Benavides, P. Bobba, A. Burnham, H. Cai, U. Gracida, T. R. Hawkins, R. K. Iyer, J. C. Kelly, T. Kim, K. Kingsbury, H. Kwon, U. Lee, Y. Li, X. Liu, L. Ou, N. Siddique, P. Sun, P. Vyawahare, O. Winjobi, M. Wu, H. Xu, E. Yoo, G. G. Zaimes, G. Zang, Greenhouse gases, Regulated Emissions, and Energy use in Technologies Model (2021 .Net), Computer Software, **2021**.
[34] P. Gibbon, *CERN Yellow Reports* **2016**, Vol 1 (2016): Proceedings of the 2014 CAS–CERN Accelerator School: Plasma Wake Acceleration.
[35] A. Fridman, *Plasma Chemistry*, Cambridge University Press, **2008**.
[36] M. Goossens, *An Introduction to Plasma Astrophysics and Magnetohydrodynamics*, 1st ed., Springer, **2003**.
[37] A. Fridman, L. A. Kennedy, *Plasma physics and engineering, 2nd edition*, CRC Press, **2011**.
[38] V. N. Ochkin, *Spectroscopy of Low Temperature Plasma*, Wiley-VCH Verlag GmbH & Co. KGaA, **2009**.
[39] U. Fantz, *Plasma Sources Sci. Technol.* **2006**, *15*, S137.
[40] P. J. Bruggeman, N Sadeghi, D. C. Schram, V Linss, *Plasma Sources Sci. Technol.* **2014**, *23*, 023001.
[41] E. Vervloessem, M. Aghaei, F. Jardali, N. Hafezkhiabani, A. Bogaerts, *ACS Sustain. Chem. Eng.* **2020**, *8*, 9711–9720.
[42] W. Wang, B. Patil, S. Heijkers, V. Hessel, A. Bogaerts, *ChemSusChem* **2017**, *10*, 2145–2157.
[43] J. R. Roth, *Industrial Plasma Engineering Volume 1: Principles*, 1st, CRC Press, **1995**.
[44] Y. P. Raizer, J. E. Allen, *Gas Discharge Physics*, 1st ed., Springer Berlin, **2011**.
[45] A. Fridman, S. Nester, L. A. Kennedy, A. Saveliev, O. Mutaf-Yardimci, *Progress in Energy and Combustion Science* **1999**, *25*, 211–231.
[46] T. Nunnally, K. Gutsol, A. Rabinovich, A. Fridman, A. Gutsol, A. Kemoun, *Journal of Physics D: Applied Physics* **2011**, *44*, 274009.
[47] M. Ramakers, J. A. Medrano, G. Trenchev, F. Gallucci, A. Bogaerts, *Plasma Sources Science and Technology* **2017**, *26*, 125002.
[48] G. Trenchev, S. Kolev, A. Bogaerts, *Plasma Sources Science and Technology* **2016**, *25*, 035014.

[49] O. Samadi Bahnamiri, F. Manaigo, A. Chatterjee, R. Snyders, F. A. D'Isa, N. Britun, *Journal of Applied Physics* **2023**, *133*, 113303.
[50] S. Li, J. Medrano Jimenez, V. Hessel, F. Gallucci, *Processes* **2018**, *6*, 248.
[51] F. Jardali, S. Van Alphen, J. Creel, H. Ahmadi Eshtehardi, M. Axelsson, R. Ingels, R. Snyders, A. Bogaerts, *Green Chem.* **2021**, *23*, 1748–1757.
[52] S. Van Alphen, H. Ahmadi Eshtehardi, C. O'Modhrain, J. Bogaerts, H. Van Poyer, J. Creel, M.-P. Delplancke, R. Snyders, A. Bogaerts, *Chem. Eng. J.* **2022**, *443*, 136529.
[53] I. Tsonev, C. O'Modhrain, A. Bogaerts, Y. Gorbanev, *ACS Sustainable Chemistry & Engineering* **2023**, *11*, 1888–1897.
[54] O. Samadi Bahnamiri, C. Verheyen, R. Snyders, A. Bogaerts, N. Britun, *Plasma Sources Science and Technology* **2021**, *30*, DOI 10.1088/1361-6595/abff0e.
[55] S. Kelly, A. Bogaerts, *Joule* **2021**, *5*, 3006–3030.
[56] B. Mutel, O. Dessaux, P. Goudmand, *Rev. Phys. Appliquée* **1984**, *19*, 461–464.
[57] R. Asisov, V. Givotov, V. Rusanov, A. Fridman, *Sov. Phys.* **1980**, *14*, 366.
[58] X. Pei, D. Gidon, Y. J. Yang, Z. Xiong, D. B. Graves, *Chem. Eng. J.* **2019**, *362*, 217–228.
[59] B. Patil, N. Cherkasov, J. Lang, A. Ibhadon, V. Hessel, Q. Wang, *Applied Catalysis B: Environmental* **2016**, *194*, 123–133.
[60] X. Pei, D. Gidon, D. B. Graves, *J. Phys. D. Appl. Phys.* **2020**, *53*, 044002.
[61] E. Vervloessem, Y. Gorbanev, A. Nikiforov, N. De Geyter, A. Bogaerts, *Green Chem.* **2022**, *24*, 916–929.
[62] M. L. Carreon, *Journal of Physics D: Applied Physics* **2019**, *52*, 483001.
[63] H. H. Kim, Y. Teramoto, A. Ogata, H. Takagi, T. Nanba, *Plasma Processes and Polymers* **2017**, *14*, 1600157.
[64] P. Peng, P. Chen, M. Addy, Y. Cheng, E. Anderson, N. Zhou, C. Schiappacasse, Y. Zhang, D. Chen, R. Hatzenbeller, Y. Liu, R. Ruan, *ACS Sustainable Chemistry & Engineering* **2019**, *7*, 100–104.
[65] L. Hollevoet, F. Jardali, Y. Gorbanev, J. Creel, A. Bogaerts, J. A. Martens, *Angew. Chem. Int. Ed.* **2020**, *59*, 23825–23829.
[66] L. Hollevoet, E. Vervloessem, Y. Gorbanev, A. Nikiforov, N. De Geyter, A. Bogaerts, J. A. Martens, *ChemSusChem* **2022**, *15*, e202102526.
[67] J. Amorim, G. Baravian, J. Jolly, *Journal of Physics D: Applied Physics* **2000**, *33*, R51.
[68] N. Britun, T. Minea, S. Konstantinidis, R. Snyders, *Journal of Physics D: Applied Physics* **2014**, *47*, 224001.
[69] M. Gromov, K. Leonova, N. D. Geyter, R. Morent, R. Snyders, N. Britun, A. Nikiforov, *Plasma Sources Science and Technology* **2021**, *30*, 065024.
[70] M. Gromov, K. Leonova, N. Britun, N. De Geyter, R. Morent, R. Snyders, A. Nikiforov, *React. Chem. Eng.* **2022**, *7*, 1047–1052.
[71] A. F. H. van Gessel, B Hrycak, M Jasiński, J Mizeraczyk, J. J. A. M. van der Mullen, P. J. Bruggeman, *Journal of Physics D: Applied Physics* **2013**, *46*, 095201.
[72] X. M. Zhu, Y. K. Pu, *Journal of Physics D: Applied Physics* **2010**, *43*, 403001.

[73] A. J. Wu, H. Zhang, X. D. Li, S. Y. Lu, C. M. Du, J. H. Yan, *IEEE Transactions on Plasma Science* **2014**, *42*, 3560–3568.

[74] T. L. Zhao, Y. Xu, Y. H. Song, X. S. Li, J. L. Liu, J. B. Liu, A. M. Zhu, *Journal of Physics D: Applied Physics* **2013**, *46*, 345201.

[75] C. Wu, W. Pan, *Theor. App. Mech. Lett.* **2011**, *1*, 024001.

[76] A. Anastasopoulou, Q. Wang, V. Hessel, J. Lang, *Processes* **2014**, *2*, 694–710.

[77] A. Anastasopoulou, R. Keijzer, S. Butala, J. Lang, G. V. Rooij, V. Hessel, *Journal of Physics D: Applied Physics* **2020**, *53*, 234001.

[78] R. Engeln, B. Klarenaar, O. Guaitella, *Plasma Sources Science and Technology* **2020**, *29*, 063001.

[79] A. C. G. Mitchell, M. W. Zemansky, *Resonance Radiation and Excited Atoms*, Cambridge University Press, London, **1971**.

[80] A. Goldman, L. R. Brown, W. G. Schoenfeld, M. N. Spencer, C. Chackerian, L. P. Giver, H. Dothe, C. P. Rinsald, L. H. Coudert, V. Dana, J. Mandin, *J. Quant. Spectrosc. Radiat. Transfer* **1998**, *60*, 825–838.

[81] A. Perrin, J. M. Flaud, A. Goldman, C. Camy Peiret, W. J. Lafferty, P. Arcas, C. P. Rinsald, *J. Quant. Spectrosc. Radiat. Transfer* **1998**, *60*, 839–850.

[82] Sirah Lasertechnik: Tunable Narrow Bandwidth Pulsed Lasers catalogue, image retrieved from: https://www.sirah.com/lasers/he/narrow-bandwidth/, **2023**.

[83] Luxottica-Exciton Laser dyes catalogue, data retrieved from: https://exciton.luxottica.com/laser-dyes.html, **2023**.

[84] I. A. Buyanova, W. M. Chen in *Defects in Advanced Electronic Materials and Novel Low Dimensional Structures*, (Eds.: J. Stehr, I. Buyanova, W. Chen), Woodhead Publishing Series in Electronic and Optical Materials, Woodhead Publishing, **2018**, pp. 189–210.

[85] S. Gröger, M. Ramakers, M. Hamme, J. A. Medrano, N. Bibinov, F. Gallucci, A. Bogaerts, P. Awakowicz, *Journal of Physics D: Applied Physics* **2018**, *52*, 065201.

[86] S. Van Alphen, F. Jardali, J. Creel, G. Trenchev, R. Snyders, A. Bogaerts, *Sustainable Energy Fuels* **2021**, *5*, 1786–1800.

[87] H. Kronemayer, P. Ifeacho, C. Hecht, T. Dreier, H. Wiggers, C. Schulz, *Appl. Phys. BB* **2007**, *88*, 373–377.

[88] S. Iseni, S. Zhang, A. F. H. van Gessel, S. Hofmann, B. T. J. van Ham, S. Reuter, K. D. Weltmann, P. J. Bruggeman, *New Journal of Physics* **2014**, *16*, 123011.

[89] P. Preissing, I. Korolov, J. Schulze, V. S. von der Gathen, M. Böke, *Plasma Sources Science and Technology* **2020**, *29*, 125001.

[90] B. S. Patil, F. J. J. Peeters, G. J. van Rooij, J. A. Medrano, F. Gallucci, J. Lang, Q. Wang, V. Hessel, *AIChE Journal* **2018**, *64*, 526–537.

[91] M. F. Merienne, A. Jenouvrier, B. Coquart, J. P. Lux, *J. Atmos. Chem.* **1997**, *27*, 219–232.

[92] M. D. Di Rosa, R. K. Hanson, *J Quant Spectrosc Radiat Transf.* **1994**, *52*, 515–529.

[93] J. Luque, D. Crosley, *LIFBASE: Database and Spectral Simulation Program*, version 2.1.1, **1999**.

[94] H. E. Bass, G. L. Hill, *The Journal of Chemical Physics* **2003**, *58*, 5179–5180.

[95] T. B. Settersten, B. D. Patterson, J. A. Gray, *The Journal of Chemical Physics* **2006**, *124*, 234308.

[96] J. Voráč, P. Dvořák, V. Procházka, J. Ehlbeck, S. Reuter, *Plasma Sources Sci Technol.* **2013**, *22*, 025016.
[97] N. Britun, V. Gamaleev, M. Hori, *Plasma Sources Science and Technology* **2021**, *30*, 08LT02.
[98] N. Britun, Unpublished data, **2023**.
[99] K. Verbiezen, R. Klein-Douwel, A. van Vliet, A. Donkerbroek, W. Meerts, N. Dam, J. ter Meulen, *Proceedings of the Combustion Institute* **2007**, *31*, 765–773.
[100] V. Ivanov, T. Paunska, S. Lazarova, A. Bogaerts, S. Kolev, *Journal of CO2 Utilization* **2023**, *67*, 102300.
[101] A. Denra, S. Saud, D. B. Nguyen, Q. T. Trinh, T.-K. Nguyen, H. An, N.-T. Nguyen, S. Teke, Y. S. Mok, *Journal of Cleaner Production* **2024**, *436*, 140618.
[102] Y. Kusano, M. Salewski, F. Leipold, J. Zhu, A. Ehn, Z Li, M. Alden, *Eur. Phys. J. D* **2014**, *68*.
[103] M. Ramakers, S. Heijkers, T. Tytgat, S. Lenaerts, A. Bogaerts, *J. of CO2 Util.* **2019**, *33*, 121–130.
[104] G. Trenchev, S. Kolev, W. Wang, M. Ramakers, A. Bogaerts, *J. Phys. Chem. C* **2017**, *121*, 24470–24479.
[105] H. Zhang, L. Li, X. Li, W. Wang, J. Yan, X. Tu, *J. of CO2 Util.* **2018**, *27*, 472–479.
[106] H. Zhang, C. Du, A. Wu, Z. Bo, J. Yan, X. Li, *Int. J. Hydrog. Energy* **2014**, *39*, 12620–12635.
[107] H. Chen, A. Wu, S. Mathieu, P. Gao, X. Li, B. Z. Xu, J. Yan, X. Tu, *Plasma Processes Polym* **2021**, *18*, 2000200.
[108] M. Peters, K. Timmerhaus, R. West, M. Peters, *Plant Design and Economics for Chemical Engineers*, 5th ed., McGraw-Hill Education, **2002**.
[109] Issues in the application of annuities, tech. rep., Queensland Competition Authority, **2014**.
[110] A. Damodaran, Cost of Equity and Capital (US), data retrieved from NYU Stern School of Business, https://pages.stern.nyu.edu/~adamodar/New_Home_Page/datafile/wacc.html, **2023**.
[111] L. Sens, U. Neuling, M. Kaltschmitt, *Renewable Energy* **2022**, *185*, 525–537.
[112] Renewable Power Generation Costs in 2020, tech. rep., IRENA: International Renewable Energy Agency, **2021**.
[113] R. D. Clayton, M. P. Harold, V. Balakotaiah, C. Wan, *Appl. Catal. B* **2009**, *90*, 662–676.
[114] Renewable ammonia projects in Sub-Saharan Africa, tech. rep., Ammonia Energy Association, **2021**.
[115] B. Koranyi, Norway's Yara to spend $220 million to rebuild, expand Swedish plant, **2014**.
[116] P. Luck, Casale: The art of building a nitric acid plant, **2021**.
[117] A. H. Reksten, M. S. Thomassen, S. Møller-Holst, K. Sundseth, *International Journal of Hydrogen Energy* **2022**, *47*, 38106–38113.
[118] J. Osorio-Tejada, K. van't Veer, N. V. D. Long, N. N. Tran, L. Fulcheri, B. S. Patil, A. Bogaerts, V. Hessel, *Energy Conversion and Management* **2022**, *269*, 116095.
[119] EUROSTAT, Farms and farmland in the European Union - statistics, **2022**.
[120] P. Lettenmeier, Ammonia Technology Roadmap, tech. rep., Siemens, **2021**.

[121] G. J. van Rooij, H. N. Akse, W. A. Bongers, M. C. M. van de Sanden, *Plasma Physics and Controlled Fusion* **2017**, *60*, 014019.

[122] H. Noordende, P. Ripson, Gigawatt green hydrogen plant, State-of-the-art design and total installed capital costs, tech. rep., Intitute for Sustainable Process Technology, **2020**.

[123] Upply, The European road freight rate development benchmark Q2, **2020**.

[124] K. H. R. Rouwenhorst, F. Jardali, A. Bogaerts, L. Lefferts, *Energy Environ. Sci.* **2023**, *16*, 6170–6173.

[125] D. B. Graves, L. B. Bakken, M. B. Jensen, R. Ingels, *Plasma Chem. Plasma Process.* **2019**, *39*, 1–19.

[126] R. Ingels, Nitrogen enrichment of organic fertilizers with nitrate and air plasma, Canadian Patent 3116999, **2020**.

[127] Coilcraft, Determining Inductor Power Losses, tech. rep., Coilcraft, **2018**.

[128] Kyotoku, Power Losses of An Inductor, tech. rep., Kyotoku.

[129] S. Timmerberg, M. Kaltschmitt, M. Finkbeiner, *Energy Convers. and Manag.: X* **2020**, *7*, 100043.